

NOTE TO USERS

This reproduction is the best copy available.

UMI[®]



SCALE FORMATION AND DESCALING IN HOT ROLLING OF LOW CARBON STEEL

by

Vladimir Vinicio Basabe Mancheno

Department of Mining and Materials Engineering,
McGill University, Montreal, Canada

July 2008

McGill University

A thesis submitted to the Faculty of Graduate and Postdoctoral Studies in
partial fulfillment of the requirements for the degree of
Doctor of Philosophy

© **Vladimir Vinicio Basabe Mancheno, 2008**



Library and Archives
Canada

Published Heritage
Branch

395 Wellington Street
Ottawa ON K1A 0N4
Canada

Bibliothèque et
Archives Canada

Direction du
Patrimoine de l'édition

395, rue Wellington
Ottawa ON K1A 0N4
Canada

Your file *Votre référence*
ISBN: 978-0-494-66289-2
Our file *Notre référence*
ISBN: 978-0-494-66289-2

NOTICE:

The author has granted a non-exclusive license allowing Library and Archives Canada to reproduce, publish, archive, preserve, conserve, communicate to the public by telecommunication or on the Internet, loan, distribute and sell theses worldwide, for commercial or non-commercial purposes, in microform, paper, electronic and/or any other formats.

The author retains copyright ownership and moral rights in this thesis. Neither the thesis nor substantial extracts from it may be printed or otherwise reproduced without the author's permission.

In compliance with the Canadian Privacy Act some supporting forms may have been removed from this thesis.

While these forms may be included in the document page count, their removal does not represent any loss of content from the thesis.

AVIS:

L'auteur a accordé une licence non exclusive permettant à la Bibliothèque et Archives Canada de reproduire, publier, archiver, sauvegarder, conserver, transmettre au public par télécommunication ou par l'Internet, prêter, distribuer et vendre des thèses partout dans le monde, à des fins commerciales ou autres, sur support microforme, papier, électronique et/ou autres formats.

L'auteur conserve la propriété du droit d'auteur et des droits moraux qui protègent cette thèse. Ni la thèse ni des extraits substantiels de celle-ci ne doivent être imprimés ou autrement reproduits sans son autorisation.

Conformément à la loi canadienne sur la protection de la vie privée, quelques formulaires secondaires ont été enlevés de cette thèse.

Bien que ces formulaires aient inclus dans la pagination, il n'y aura aucun contenu manquant.


Canada

To my Mother, Father and Sisters who always love and support me

Abstract

In this research, the effects of gas composition, elapsed time of reaction and temperature on scale formation and descaling of low carbon steel were investigated and results were discussed from the viewpoint of the phase composition of the scales, oxidation rates, oxidation mechanisms, adhesion, fracture mechanics, porosity and residual scale.

The phase composition and morphology of scales grown under conditions similar to those of reheating furnaces were analyzed. Low carbon steel was oxidized over the temperature range 1000-1250°C in gas mixtures of O₂-CO₂-H₂O-N₂, O₂-H₂O-N₂ and O₂-CO₂-N₂. The mole fraction of each phase, wüstite (FeO), magnetite (Fe₃O₄) and hematite (Fe₂O₃) was determined by the direct comparison method. Two types of scales were observed. The first type was a crystalline scale with an irregular outer surface composed mostly of wüstite, and a negligible amount of magnetite. The second type was the classical three-layer scale composed of wüstite, magnetite and hematite. In general, the experiments showed that the furnace atmosphere, oxidation time and temperature influence the phase composition of the scales.

Low carbon steel was oxidized in air over the temperature range 600-1200°C for 120 s to approximate the formation of secondary and tertiary scale in hot rolling. The mole fraction of wüstite, magnetite and hematite was determined by the direct comparison method. The phase composition of the scales changed with temperature and time. During the initial 30 s of oxidation, wüstite was the predominant phase in the temperature range 800-1200°C, and as oxidation proceeded, the percentages of magnetite and hematite increased. In addition, the texture of the scales was investigated by orientation imaging microscopy (OIM); it was found that temperature influences the texture of the scales. The experiments indicated that 850°C is the ideal temperature for the finishing mill in order to reduce surface defects and work roll wear.

The adhesion of scales formed in air on low carbon steel in continuous heating and isothermal conditions was investigated with a four-point bending test. The separation (crack) always occurred inside the scale indicating that the strength of the scale is lower than the strength of the scale/steel interface. It was found that scale adhesion is related to scale porosity, blister formation and stresses acting in the scale. A spallation process was observed when cooling from 800°C to room temperature. The microscopic observations revealed that spallation followed route 1 “strong interface and weak oxide.”

Low carbon steel was oxidized over the temperature range 1050-1250°C in O₂-CO₂-H₂O-N₂ gas mixtures in order to study the hydraulic descaling process. The oxidation times were 15-120 min. and the scales were 130-2000 μm thick. The experimental parameters were chosen to approximate scale formation under conditions similar to those of reheating furnaces. In the hydraulic descaling tests, two modes of scale removal were observed. In the first mode, observed in classical three-layer scales that developed an inner porous layer with low or medium porosity, the horizontal undercutting occurred at the boundary of the inner porous layer and dense scale. The second mode was observed in classical three-layer scales that developed an inner porous layer with high porosity and in crystalline scales. In the second mode, the horizontal undercutting occurred at the first plane of large pores relative to the scale/steel interface. In general, the experiments showed that scale morphology controlled the removability of scale.

Résumé

Dans cette recherche, les effets de la composition des gaz, le temps de réaction et la température sur la formation de la calamine et du décalaminage ont été étudiés sur l'acier à faible teneur en carbone et les résultats ont été discutés par rapport aux points de vue des compositions de phase des calamines, des vitesses d'oxydation, des mécanismes d'oxydation, de l'adhésion, des mécanismes de fracture, de la porosité et de la calamine résiduelle.

La composition de la phase et la morphologie des calamines développées sous des conditions similaires à celles des fours à réchauffer ont été analysées. L'acier à faible teneur en carbone a été oxydé entre les températures 1000-1250°C dans les mélanges gazeux d' O_2 - CO_2 - H_2O - N_2 , O_2 - H_2O - N_2 et O_2 - CO_2 - N_2 . La fraction molaire de chaque phase, wüstite (FeO), magnetite (Fe_3O_4) et hematite (Fe_2O_3) a été déterminée par la méthode de comparaison directe. Deux types de calamines ont été observés. Le premier type est la calamine cristalline avec une surface extérieure irrégulière composée essentiellement de wüstite, et une portion négligeable de magnetite. Le second type est la classique calamine de trois couches composé de wüstite, magnetite et hematite. En général, les expériences ont démontré que l'atmosphère du fourneau, le temps d'oxydation et la température influencent la composition de phase des calamines.

L'acier à faible teneur en carbone a été oxydé à l'air entre les températures de 600-1200°C pour 120 s pour simuler la formation de la seconde et troisième calamine dans le laminage à chaud. La fraction molaire de wüstite, magnetite et hematite a été déterminée par la méthode de comparaison directe. La phase de composition des calamines a changé avec la température et le temps. Durant les 30 secondes initiales d'oxydation, wüstite a été la phase prédominante entre les températures 800-1200°C, et alors que l'oxydation se poursuivait, les pourcentages de magnetite et d'hématite ont augmenté. De plus, la texture des calamines a été investiguée par orientation imaging microscopy (OIM); il a été observé que la température influence la texture des

calamines. Les expériences ont indiqué que 850°C était la température idéale pour le train finisseur afin de réduire les défauts de surface et l'usure du cylindre travail.

L'adhésion des calamines qui se forment à l'air sur de l'acier à faible teneur en carbone dans un chauffage continu et dans des conditions isothermiques a été investiguée par l'essai de pliage à quatre points. La séparation (fissure) a toujours eu lieu à l'intérieur de la calamine indiquant que la résistance de la calamine était moindre que la résistance de l'interface acier/calamine. Il a été prouvé que l'adhésion de la calamine était reliée à la porosité de la calamine, à la formation de cloques et aux multiples stress agissants sur la calamine. Le processus de spallation a été observé en rafraîchissant la température de 800°C à la température de la pièce. Les observations microscopiques ont révélé que la spallation a suivi la route 1 "forte interface et faible oxyde."

L'acier à faible teneur en carbone a été oxydé entre les températures 1050-1250°C dans les mélanges gazeux d' O_2 - CO_2 - H_2O - N_2 pour étudier le procès de décalaminage hydraulique. Les temps d'oxydation ont été de 15 à 120 min. et les calamines étaient 130-2000 μm d'épaisseur. Les paramètres expérimentaux ont été choisis pour simuler la formation de la calamine sous des conditions similaires à celles des fours à réchauffer. Dans les tests de décalaminage hydraulique, deux modes d'enlèvement de la calamine ont été observés. Dans le premier mode, observé dans les classiques calamines à trois couches qui ont développé une couche intérieure poreuse avec une faible ou moyenne porosité, la sous coupe horizontale a eu lieu à la frontière de la couche intérieure poreuse et de la couche dense de la calamine. Le second mode a été observé dans les classiques calamines à trois couches qui ont développé une couche intérieure poreuse avec une grande porosité et dans les calamines cristallines. Dans le second mode, la sous coupe horizontale a eu lieu au premier plan de larges pores en rapport avec l'interface acier/calamine. En général, les expériences ont démontré que la morphologie de la calamine contrôlait l'enlèvement de la calamine.

Acknowledgements

I would like to thank my supervisor Professor Jerzy A. Szpunar, for his support and guidance. I would like also to thank Slavek Poplawski for his help with the X-ray measurements and for his technical support. I express my deepest thanks to McGill University, which gave me the opportunity to realize this work and the privilege of being surrounded by a highly motivated research environment.

I wish to express my gratitude to Hualong Li, Jong-Tae Park, Jae-Young Cho, Jianlong Lin, Yang Cao, Shixue Wen, Raed Hazhaikch and Kabir Mirpuri, who shared ideas and friendship during my Ph.D. studies at McGill University. In particular, thanks go to Alexander Blander for his training, and help in the use of the scanning electron microscope (SEM) and orientation imaging microscopy (OIM). My special gratitude goes to Sara Israel for her great contribution in preparing the edition of this work, and her constant encouragement and support.

Finally, I am deeply indebted to my parents, who always provide stability, guidance and inspiration.

CONTENTS

Chapter I – Introduction.....	1
Scope of Present Work.....	2
Chapter II - Literature Review.....	4
2.1 Iron Oxides.....	5
2.2 Thermodynamic Aspects of Iron Oxides.....	6
2.3 Oxidation Mechanism of Iron.....	10
2.4 Iron Oxide Scales on Steels.....	11
2.5 Classification of Scales.....	13
2.6 Oxidation Rates.....	13
2.6.1 Effect of Steel Composition on Oxidation Rate.....	17
2.6.2 Effect of Atmosphere on Oxidation Rate.....	18
2.6.3 Effect of Gas Velocity on Oxidation Rate.....	24
2.7 Effect of Scaling on Hot Rolling.....	24
2.8 Hydraulic Descaling in Hot Rolling.....	26
2.9 Mechanical Stresses in Oxide Scales.....	28
2.12.1 Stresses Arising from Oxide Growth.....	28
2.12.2 Stresses Arising from Temperature Changes.....	29
Chapter III - Phase Composition of Oxide Scales during Reheating.....	32
3.1 Introduction.....	33
3.2 Objectives.....	34
3.3 Experimental.....	35
3.3.1 Sample Preparation.....	35

3.3.2	Quantitative Phase Analysis by X-ray Diffraction.....	38
3.4	Results and Discussion.....	44
3.5	Summary.....	56
 Chapter IV - Secondary and Tertiary Scales in Hot Rolling.....		57
4.1	Introduction.....	58
4.2	Objectives.....	58
4.3	Experimental.....	59
4.3.1	Rate of Scale Growth and Scale Thickness Measurements.....	59
4.3.2	Phase Composition.....	60
4.3.3	Texture and Microstructure Analyses	60
4.3.4	Pore Formation.....	63
4.4	Results and Discussion.....	68
4.4.1	Scale Morphology.....	68
4.4.2	Pore Formation.....	69
4.4.3	Rate of Scale Growth.....	69
4.4.4	Phase Composition.....	74
4.4.5	Microstructure and Microtexture Analysis.....	77
4.5	Summary.....	79
 Chapter V - Adhesion of Oxide Scales.....		81
5.1	Introduction.....	82
5.2	Objectives.....	83
5.3	Experimental.....	83
5.3.1	Four-Point Bending Test.....	83
5.3.2	Sample Preparation.....	84
5.4	Results and Discussion.....	92
5.4.1	Continuous Heating Experiments.....	92

5.4.2 Isothermal Experiments.....	105
5.5 Summary.....	110
Chapter VI - Effect of O₂ in Heating Atmosphere on Hydraulic Descaling.....	111
6.1 Introduction.....	112
6.2 Objectives.....	112
6.3 Experimental.....	113
6.4 Results and Discussion.....	116
6.4.1 Scale Morphology.....	116
6.4.1.1 Formation of Pores due to Idiomorphic Growth....	117
6.4.1.2 Formation of Pores due to Growth Stress.....	117
6.4.2 Modes of Scale Removal.....	122
6.4.2.1 Mode I.....	122
6.4.2.2 Mode II.....	123
6.4.3 Removability of Scale.....	130
6.5 Summary.....	136
Chapter VII - Conclusions, Contribution to Knowledge and Suggested Future Work.....	137
7.1 Conclusions.....	138
7.2 Contribution to Knowledge.....	140
7.3 Suggested Future Work.....	141
7.3.1 The Effect of H ₂ O on Hydraulic Descaling.....	141
7.3.2 The Effect of Nickel in Steel on Hydraulic Descaling.....	141
References.....	143

Contents

Appendix A.....	154
Appendix B.....	157

Figures

Chapter 2

- Figure 2.1** Phase stability in the system Fe-Fe₂O₃ as a function of ΔG° and temperature (Gaskell, 1995).
- Figure 2.2** The iron-oxygen phase diagram (Darken and Gurry, 1945, 1946; Gaskell, 1995).
- Figure 2.3** Oxidation mechanism of iron to form a three-layered scale of FeO, Fe₃O₄ and Fe₂O₃ above 570°C showing diffusion steps and interfacial reactions (Birks and Meier, 1983).
- Figure 2.4** Relationship between temperature and metal loss (Cook and Rasmussen, 1970).
- Figure 2.5** Equilibrium products of combustion of natural gas related to percentage of theoretical combustion air (Cook and Rasmussen, 1970).
- Figure 2.6** As percentage of combustion air decreases, percentage of oxidants decreases, while that of reducers increase (Cook and Rasmussen, 1970).
- Figure 2.7** Scale-free heating strategy proposed by Cook and Rasmussen (1970).
- Figure 2.8** Influence of additions of carbon monoxide and oxygen to the neutral atmosphere, free form and also containing 0.17% of sulphur dioxide, on the scaling of plain carbon steel (Preece *et al.*, 1939).
- Figure 2.9** Mechanism of scale defects (Seki *et al.*, 1996).

Figure 2.10 Bochum hot strip mill; layout of the descaling equipment (Becker *et al.*, 2000).

Chapter 3

Figure 3.1 Schematic diagram of: a) Bragg-Brentano geometry, b) diffractometer.

Figure 3.2 Oxide powder diffraction patterns illustrating the influence of: free oxygen a), c); carbon dioxide c), e); oxidation time a), b); water vapour b), d); temperature a), f). The scales were formed in: a) 1O₂-15CO₂-10H₂O-N₂ for 12 min. at 1250°C, b) 1O₂-15CO₂-10H₂O-N₂ for 120 min. at 1250°C, c) 5O₂-15CO₂-10H₂O-N₂ for 12 min. at 1250°C, d) 1O₂-15CO₂-N₂ for 120 min. at 1250°C, e) 5O₂-10H₂O-N₂ for 12 min. at 1250°C, f) 1O₂-15CO₂-10H₂O-N₂ for 12 min. at 1050°C.

Figure 3.3 Scales formed at 1250°C for 60 min. in: a) 1O₂-15CO₂-10H₂O-N₂, crystalline scale with an irregular outer surface; b) 5O₂-15CO₂-10H₂O-N₂, classical three-layer scale. During cooling with a flow of argon, some wüstite decomposed resulting in the precipitation of magnetite in the wüstite layer.

Figure 3.4 Effect of free oxygen, oxidation time and temperature on the percentages of FeO, Fe₃O₄ and Fe₂O₃ in the scales formed on low carbon steel. Samples a), b), c), d) oxidized in 1O₂-15CO₂-10H₂O-N₂ for: a) 12 min., b) 30 min., c) 60 min., d) 120 min.; samples e), f), g), h) oxidized in 5O₂-15CO₂-10H₂O-N₂ for: e) 12 min., f) 30 min., g) 60 min., h) 120 min.

Figure 3.5 Effect of free oxygen, carbon dioxide, water vapour and oxidation time on the percentages of FeO, Fe₃O₄ and Fe₂O₃ in the scales formed on low carbon steel oxidized at 1100°C in: a) 1O₂-15CO₂-10H₂O-N₂, b) 5O₂-15CO₂-10H₂O-N₂, c) 1O₂-10H₂O-N₂, d) 5O₂-10H₂O-N₂, e) 1O₂-15CO₂-N₂, f) 5O₂-15CO₂-N₂.

Figure 3.6 Scale formed in 1O₂-15CO₂-N₂ at 1100°C for 60 min.

Figure 3.7 Effect of free oxygen, carbon dioxide, water vapour and oxidation time on the percentages of FeO, Fe₃O₄ and Fe₂O₃ in the scales formed on low carbon steel oxidized at 1250°C in: a) 1O₂-15CO₂-10H₂O-N₂, b) 5O₂-15CO₂-10H₂O-N₂, c) 1O₂-10H₂O-N₂, d) 5O₂-10H₂O-N₂, e) 1O₂-15CO₂-N₂, f) 5O₂-15CO₂-N₂.

Figure 3.8 Scale formed in 1O₂-15CO₂-N₂ at 1250°C for 120 min.

Chapter 4

Figure 4.1 (200) pole figure of the low carbon steel used for the oxidation tests.

Figure 4.2 Schematic diagram of the thermogravimetric analyzer.

Figure 4.3 Diagram of the components of the EBSD system.

Figure 4.4 Diagram illustrating the origin of Kikuchi lines in EBSD.

Figure 4.5 Schematic representation of scale defects in isothermal oxidation above 850°C.

Figure 4.6 Scales formed in air for 120 s at the temperature of: a) 800°C, b) 850°C, c) 900°C.

Figure 4.7 The image quality (IQ) of scales formed at 950°C in air for: a) 5 s, b) 10 s, c) 120 s.

Figure 4.8 Thickness of scales formed on low carbon steel in air over the temperature range 600-1200°C for 120 s. The dashed line for the temperature of 850°C indicates the division between homogeneous oxide and non-homogeneous oxide.

Figure 4.9 Scale formed in air for 40 s at 1200°C showing high porosity.

Figure 4.10 Oxide powder diffraction patterns after isothermal oxidation in air at 1050°C for: a) 30 s, b) 120 s, c) 600 s.

Figure 4.11 Iron oxide composition as a function of temperature and oxidation time for: a) 30 s, b) 120 s, c) 600 s.

Figure 4.12 The image quality (IQ) of scales formed in air for 10 s at the temperature of: a) 850°C, b) 900°C, c) 950°C.

Figure 4.13 The EBSD phase map of a scale grown for 10 s at 950°C. The blue region: bcc iron; the red: wüstite; the yellow: magnetite.

Figure 4.14 (001) pole figures of the wüstite and magnetite phases for the temperatures of: a) 850°C, b) 900°C, c) 950°C.

Chapter 5

Figure 5.1 Schematic representation of the four-point bending arrangement.

Figure 5.2 Mounting jig used to align the oxidized steel sample and stainless steel loading bars.

- Figure 5.3** Schematic representation of the four-point bending jig.
- Figure 5.4** Four-point bending test.
- Figure 5.5** Schematic representation of the sample holder used to mount the steel samples for oxidation experiments.
- Figure 5.6** Continuous heating schedule adopted for oxidizing the steel samples.
- Figure 5.7** Isothermal experiments at 700, 800 and 950°C.
- Figure 5.8** Schematic of cracking and spallation caused by compressive oxide stress (Evans and Lobb, 1984; Evans, 1988).
- Figure 5.9** Spallation of scale during cooling from 800°C. The decohesion plane (crack) was localized in the scale. The shear crack through the scale thickness reveals that spallation occurred according to route 1 (strong interface and weak oxide). The scale was formed in air during continuous heating to 800°C.
- Figure 5.10** Linear load-displacement behavior in the four-point bending test. The scale was formed in air during continuous heating to 880°C.
- Figure 5.11** The three modes of loading in a crack.

- Figure 5.12** The image quality (IQ) of a scale after debonding in the four-point bending test. Some scale remained on the steel after debonding. The crack detached the scale close to the scale/steel interface. After detaching the scale, the crack propagated into the remaining scale showing the exact position of the plane of decohesion (crack), which is located in the wüstite grains (cleavage fracture). The scale was formed in air during continuous heating to 950°C.
- Figure 5.13** Scales formed in air during continuous heating to: a) 880°C, b) 1200°C. The increase in time and temperature in the continuous heating schedule resulted in an increase in the size and concentration of pores.
- Figure 5.14** Fracture map for oxides (Gandhi and Ashby, 1979). The interval in which the fractures occurred in the present study is indicated.
- Figure 5.15** Critical load required to de-adhere scales in the four-point bending test at room temperature. The scales were grown in air under a continuous heating to 800, 880, 950 and 1200°C. A zero value was assigned to the scales that spalled when cooling from the temperature of 800°C. The mean scale thickness, X , is indicated beside each data point.
- Figure 5.16** Scale formed in air at the temperature of 700°C for 4320 min. showing large pores near the scale/steel interface.

- Figure 5.17** Critical load required to deadhere scales of 130 μm in thickness in the four-point bending test at room temperature. The scales were grown in air at the temperatures of 700, 800 and 950°C for 4320, 150 and 10 min. respectively. A zero value was assigned to the scales that spalled when cooling from the temperature of 800°C, and to the detached scales by blistering at 950°C.
- Figure 5.18** Spallation of scale during cooling from 800°C in the isothermal experiments. The decohesion plane was localized in the scale. The spallation occurred close to the outer surface of the scale according to route 1 (strong interface and weak oxide). The scale was formed in air at the temperature of 800°C for 150 min.
- Figure 5.19** Side view photo of a blistered scale formed in air at the temperature of 950°C for 10 min. The adhesion of the blistered scale was low. As a result, during sample handling some blistered scale detached leaving a thin layer of residual scale on the steel substrate.

Chapter 6

- Figure 6.1** Schematic diagram of the hydraulic descaling test.
- Figure 6.2** Schematic diagram of the scale measurements.
- Figure 6.3** Cross-sections of scales formed at 1250°C in: a) 1O₂-15CO₂-10H₂O-N₂ for 30 min., crystalline scale showing inner porous layer formation, b) 5O₂-15CO₂-10H₂O-N₂ for 120 min., classical three-layer scale showing inner porous layer formation. During cooling some wüstite decomposed, resulting in the precipitation of magnetite in the wüstite layer.

Figure 6.4 Vacancy fluxes, J_v , in single grains due to imposed stresses: a) through vacancy-lattice diffusion (Nabarro-Herring creep); b) through diffusion along grain boundaries (Coble creep). Interstitial defects move in the opposite direction as the vacancies (Kofstad, 1985).

Figure 6.5 a) Four grains in a hexagonal array; the diffusion centers are marked with circles. XYZ is a marker line parallel to the tensile axis. b) The same grains after diffusion creep in the absence of any relative grain movement; the new diffusion centers are marked with crosses. XYZ is in the same relative position. c) The same grains after diffusion creep in the presence of relative grain movement. The marked line is now divided into segments, XY' and Y''Z (After Evans and Langdon, 1976).

Figure 6.6 Cross-section of scale formed at 1250°C in 5O₂-15CO₂-10H₂O-N₂ for 60 min. showing pore formation (arrowed) at the grain boundaries.

Figure 6.7 Top view of specimen after hydraulic descaling test. The crystalline scale was formed in 1O₂-15CO₂-10H₂O-N₂ for 60 min. at 1250°C.

Figure 6.8 Schematic diagram of: a) three-layer scale before hydraulic descaling in mode I, b) residual scale after hydraulic descaling in mode I.

Figure 6.9 Effect of free oxygen, oxidation time and temperature on: a) scale thickness, b) inner porous layer thickness.

Figure 6.10 Cross-section of three-layer scale after hydraulic descaling in mode I. The three-layer scale was formed in 5O₂-15CO₂-10H₂O-N₂ for 30 min. at 1150°C.

Figure 6.11 Schematic diagram of: a) three-layer scale before hydraulic descaling in mode II, b) crystalline scale before hydraulic descaling in mode II, c) residual scale after hydraulic descaling in mode II.

Figure 6.12 Cross-section of three-layer scale after hydraulic descaling in mode II. The three-layer scale was formed in $5\text{O}_2\text{-}15\text{CO}_2\text{-}10\text{H}_2\text{O-N}_2$ for 60 min. at 1250°C . Outside of the jet impact zone some dense scale was removed together with the scale of the jet impact zone.

Figure 6.13 Mean thickness of the residual scale, standard deviation and mode of scale removal as a function of temperature, free oxygen and oxidation time. The low carbon steel was oxidized for 15, 30, 60, 120 min. in $1\text{O}_2\text{-}15\text{CO}_2\text{-}10\text{H}_2\text{O-N}_2$ at: a) 1050°C , c) 1100°C , e) 1150°C , g) 1200°C , i) 1250°C , and in $5\text{O}_2\text{-}15\text{CO}_2\text{-}10\text{H}_2\text{O-N}_2$ at: b) 1050°C , d) 1100°C , f) 1150°C , h) 1200°C , j) 1250°C .

Figure 6.14 Figure 6.14 Cross-sections of scales and their residual scales after hydraulic descaling in mode II. The pores (arrowed) of the first plane of large pores relative to the scale/steel interface are indicated in the middle column. The scales were formed in: a) $1\text{O}_2\text{-}15\text{CO}_2\text{-}10\text{H}_2\text{O-N}_2$ for 60 min. at 1050°C , three-layer scale, b) $1\text{O}_2\text{-}15\text{CO}_2\text{-}10\text{H}_2\text{O-N}_2$ for 120 min. at 1050°C , three-layer scale, c) $1\text{O}_2\text{-}15\text{CO}_2\text{-}10\text{H}_2\text{O-N}_2$ for 30 min. at 1150°C , crystalline scale, d) $1\text{O}_2\text{-}15\text{CO}_2\text{-}10\text{H}_2\text{O-N}_2$ for 120 min. at 1150°C , three-layer scale, e) $1\text{O}_2\text{-}15\text{CO}_2\text{-}10\text{H}_2\text{O-N}_2$ for 60 min. at 1250°C , crystalline scale, f) $5\text{O}_2\text{-}15\text{CO}_2\text{-}10\text{H}_2\text{O-N}_2$ for 30 min. at 1250°C , three-layer scale.

Tables

Chapter 2

- Table 2.1** Crystal structure of iron oxides.
- Table 2.2** PBR values for iron oxides.
- Table 2.3** Thermal expansion coefficients of some metal substrates.
- Table 2.4** Thermal expansion coefficients of FeO and Fe₂O₃.
- Table 2.5** Thermal expansion coefficients of Fe₃O₄.

Chapter 3

- Table 3.1** Chemical composition of the steel (wt %).
- Table 3.2** Temperatures (°C) and gas mixtures (v%) used to oxidize the low carbon steel.
- Table 3.3** R factor intensity analysis.

Chapter 5

- Table 5.1** Chemical composition of the steel (wt %).
- Table 5.2** Fracture mechanism analysis in the four-point bending test.

Chapter 6

Table 6.1 Chemical composition of the steel (wt %).

Table 6.2 Mode of scale removal and scale morphology for different temperatures, gas mixtures and oxidation times.

Appendix

Table A.1 Example of scale analysis. The scale was formed in 5O₂-15CO₂-N₂ gas mixture at 1100°C for 60 min.

Table A.2 Analysis of the iron oxides in scales formed over the temperature range 1000-1250°C in 1O₂-15CO₂-10H₂O-N₂ gas mixture.

Table A.3 Analysis of the iron oxides in scales formed over the temperature range 1000-1250°C in 5O₂-15CO₂-10H₂O-N₂ gas mixture.

Table A.4 Analysis of the iron oxides in scales formed at the temperature of 1100°C and 1250°C in 1O₂-15CO₂-N₂ gas mixture.

Table A.5 Analysis of the iron oxides in scales formed at the temperature of 1100°C and 1250°C in 1O₂-10H₂O-N₂ gas mixture.

Table A.6 Analysis of the iron oxides in scales formed at the temperature of 1100°C and 1250°C in 5O₂-15CO₂-N₂ gas mixture.

Table A.7 Analysis of the iron oxides in scales formed at the temperature of 1100°C and 1250°C in 5O₂-10H₂O-N₂ gas mixture.

Table A.8 Analysis of the iron oxides in scales formed over the temperature range 750-1200°C in dry air.

Chapter One

Introduction

In hot strip mills, the heating of slabs before hot deformation is necessary to soften the steel before rolling. In the reheating of the slab, a primary scale of around 2 mm in thickness is formed when the slab is reheated to 1250-1260°C. After the first descaling, thin secondary and tertiary scales grow fast in the subsequent stages of the hot rolling process.

During hot rolling, scales can cause surface defects. To prevent these defects, scales are removed by mechanical and/or hydraulic descaling. Although descaling is a common and a reliable practice, the loss of material due to scale is still present in the hot rolling of steel strip. Therefore, studies on scale formation and descaling of steels oxidized in conditions similar to those of hot strip mills are of great interest to better understand the descaling process.

In the analysis of the descaling process, it is necessary not only to analyze descaling as the removal of the scales but also as a process that is related to the control of the scales in the reheating of the slab and along the different stages of the hot rolling process. In the present work, the approach to scale formation and descaling is dynamic, in that several factors and their relationships are analyzed with the purpose of defining better descaling conditions and rolling practices.

Scope of Present Work

The present work has been organized into seven chapters. Chapter 1 presents an introduction. Chapter 2 provides a literature review of the fundamental aspects of oxidation of iron and steels, scale formation, descaling and hot rolling. In Chapter 3, the influence of the furnace atmosphere, oxidation time and temperature on the phase composition of scales grown on low carbon steel under conditions similar to those of reheating furnaces is analyzed, and results are discussed quantitatively from the view point of the scale morphology. Chapter 4 deals with the growth rate and phase composition of secondary and tertiary scales in hot rolling of low carbon steel. Chapter 5 deals with the adhesion of scales grown on low carbon steel under continuous heating

and isothermal conditions. The influence of scale morphology on scale adhesion is analyzed and discussed. Chapter 6 analyses the effect of the concentration of O₂ in the heating atmosphere on hydraulic descaling of low carbon steel. In this chapter the influence of scale morphology on the removability of scale is analyzed and discussed. Chapter 7 contains the conclusions of the present work, its contribution to the original knowledge and suggested future work.

**Chapter
Two**

Literature Review

2.1 Iron Oxides

Iron is thermodynamically unstable when exposed to the atmosphere, and above 570°C, three iron oxides can be formed: wüstite, FeO; magnetite, Fe₃O₄; and hematite, Fe₂O₃; (Caplan and Cohen, 1966; Sachs and Tuck, 1968; Kofstad, 1988). The crystal system of wüstite is cubic with a halite structure (NaCl) (see Table 2.1). In the halite structure of wüstite, the anions are cubic close-packed with a sequence ABAB along the [111] direction, and the cations are situated in the octahedral interstices. Wüstite is metal deficient, Fe_{1-y}O. The metal deficit y in wüstite as a function of the partial pressure of oxygen has been studied over the temperature range of 800-1250°C; it has been found that depending on the temperature, the metal deficit y in wüstite can vary from 0.05 at the iron/wüstite interface to about 0.15 at the wüstite/magnetite interface (Vallet and Raccach, 1965; Vallet, 1965; Kofstad 1988). These high cation vacancies result in a high mobility of cations and electrons via metal vacancies and electron holes (Khanna, 2002).

The wüstite phase decomposes to magnetite and alpha-iron when cooling to temperatures below 570°C (Kubaschewski and Hopkins, 1962; Modin, 1962; Shiraiwa and Matsuno, 1967). The decomposition of wüstite depends on the cooling temperature; the fastest decomposition of wüstite is observed at 400°C (Shiraiwa and Matsuno, 1967). The cooling rate also influences the decomposition of wüstite. A high cooling rate partially or completely prevent the decomposition of wüstite (Modin, 1962; Sheasby *et al.*, 1984).

The crystal system of magnetite is cubic with (MgAl₂O₄) structure, Table 2.1. The unit cell of the (MgAl₂O₄) structure contains 32 oxygen ions, 32 octahedral sites and 64 tetrahedral sites. Magnetite has 16 trivalent cations and 8 divalent cations. At and below room temperature, the trivalent cations occupy one eighth of the tetrahedral sites and one fourth of the octahedral sites; the divalent cations occupy one fourth of the octahedral sites. This particular distribution of cations is known as the inverse spinel structure, in which the oxygen ions are cubic closed-packed with a sequence ABCABC along the [111] direction, (Cornell and Schwertmann, 2003). At high temperatures,

magnetite has the normal spinel structure, in which the trivalent cations occupy one half of the octahedral sites and the divalent cations occupy one eighth of the tetrahedral sites. Magnetite has little deviation from stoichiometry, and the excess of oxygen is much smaller than with wüstite (Kubaschewski and Hopkins, 1962).

Hematite has two structures, α -Fe₂O₃ and γ -Fe₂O₃. At high temperatures, magnetite oxidizes to form α -Fe₂O₃, therefore, only the α -Fe₂O₃ structure is present at high temperature. The crystal system of hematite in the form α -Fe₂O₃ is rhombohedral with (α -Al₂O₃) structure, Table 2.1. In (α -Al₂O₃) structure (called corundum structure), the oxygen ions of hematite are hexagonal closed-packed with a sequence ABAB along the [001] direction, and the trivalent iron cations occupy two thirds of the octahedral sites (Cornell and Schwertmann, 2003).

Table 2.1 *Crystal structure of iron oxides.*

Oxide	System	Space group	Type of structure	Lattice parameters (Å) *	
				a	c
FeO	Cubic	Fm3m	NaCl	4.307	-
Fe ₃ O ₄	Cubic	Fd3m	MgAl ₂ O ₄	8.3967	-
Fe ₂ O ₃	Rhombohedral	$\bar{R}3c$	α -Al ₂ O ₃	5.034	13.752

* Taken from 6-0615, 11-614 and 13-534 JCPDS cards (1974).

2.2 Thermodynamic Aspects of Iron Oxides

The chemical reaction of the metal M with oxygen gas O_2 to form the oxide M_aO_b can be written as follows:



The above chemical reaction occurs only when the free energy change for the reaction is negative. This implies that thermodynamically, the oxide will form only if the ambient oxygen pressure is larger than the dissociation pressure of the oxide in equilibrium with the metal (Kofstad, 1988):

$$p_{O_2} \geq \exp\left\{-\frac{2\Delta G^\circ(M_aO_b)}{bRT}\right\} \quad (2.2)$$

where p_{O_2} is the partial pressure of oxygen, ΔG° the standard free energy change of the reaction, R the gas constant and T the absolute temperature.

The equilibrium partial pressure of oxygen (often called dissociation pressure) $p_{O_2,eq}$, below which no oxidation occurs, can be easily obtained in the Ellingham/Richardson diagram. In this diagram, the equilibrium partial pressure is obtained for a required temperature. The diagram represents the thermodynamic driving force for a reaction to occur; the most stable oxides have the largest negative value of ΔG° . The Ellingham/Richardson diagram of iron oxides is shown in Figure 2.1. In this diagram, it is possible to observe that the stability of the iron oxides increases from hematite to wüstite.

Phase diagrams are used to predict the probable reaction products and the sequence of oxides in a multilayer scale. The most oxygen-deficient oxide is next to the metal, and the most oxygen-rich next to the gas phase (Kofstad, 1988). The iron-oxygen phase diagram is given in Figure 2.2. The diagram shows that in the oxidation of iron in air or oxygen above 570°C, the scale consists of three layers arranged in order of oxygen content. The inner layer, with the lowest oxygen content is wüstite, the intermediate layer magnetite, and the outer layer hematite.

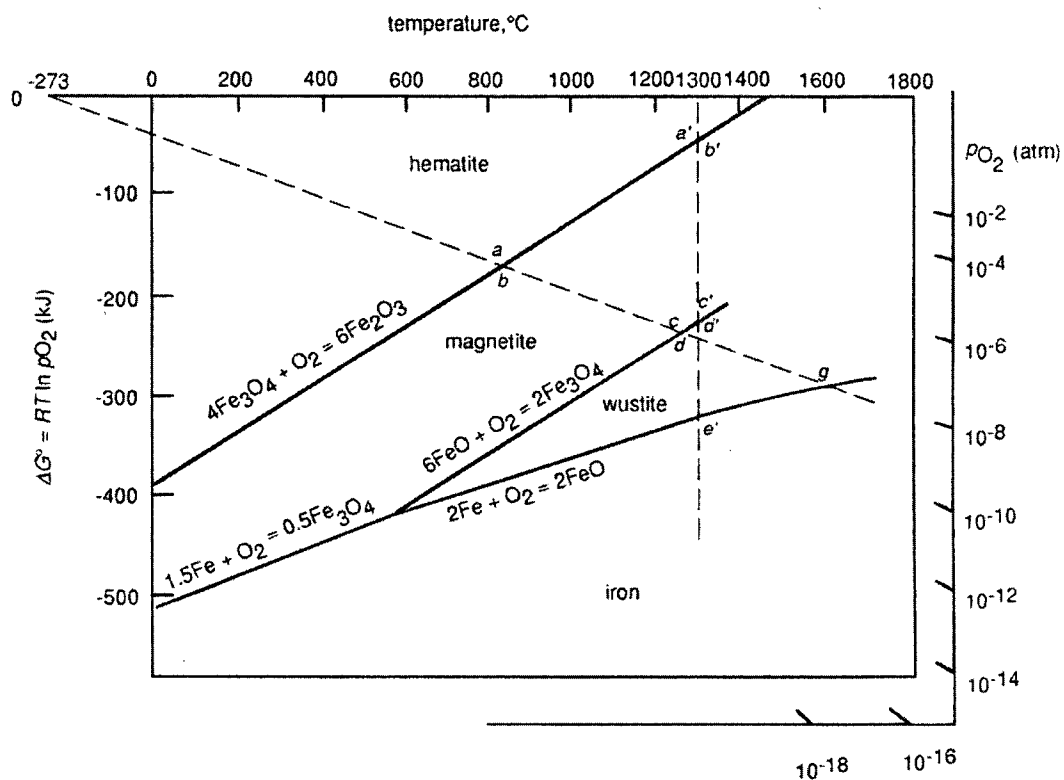


Figure 2.1 Phase stability in the system Fe-Fe₂O₃ as a function of ΔG° and temperature (Gaskell, 1995).

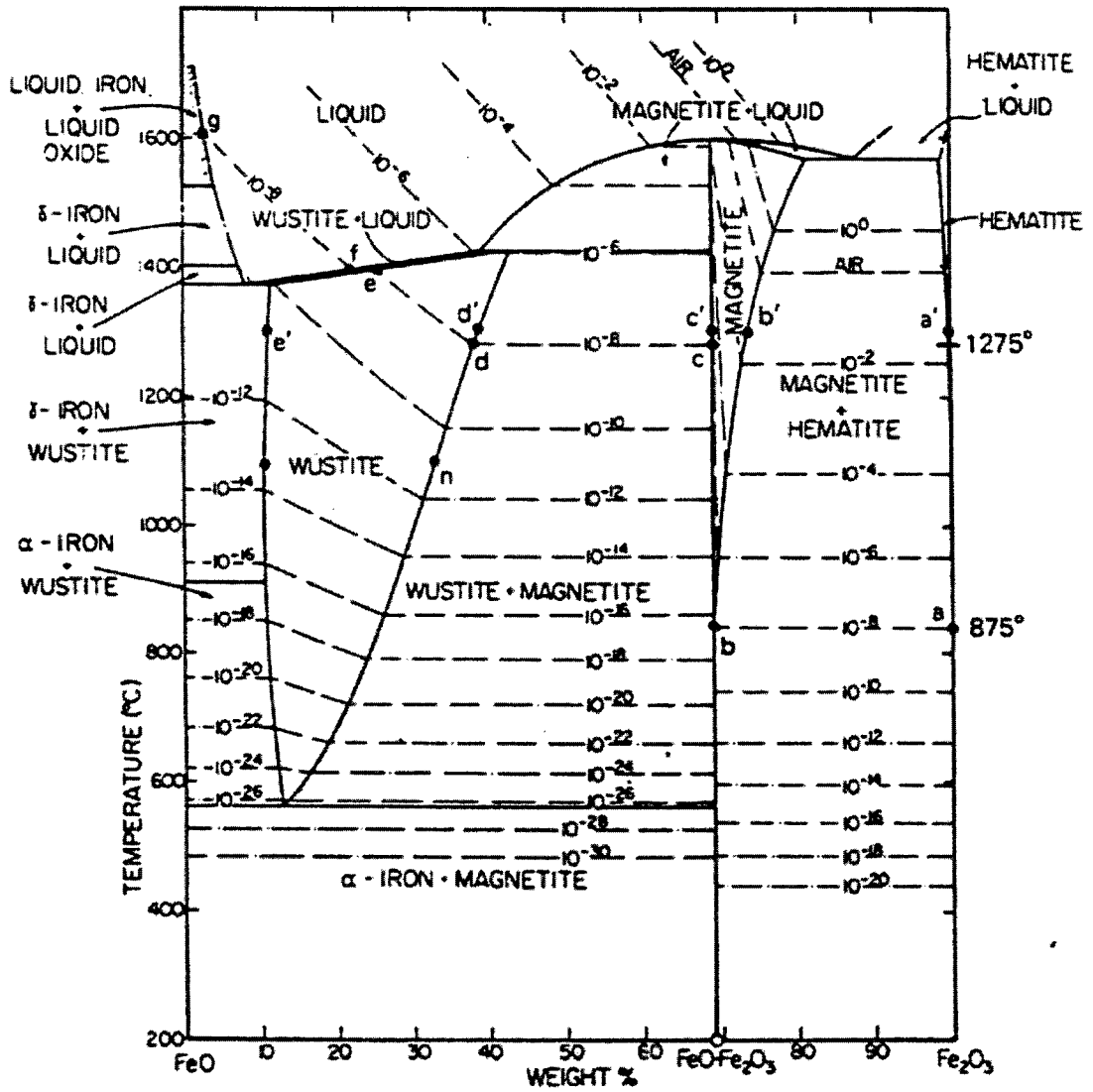


Figure 2.2 The iron-oxygen phase diagram (Darken and Gurry, 1945, 1946; Gaskell, 1995).

2.3 Oxidation Mechanism of Iron

Birks and Meier (1983) proposed a mechanism for scale growth in the oxidation of iron above 570°C (see Figure 2.3). In their model, the mechanism of iron oxidation in a multilayer scale is explained through the following reactions:

Iron ionises at the wüstite/iron interface according to the reaction:



Iron ions and electrons migrate in the wüstite layer via iron vacancies and electron holes respectively. At the magnetite/wüstite interface, iron ions and electrons react with magnetite forming wüstite according to the reaction:



In the magnetite layer, iron ions migrate via iron ion vacancies in the tetrahedral and octahedral sites, and electrons migrate via electron holes and excess electrons. At the hematite/magnetite interface magnetite is formed through the reactions:



Hematite can be formed by iron ions moving outward or oxygen ions moving inward in the hematite layer. In the outward migration of iron ions in the hematite layer, the iron ions migrate via iron ion vacancies together with electrons. The reaction for the formation of hematite at the gas/hematite interface is:



In the case of oxygen ions migrating inward in the hematite layer, the iron ions and electrons (in excess of requirements for reduction of hematite to magnetite) react with oxygen moving via oxygen vacancies. The reactions for the oxygen ionization and formation of hematite at the hematite/magnetite interface are:



There is a disagreement among researchers regarding the formation of Fe_2O_3 . In contrast to the above model proposed by Birks and Meier (1983), the formation of hematite has been considered only as an oxygen ion migration process (Hauffe, 1954). The later work of Schwenk and Rahmel (1986) concluded that because of experimental difficulties, it is impossible to clearly establish the reactions in which Fe_2O_3 is really formed.

2.4 Iron Scales on Steels

In hot strip mills, using either conventional thick or thin slab casting and rolling technology, the steel is heated above 570 °C. As a result, scales can contain the three iron oxides (wüstite, magnetite and hematite). Due to the high temperatures, wüstite is always present in the hot rolling process. The wüstite point 570 °C can be shifted to higher temperatures by alloying the iron with Mo, Cr and Ni; the wüstite point can be lowered with additions of Mn (Rahmel, 1961). The wüstite phase has a melting point of 1370°C to 1425°C. Melting of the wüstite layer (washing) accelerates the scaling rate, and further increases grain boundary penetration that produces inferior surface quality (Ginzburg and R. Ballas, 2000).

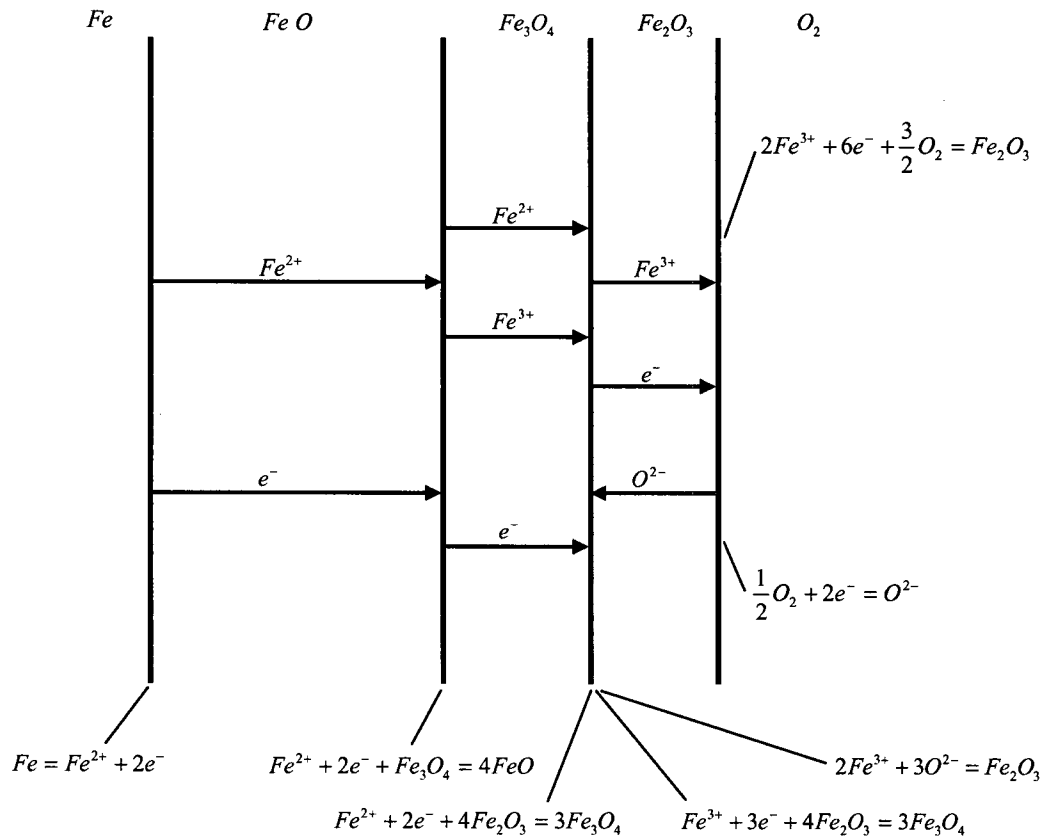


Figure 2.3 Oxidation mechanism of iron to form a three-layered scale of FeO, Fe₃O₄ and Fe₂O₃ above 570°C showing diffusion steps and interfacial reactions (Birks and Meier, 1983).

2.5 Classification of Scales

The scales can be classified as: primary scale, secondary scale and tertiary scale (Blazevic, 1997). The primary scale of around 2 mm is formed in the reheat furnace when the stock is heated for 2 or 3 hours at 1250-1260°C. After reheating, the primary scale is broken up by an edging pass (scale breaker) and removed by water jets in the high pressure hydraulic descaler.

After the first descaling, secondary scale grows fast in the roughing mill. However, the thickness of secondary scale has been found to be less than 100 μm , mostly because of the short time of exposure of the stock surface to the atmosphere during hot rolling (Chen *et al.*, 1993). Due to the changes in surface temperature of the stock, which result from contact with cold rolls and descaling water, the secondary scale is formed in the temperature range 600-1200°C (Krzyzanowski and Beynon, 1999). Secondary scale is removed by high pressure water jets during the reversing rough mill or before the strip enters the finishing mill. In Steckel mills, the descaling of secondary scale is performed before the coil furnace (Ramaswamy *et al.*, 1996). In the descaling operation before the finishing mill, the secondary scale is easily removed (Wolf, October 2000).

Tertiary scale grows in the finishing strip mill at temperatures less than 1000°C (Lenard *et al.* 1999). The tertiary scale is formed between the finishing mill descaler and the first finishing stand, between stands in the finishing strip mill and also after the stock exits the last stand of the finishing strip mill.

2.6 Oxidation Rates

During the initial stage of oxidation, plenty of iron is available to react with the oxidizing gas. As a result, the initial oxidation is controlled by surface reaction, in which the slowest step is the absorption of oxygen into the scale. In this situation, the

scaling rate is linear and constant (Smeltzer, 1960; Tuck *et al.*, 1966; Sachs and Tuck, 1968; Birks and Meier, 1983). As the scale thickens, the amount of iron supplied to the outer surface decreases until it becomes the slowest step and the rate controlling mechanism. In this situation, when the oxidation of iron is diffusion controlled, it obeys a parabolic rate law (Pettit and Wagner, 1964; Tuck *et al.*, 1966; Sachs and Tuck, 1968; Kubaschewski and Hopkins, 1962; Birks and Meier, 1983).

The linear rate of oxidation can be expressed as:

$$\frac{dx}{dt} = k_l \quad (2.10)$$

$$x = k_l t \quad (2.11)$$

where k_l is the linear rate constant, x the oxide thickness and t the oxidation time.

The parabolic rate of oxidation can be expressed as follows:

$$\frac{dx}{dt} = \frac{k_p}{x} \quad (2.12)$$

$$x^2 = k_p t \quad (2.13)$$

where k_p denotes the parabolic rate constant.

The temperature dependence of the parabolic rate of iron obeys an Arrhenius relationship (Kor and Turkdogan, 1971; Smeltzer and Young, 1975):

$$K = K_0 \exp\left(\frac{-Q}{RT}\right) \quad (2.14)$$

where K is the parabolic rate, K_0 a constant, Q the activation energy, R and T are as defined above.

As a result of the Arrhenius relationship, the curves of temperature-metal loss are exponential. For a 1030 steel, the influence of temperature on the metal loss is illustrated in Figure 2.4.

The type of process also influences the oxidation rate. The scale loss due to reheating is about two to four times higher than in a continuous casting operation. This is due to higher surface temperatures and longer holding times that are used in the reheating process (Wolf, July 2000).

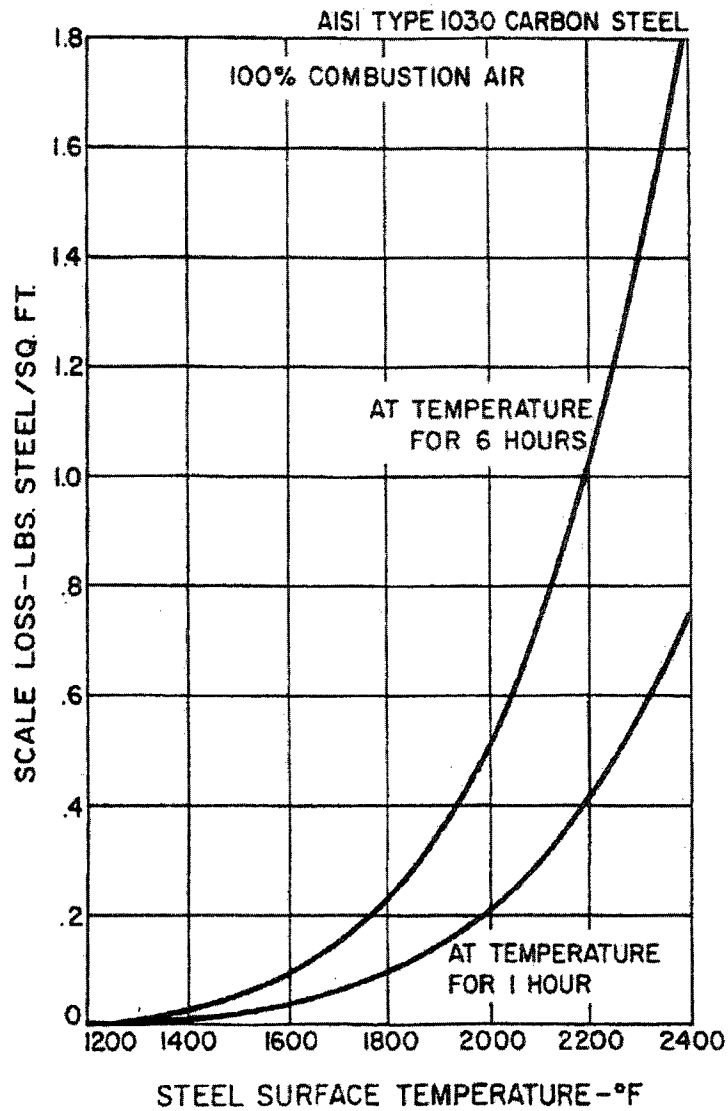


Figure 2.4 Relationship between temperature and metal loss (Cook and Rasmussen, 1970).

2.6.1 Effect of Steel Composition on Oxidation Rate

Carbon – An increase in the carbon content results in a reduction of the oxidation rate (Cook and Rasmussen, 1970; Wolf, March 2000). This reduction of oxidation rate with an increase in carbon content has been attributed to the carbon enrichment in the scale layer that reduces the oxidation of iron (Wolf, March 2000).

Sulphur and Phosphorus – The effect of sulphur on the oxidation rate is insignificant; in contrast, phosphorus lowers the oxidation resistance of iron (Sachs and Tuck, 1968). In Si-added hot-rolled steel sheets, sulphur and phosphorus improve hydraulic descalability by forming a liquid eutectic compound in the scale/steel interface (Fukagawa, 1995, 1997).

Manganese – The iron in wüstite and magnetite can be substituted with manganese; the effects of manganese on the oxidation rate are insignificant (Scheil and Kiwit, 1936).

Silicon – For low carbon steel, the Si content is low, and the effect of Si on the oxidation rate and descalability should not be important. However, in steels with silicon content, the formation of a separate phase of fayalite (Fe_2SiO_4) reduces the oxidation rate (Ginzburg and R. Ballas, 2000). In Si-containing steels, the descaling process is severely affected for the following reasons (Nakamura, 1994):

- (i) High Si-containing steels have bigger pores than low Si-containing steels. In the hydraulic descaling, the large pores formed in the scales of high Si-containing steels result in thick residual scales and in an inferior descalability.
- (ii) In Si-containing steels, fayalite (Fe_2SiO_4) is formed at the interface scale/metal. Fayalite becomes solid at temperatures under 1170°C , which is the eutectic point of Fe_2SiO_4 and FeO . The solid fayalite increases the adhesion of scale on steel, worsening considerably the descalability of Si-containing steels.

Nickel – At the metal/oxide interface, iron diffuses to the wüstite layer while nickel is rejected. Nickel does not tend to diffuse rapidly to the core, forming a nickel-rich surface layer that reduces the oxidation rate (Wolf, April 2000). Asai *et al.* (1997) investigated the addition of nickel in mild steels. They found that nickel modifies the scale/metal interface by making it uneven. Furthermore, they observed that an increase in the unevenness of the scale/metal interface in the steels with high nickel content resulted in a lower descalability than in the steels with low nickel content.

2.6.2 Effect of Heating Atmosphere on Oxidation Rate

In hot strip mills, the heating of the steel is performed in direct-fired furnaces, in which the steel is surrounded by the products of combustion. In perfect conditions (theoretical air-to-gas ratio), the furnace atmosphere is composed of carbon dioxide, water vapour and nitrogen. A deficiency in combustion air results in small quantities of carbon monoxide and hydrogen in the furnace atmosphere, while an excess of combustion air results in some free oxygen. In the furnace atmosphere, the oxidizing gases are oxygen, water vapour and carbon dioxide, and the reducing gases are carbon monoxide and hydrogen. The iron present in the steel reacts with the oxidizing gases through several reactions. At high temperature, the iron and oxygen react, forming iron oxide. The iron and water vapour react to form iron oxide and hydrogen. Iron and carbon dioxide react forming iron oxide and carbon monoxide.

The potential for further work damage from scale formation increases as the amount of scale increases. Therefore, a reduction in the scale formation is desirable. This reduction can be done by monitoring the concentration of free oxygen in the combustion products. In a series of trials, it was concluded that a reduction of 35 % in scale formation is possible when the amount of excess air for combustion is reduced from 70% to about 20% (Abuluwefa *et al.*, 1994).

Cook and Rasmussen (1970) studied the equilibrium products of combustion of natural gas related to percentage of theoretical combustion air, Figure 2.5. They

observed that a gradual decrease in the percentage of combustion air resulted in a transition from oxidizing to reducing atmosphere; in this situation, the free oxygen was absent in the furnace atmosphere and the ratios of CO_2/CO and $\text{H}_2\text{O}/\text{H}_2$ were neutral to iron, Figure 2.6. They also proposed a strategy for scale-free heating, in which the air-gas ratio is reduced as the temperature is increased, Figure 2.7.

Scale-free heating has several advantages, such as an increment in yield, an improvement in product quality, and a reduction in cost in the area of scale removal. However, it must be remembered that some producers insist on scaling to remove surface defects originated in the caster. In terms of disadvantages, it is a process that requires a tight control of the air-gas ratio and temperature. Also, it is a process that requires preheating combustion air or reducing the nitrogen in the combustion air (enriching the combustion air with oxygen) in order to have a suitable flame temperature.

Fuels such as coal, coke and oil contain some sulphur. If these fuels are used in a reheat furnace, the sulphur burns, forming another important constituent of the furnace atmosphere, sulfur dioxide (SO_2). Preece *et al.* (1939) studied the influence of sulphur dioxide on the oxidation rate of plain carbon steel. In their work, it was observed that in the presence of sulphur dioxide, the rate of oxidation accelerates rapidly with diminishing oxygen content (see Figure 2.8). In addition, sulphur dioxide reacts with iron, forming liquid sulphides such as FeS in scale. The sulfides increase the adhesion of the scale on the steel surface, worsening the removal of scale (Rolls, 1963; Birks, 1973).

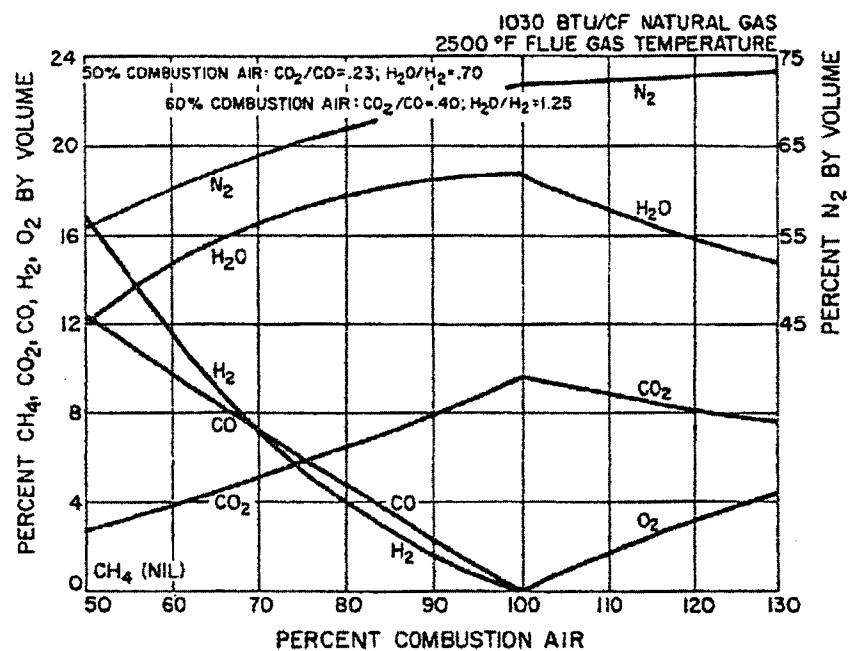


Figure 2.5 Equilibrium products of combustion of natural gas related to percentage of theoretical combustion air (Cook and Rasmussen, 1970).

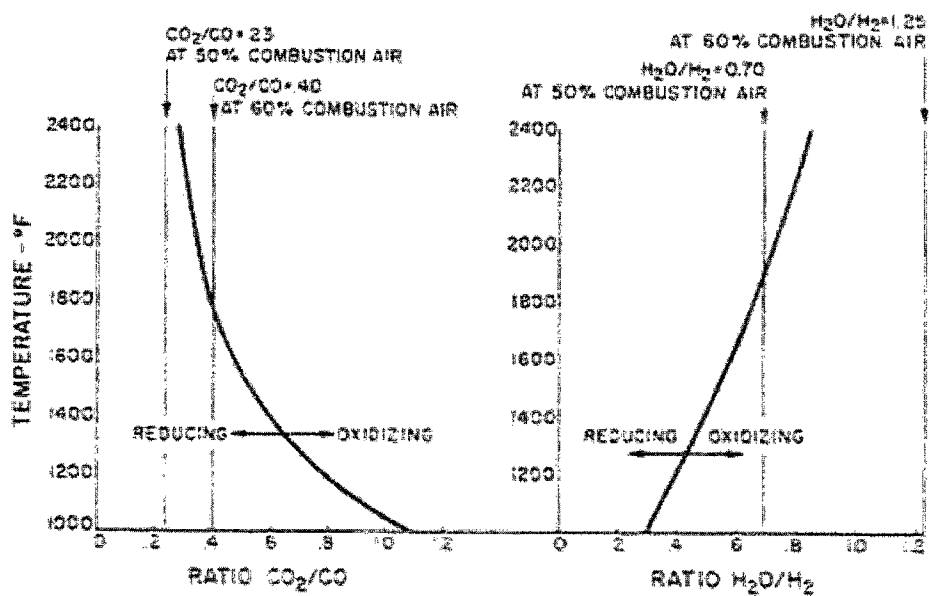


Figure 2.6 As percentage of combustion air decreases, percentage of oxidants decreases, while that of reducers increase (Cook and Rasmussen, 1970).

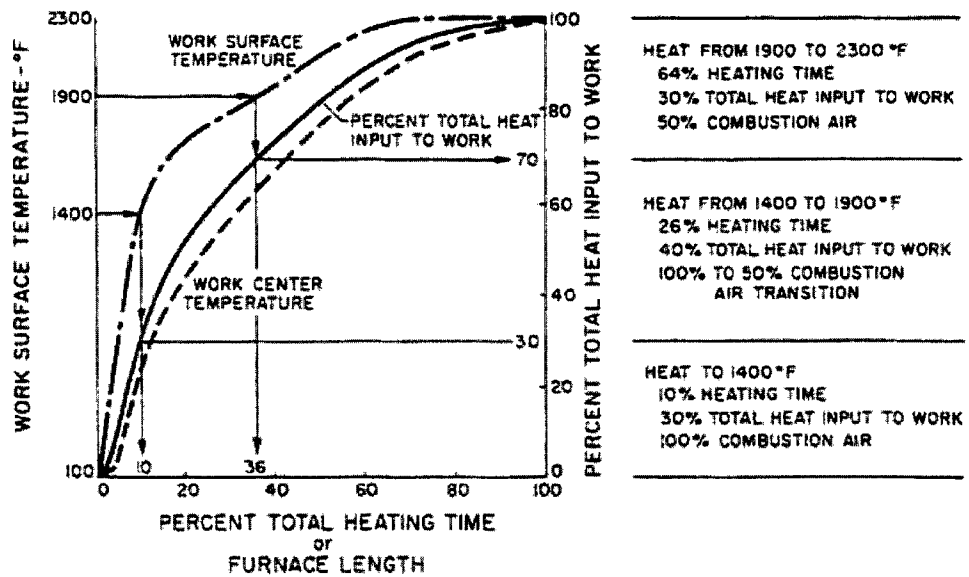


Figure 2.7 Scale-free heating strategy proposed by Cook and Rasmussen (1970).

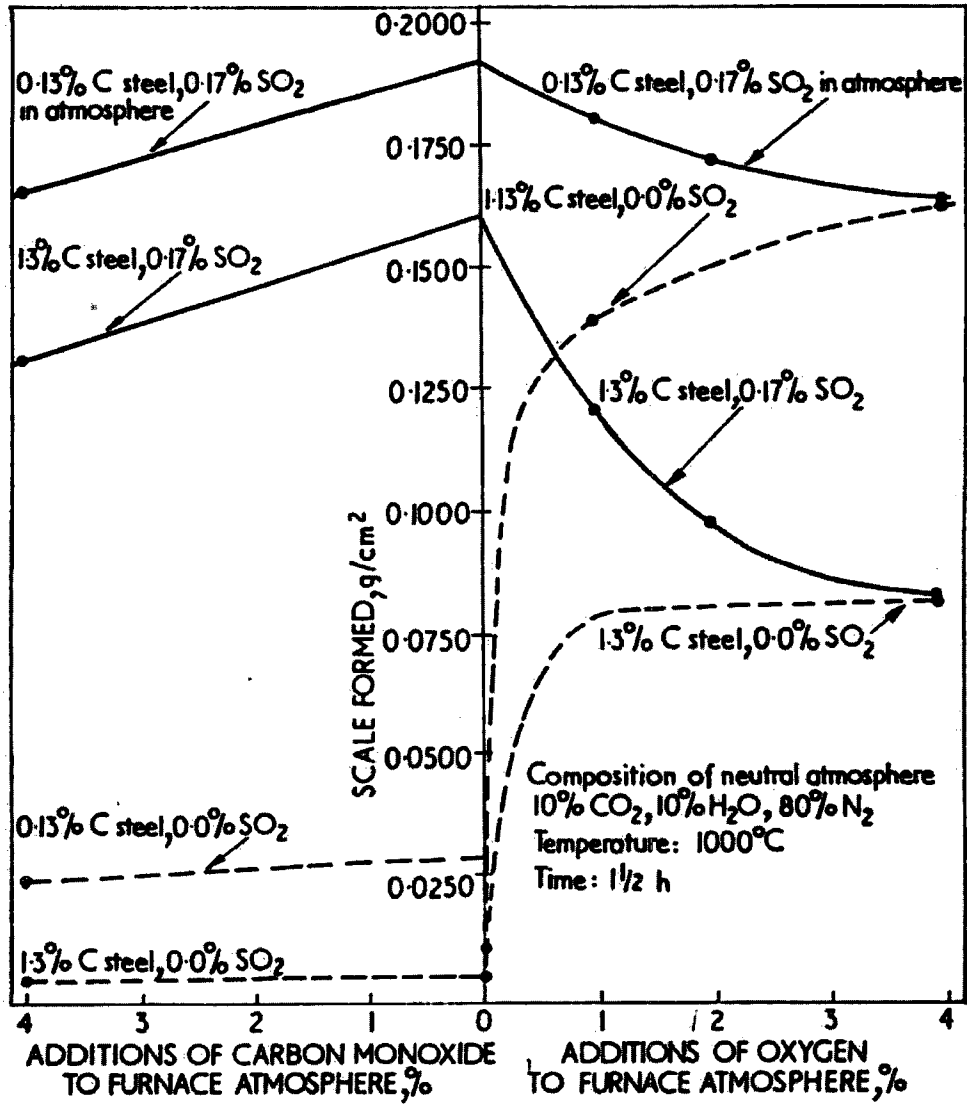


Figure 2.8 Influence of additions of carbon monoxide and oxygen to the neutral atmosphere, free form and also containing 0.17% of sulphur dioxide, on the scaling of plain carbon steel (Preece *et al.*, 1939).

2.6.3 Effect of Gas Velocity on Oxidation Rate

The reactions that occur in the oxidation of steel demand a certain quantity of oxygen. The supply of oxygen depends on the velocity of the gas stream. As a result, the oxidation rate increases until a critical gas velocity is reached, that is, when the rate of oxygen supply becomes equal to the maximum rate at which the oxidizing agent is used. The critical gas velocity for air is 4.2 cm/s (Abuluwefa, 1996), (5 ft/min.) 2.54 cm/s for carbon dioxide, and (23 ft/min.) 11.68 cm/s for steam (Jominy and Murphy, 1930).

2.7 Effect of Scaling on Hot Rolling

Several researchers have investigated the interaction between scales and roll mills. In the concept proposed by Lenard *et al.* (1999), the scale can have two effects. If the scale is soft and ductile, it serves as a lubricant, and if the scale is hard and abrasive, it serves as an abrasive medium in the system steel-scale- roll mill.

El-Kalay and Sparling (1968) found that scale could reduce loads by as much as 25%. They found that thin scale resisted the penetration of the small aspersions of smooth rolls but was penetrated by the aspersions of rough rolls. As a result, sliding friction occurred when rolling thin scale with smooth roll, and sticking friction occurred when rolling thin scale with rough rolls. The sliding friction required lesser load than the sticking friction; therefore, the load was reduced in the rolling of thin scale with smooth roll. It was also reported that thick scale broke up into islands and hot metal extruded between the islands and stuck to the rolls. During hot rolling, the islands moved apart and promoted tensions in the sticking extruded hot metal, thus reducing the load.

Blazevic (1996, 1997) reported that the quality of the final strip surface is influenced by the thickness of the tertiary scales as follows: in the finishing strip mill, the scale that enters the first finishing stand can be thin and hot or thicker and colder. If

the scale is thin and hot, it is plastic and elongates with the metal. In this situation, the scale fractures in fine lines and the hot metal is partially extruded in these fine fractures, resulting in a strip with low rough surface. If the scale is thick, it is colder and less plastic. As a result, the scale cannot elongate with the metal, and a severe fracture occurs in the scale. In this situation, the metal is extruded between scale particles, while the scale particles are pushed into the steel. This results in a strip with a very rough surface.

In the work of Seki *et al.* (1996) blisters and surface defects were investigated, and a mechanism of scale defects was proposed (see Figure 2.9). It was found that a reduction in temperature reduces the scale thickness and prevents scale defects in the finishing strip mill.

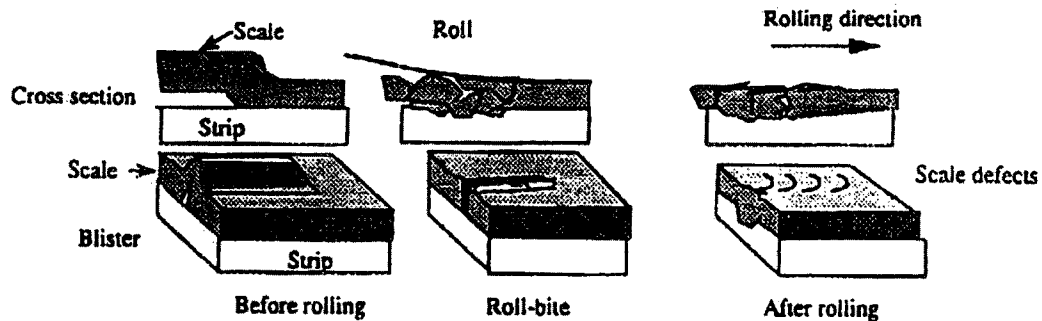


Figure 2.9 Mechanism of scale defects (Seki *et al.*, 1996).

2.8 Hydraulic Descaling in Hot Rolling

In the hot rolling process the scales formed in the different stages are removed by high pressure water jets (descaling operations) to ensure the required quality of the final product. Figure 2.10 illustrates the position of descalers and nozzles in the Bochum hot strip mill (Becker *et al.*, 2000). In this hot strip mill the function of the nozzles of the first descaler is to remove primary furnace scale. The nozzles before and after the roughing stand, the second descaler and the nozzles before the finishing mill remove secondary scale. As the strip enters the finishing mill, the nozzles lower the surface temperature of the strip to prevent the formation of tertiary scale.

Sheppard and Steen (1970) investigated hydraulic descaling of steel oxidized in air. According to them, in hydraulic descaling, the total stress produced in the scale is the product of the thermal stress produced by the cooling action of the water jet, the depositional compression stress (oxidation stress), and the stress due to the impact force of the water jet. In their study, it was observed that scales are removed during hydraulic descaling by the following mechanism:

- (i) A horizontal undercutting (crack) propagates at the scale/steel interface.
- (ii) The scale is fractured on planes normal to the interface forming scale chips.
- (iii) The scale chips are removed by the flow of water.

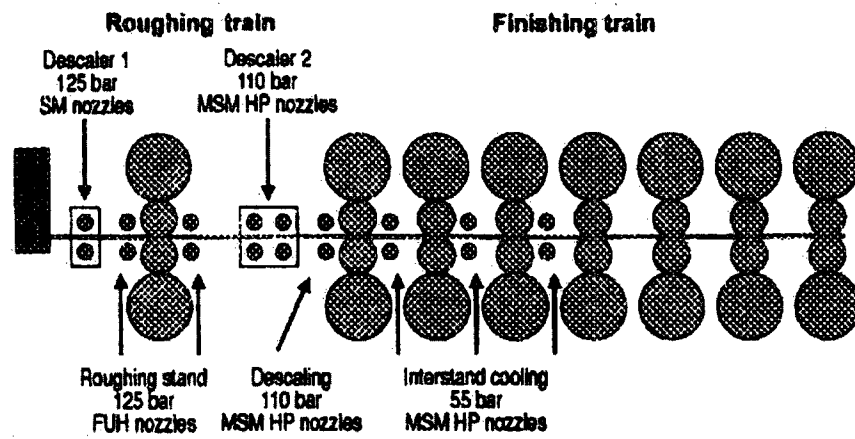


Figure 2.10 Bochum hot strip mill; layout of the descaling equipment (Becker *et al.*, 2000).

2.9 Mechanical Stresses in Scales

Scales formed at high temperature are subject to mechanical stresses. These stresses may result in cracking or spalling of the scale. The stresses can be classified as intrinsic or extrinsic in origin. Intrinsic stresses are due to oxide growth, and extrinsic stresses are due to creep under load or to temperature changes (Robertson and Manning, 1990).

2.9.1 Stresses Arising from Oxide Growth

The model of Pilling and Bedworth (1923) explains the stresses arising from oxide growth (oxidation stresses). In this model, tensile or compressive stresses are related to a change in volume as the metal is converted into oxide. The ratio of the volume per metal ion in the oxide to the volume per metal atom in the metal has commonly been termed PBR, the Pilling-Bedworth ratio. Compressive stress is developed in the oxide when $PBR > 1$, and tensile stress when $PBR < 1$. The Pilling-Bedworth ratio (PBR) for iron oxides is $PBR > 1$ (see Table 2.2). Therefore, during oxide growth, compressive stress is present in the scale.

Another source of stress during oxide growth is the formation of fresh material inside the scale itself. For instance, Jaenicke *et al.* (1964) reported that in the oxidation of copper and gold-copper alloys, the oxygen penetration through a porous layer causes compressive stress in the oxide. Rhines and Wolf (1970) reported that in the high temperature scaling of nickel, anion diffuses in the grain boundary networks of scale and oxidizes the nickel that moves in the bulk of oxide crystals. This results in new oxide upon boundaries of columnar grains and compressive stress in the scale. A similar explanation has been given by Tylecote (1965) in his research concerning the oxidation of iron, nickel, copper and titanium. He suggested that inward oxygen diffusion takes place along the grain boundaries, causing oxidation within the film and oxide growth stresses.

2.9.2 Stresses Arising from Temperature Changes

During cooling from the oxidation temperature, the different thermal expansion coefficient of the oxide and metal substrate generates stresses in the scales. In general, metals have a higher thermal expansion coefficient than oxides. Therefore, scales are under compressive stresses on cooling. The thermal expansion coefficients of some metal substrates, wüstite and hematite, and magnetite are given in Tables 2.3, 2.4 and 2.5, respectively. The transition from inverse spinel structure to normal spinel with increasing temperature results in changes in the thermal expansion coefficient of magnetite; the thermal expansion coefficient increases in the temperature range 400-600°C and then follows at higher temperatures (see Table 2.5).

The stress that arises from temperature change can be estimated with the following equation (Liu *et al.*, 2003):

$$\sigma_{ox} \cong E_{ox}(\alpha_{sub} - \alpha_{ox})\Delta T \quad (2.15)$$

where σ_{ox} is the stress in the oxide, E_{ox} is the Young's modulus of oxide, α_{sub} the thermal expansion coefficient of the metal substrate, α_{ox} the thermal expansion coefficient of the oxide and ΔT the temperature change.

Table 2.2 PBR values for iron oxides.

System	PBR	Reference
FeO/ α -Fe	1.68	Hancock and Hurst, 1970
FeO/Fe	1.78	Jones, 1996
FeO/Fe	1.7	Stringer, 1996
FeO/Fe	1.7	Kofstad, 1988
Fe ₃ O ₄ / α -Fe	2.1	Hancock and Hurst, 1970
Fe ₂ O ₃ / α -Fe	2.14	Hancock and Hurst, 1970
Fe ₃ O ₄ /FeO	1.2	Hancock and Hurst, 1970
Fe ₂ O ₃ /Fe ₃ O ₄	1.02	Hancock and Hurst, 1970

Table 2.3 Thermal expansion coefficients of some metal substrates.

Substrate	Coefficient 10 ⁻⁶	Temperature range (°C)	Reference
Fe	15.3	0-900	Tylecote, 1960
Mild steel	16.2	400-800	Robertson and Manning, 1990
Type 316 steel	18.3	400-800	Robertson and Manning, 1990

Table 2.4 Thermal expansion coefficients of FeO and Fe₂O₃.

Oxide	Coefficient 10 ⁻⁶	Temperature range (°C)	Reference
FeO	12.2	100-1000	Tylecote, 1960
FeO	15.0	400-800	Robertson and Manning, 1990
FeO	15.2	100-1000	The Oxide Handbook, 1982
Fe ₂ O ₃	13.9	400-800	Robertson and Manning, 1990
Fe ₂ O ₃	14.9	20-900	Tylecote, 1960
Fe ₂ O ₃	12.5	100-1200	The Oxide Handbook, 1982

Table 2.5 Thermal expansion coefficients of Fe₃O₄ (Manning and Metcalfe, 1977).

F ₃ O ₄ coefficient x 10 ⁻⁶	Temperature range (°C)
11.25	0-50
11.65	50-100
12.15	100-150
12.60	150-200
13.05	200-250
13.70	250-300
14.25	300-350
14.80	350-400
15.60	400-450
17.45	450-500
24.00	500-550
24.50	550-600
16.50	600-650

**Chapter
Three**

**Phase Composition of Oxide Scales
during Reheating**

3.1 Introduction

In hot strip mills, reheating furnaces are used to heat slabs prior to hot working. In reheating operations, scales are formed when the steel surface reacts with the furnace atmosphere. During hot rolling, scales can generate surface defects. To prevent these defects, scales are removed by mechanical and/or hydraulic descaling.

The iron oxides are different in crystal structures (Villars and Calvert, 1991), density (The Oxide Handbook, 1982), thermal properties (Schütze, 1997; The Oxide Handbook, 1982), thermodynamic properties (The Oxide Handbook, 1982) and mechanical properties (Schütze, 1997; The Oxide Handbook, 1982). Thus, the determination of the amount of each phase present in the scale is of great interest in order to better understand the relation between scale composition and descaling.

Scale formation during reheating has been studied extensively because of its industrial importance. Several researchers have reported changes in the phase composition of the scales. As early as 1939, Preece *et al.* reported that at 1000°C, a crystalline scale composed only of wüstite formed on the surface of plain carbon steel in a 10CO₂-10H₂O-80N₂ atmosphere. They observed that additions of free oxygen of more than 1% to the previous atmosphere resulted in a transition from the crystalline scale to the classical three-layer scale. In carbon dioxide atmospheres, Smeltzer (1960) found that at temperatures below the Curie point of iron, the scale formed on pure iron consisted of wüstite and magnetite, while at high temperatures the scale consisted only of wüstite. Tuck *et al.* (1966) reported that in temperatures ranging from 850 to 1000°C, classical three-layer scales grew on pure iron and mild steel in air and oxygen. Furthermore, they noted that in a carbon dioxide atmosphere, the scale consisted only of wüstite; although after it reached a certain thickness, magnetite was also formed. Sheasby *et al.* (1984) observed that after 10 min. of oxidation of pure iron at 1200°C in a 20H₂O-N₂ gas mixture, the scale consisted only of wüstite, while in a 4O₂-20H₂O-N₂ gas mixture the scale had the classical three-layered formation. In an analysis by neutron diffraction of the oxidation of mild steel at high temperature in oxygen-nitrogen gas mixtures, Abuluwefa (1996) found that a rise in the oxygen concentration increased

the fractions of magnetite and hematite in the scale. In 1997, Abuluwefa *et al.* found that in gases containing free oxygen, the main oxidizing agent is the free oxygen and additions of carbon dioxide and water vapour have little effect on the magnitude of the initial oxidation rates. This indicates that future studies of scale formation during reheating should be done in dilute atmospheres containing some free oxygen. Although previous works carried out in pure carbon dioxide (Smeltzer, 1960; Tuck *et al.*, 1966), water vapour (Tuck *et al.*, 1966), oxygen (Tuck *et al.*, 1966; Bohnenkamp and Engell, 1959) and air (Tuck *et al.*, 1966) have contributed to a better understanding of surface oxidation of steel, they do not represent the oxidizing conditions during reheating operations, which are usually carried out in dilute atmospheres composed mainly of some free oxygen, carbon dioxide, water vapour and nitrogen.

With the exception of the work by Abuluwefa (1996) mentioned above, previous works in dilute atmospheres have used metallographic analyses to study the changes in the phase composition of the scales (Preece *et al.*, 1939; Sheasby *et al.*, 1984). The accuracy of metallographic analyses is questionable, whereas alternative X-ray diffraction techniques offer potential for greater accuracy and rapid analysis (Biederman *et al.*, 1974). In this chapter, quantitative phase analyses of scales formed in dilute atmospheres containing some free oxygen are carried out in order to better understand the phase composition of scales in industrial furnaces. Understanding phase composition will allow the development of more accurate models of scale formation and descaling. This may lead to a better hot rolling technology.

3.2 Objectives

The objective of this chapter is to investigate:

- 1 - The phase composition of scales formed in O_2 - CO_2 - H_2O - N_2 , O_2 - H_2O - N_2 and O_2 - CO_2 - N_2 gas mixtures under conditions similar to those of reheating furnaces in hot strip mills.

- 2 - The effect of free oxygen, carbon dioxide and water vapour on the phase composition of the scales.
- 3 - The influence of oxidation time and temperature on the phase composition of scales.
- 4 - The influence of scale morphology on the phase composition of scales.

3.3 Experimental

3.3.1 Sample Preparation

The chemical composition of the low carbon steel samples is shown in Table 3.1. The dimensions of the samples for the phase composition analysis were 30 mm in width, 70 mm in length, and 1 to 3 mm in thickness; the additional samples for microscopic observations were 15 mm in width, 20 mm in length, and 3 mm in thickness. For the oxidation test, the samples were polished with SiC paper and cleaned with alcohol. The oxidation rate increases with the gas velocity until a critical gas velocity is reached. The critical gas velocity for air is 4.2 cm/s (Abuluwefa, 1996), (5 ft/min.) 2.54 cm/s for carbon dioxide and (23 ft/min.) 11.68 cm/s for steam (Jominy and Murphy, 1930). In this study, a gas velocity of 11.7 cm/s was used to ensure high oxidizing conditions in the oxidation tests.

Table 3.1 Chemical composition of the steel (wt %).

C	Mn	Si	Cu	P	S	Ni	Mo	V	Sn	Cr
0.06	0.32	0.007	0.028	0.005	0.009	0.01	0.001	0.001	0.004	0.026

A tubular horizontal furnace (Model Mellen Microtherm 1300°C) was used to heat the samples in an argon atmosphere to 1000, 1050, 1100, 1150, 1200 and 1250°C. The argon was then replaced by the gas mixtures shown in Table 3.2. A gas analyzer (Model Nova 376WP) that allows simultaneous measurements of O₂, CO₂, CO and NO_x (as NO) was used to obtain the different gas mixtures. In this gas analyzer, O₂, CO and NO sensors are electrochemical “fuel cell” type sensors, while a small micro infrared detector is used for measuring CO₂ (Nova, 1997). The desired gas mixtures of O₂, CO₂ and N₂ were obtained by controlling the flow of dry air, carbon dioxide and nitrogen. In the case of the water vapour-containing gas mixtures O₂-CO₂-H₂-N₂, the water vapour was added by passing the gas mixtures through a sealed water-heated container.

After isothermal oxidation of 12, 30, 60 and 120 min., the samples for the phase composition analysis were quenched in water in order to avoid the decomposition of wüstite. During the quenching process, the oxide partially detached from the steel due to stresses induced by temperature changes. The remaining oxide was removed by uniaxial tensile loading with a Tinius Olsen tensile tester (Model H25K-S). After removal, the oxide was ground to a fine powder for quantitative X-ray diffraction phase analysis. For phase composition analysis, quenching is the most suitable procedure to avoid the decomposition of wüstite. Nevertheless, quenching tends to fracture the oxide, masking the original morphology at high temperature. Therefore, the additional samples for microscopic observations were oxidized and fast cooled with a flow of argon. Fast cooling with a flow of argon avoids fracturing of the scale while reducing the decomposition of wüstite. After fast cooling with a flow of argon, scale/steel cross-sections were hot mounted in a resin and polished with SiC paper to a 1200 grit surface finish. Colloidal silica of 0.05 μm was then used in the final stage. The scale/steel cross-sections were observed with an optical microscope equipped with an image analyzer.

Table 3.2 Temperatures (°C) and gas mixtures (v%) used to oxidize the low carbon steel.

Temp. (°C)	% O ₂	% CO ₂	% H ₂ O	% N ₂
1000	1	15	10	74
1000	5	15	10	70
1050	1	15	10	74
1050	5	15	10	70
1100	1	15	10	74
1100	1	---	10	89
1100	1	15	---	84
1100	5	15	10	70
1100	5	---	10	85
1100	5	15	---	80
1150	1	15	10	74
1150	5	15	10	70
1200	1	15	10	74
1200	5	15	10	70
1250	1	15	10	74
1250	1	---	10	89
1250	1	15	---	84
1250	5	15	10	70
1250	5	---	10	85
1250	5	15	---	80

3.3.2 Quantitative Phase Analysis by X-ray Diffraction

The diffractometry was carried out in a Rigaku Dmax III X-ray diffractometer with Bragg–Brentano parafocusing geometry, Figure 3.1(a). The diffractometer was equipped with a copper rotating anode X-ray source. The goniometer has four slit positions: the divergence slit (DS), the scatter slit (SS), the receiving slit (RS) and the receiving slit monochromator (RSm), Figure 3.1(b). The X-ray source was obtained by a conventional copper target X-ray tube set to 40 KV and 130 mA. A diffracted beam graphite monochromator tuned to Cu $K\alpha$ radiation was used to collect the diffraction patterns from $5\text{-}80^\circ 2\theta$ at a rate of $2^\circ/\text{min}$.

The principle of X-ray diffraction analysis is based on Bragg's law for the reflection of radiation by the crystal lattice. Bragg's law is expressed as:

$$\lambda = 2d \sin \theta \quad (3.1)$$

where λ = wavelength of incident beam, d = distant between planes and θ = the angle between the incident radiation and the diffracting plane (Bragg angle).

The intensity of the diffracted X-ray can be used to calculate interplanar spacings and to determine the crystal structure in an investigated specimen. The direct comparison method was used for the quantitative phase analysis. The method is based on the fact that the intensity of a diffraction pattern of a particular phase is proportional to the content of that phase in a mixture of phases. Since its creation by Averbach and Cohen (1948), the direct comparison method has been used to measure the amount of retained austenite in hardened steel, and to solve other analytical problems.

The intensity diffracted by a single-phase powder specimen can be expressed as follows (Cullity, 1978):

$$I = \left(\frac{I_0 A \lambda^3}{32\pi r} \right) \left[\left(\frac{u_0}{4\pi} \right)^2 \frac{e^4}{m^2} \right] \left(\frac{1}{v^2} \right) \left[|F|^2 p \left(\frac{1 + \cos^2 2\theta}{\sin^2 \theta \cos \theta} \right) \right] \left(\frac{e^{-2M}}{2\mu} \right) \quad (3.2)$$

where I = integrated intensity (joules $\text{sec}^{-1}\text{m}^{-1}$), I_0 = intensity of incident beam (joules $\text{sec}^{-1}\text{m}^{-2}$), A = cross sectional area of incident beam (m^2), λ = wavelength of incident beam (m), r = radius of diffractometer circle (m), $\mu_0 = 4\pi \times 10^{-7} \text{ m kg C}^{-2}$, e = charge on electron (C), m = mass of electron (kg), v = volume of unit cell (m^3), F = structure factor, p = multiplicity factor, θ = Bragg angle, e^{-2M} = temperature factor and μ = linear absorption coefficient (m^{-1}), which enters as the absorption factor $1/2\mu$. For the derivation of this equation, the reader is referred to the text by James (1962).

If K_2 and R are defined as follows:

$$K_2 = \left(\frac{I_0 A \lambda^3}{32\pi r} \right) \left[\left(\frac{u_0}{4\pi} \right)^2 \frac{e^4}{m^2} \right] \quad (3.3)$$

$$R = \left(\frac{1}{v^2} \right) \left[|F|^2 p \left(\frac{1 + \cos^2 2\theta}{\sin^2 \theta \cos \theta} \right) \right] \left(e^{-2M} \right) \quad (3.4)$$

Then, Eq. (3.2) can be written as:

$$I = \frac{K_2 R}{2\mu} \quad (3.5)$$

In a mixture of wüstite (W), magnetite (M) and hematite (H), Eq. (3.5) can be expressed as (Biederman *et al.*, 1974):

$$I_W = \frac{K_2 R_W C_W}{2\mu_m} \quad (3.6)$$

$$I_M = \frac{K_2 R_M C_M}{2\mu_m} \quad (3.7)$$

$$I_H = \frac{K_2 R_H C_H}{2\mu_m} \quad (3.8)$$

where C_W , C_M and C_H are the volume fraction of wüstite, magnetite and hematite in the mixture and μ_m is the linear absorption coefficient of the mixture.

In Eqs. (3.6)-(3.8) K_2 is a constant, independent of the kind and amount of the diffracting substance, thus:

$$\frac{I_W}{I_M} = \frac{R_W C_W}{R_M C_M} \quad (3.9)$$

$$\frac{I_W}{I_H} = \frac{R_W C_W}{R_H C_H} \quad (3.10)$$

$$\frac{I_M}{I_H} = \frac{R_M C_M}{R_H C_H} \quad (3.11)$$

The value of I_W , I_M and I_H can be measured from the diffractometer pattern, R can be calculated from Eq. (3.4), and with the additional relationship:

$$C_W + C_M + C_H = 1 \quad (3.12)$$

Then, the value of C_W is given by:

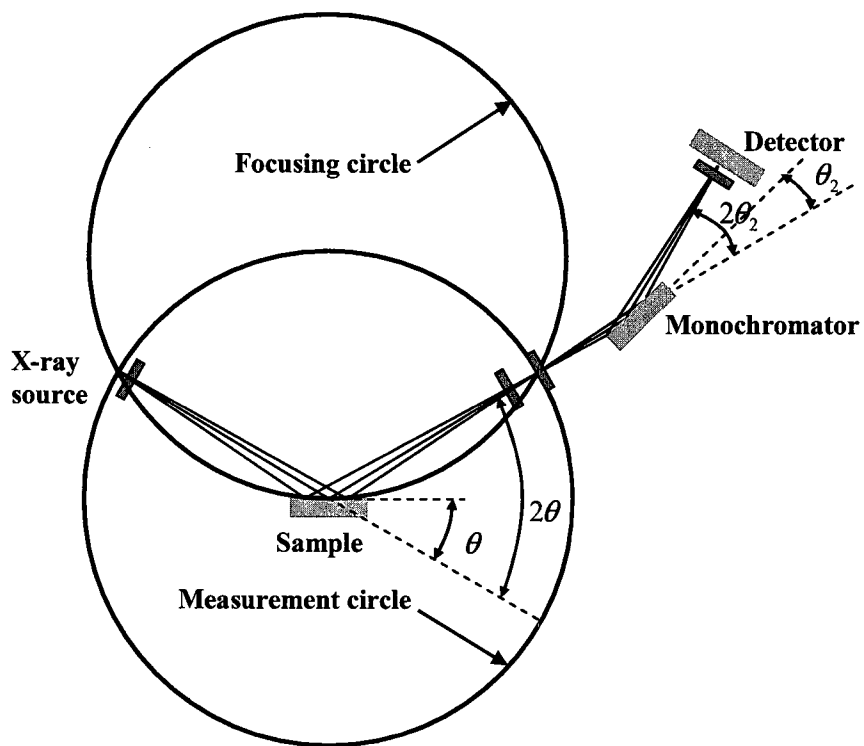
$$C_W = \frac{1}{1 + \frac{R_W I_M}{R_M I_W} + \frac{R_W I_H}{R_H I_W}} \quad (3.13)$$

Similar analyses give the concentrations of magnetite and hematite:

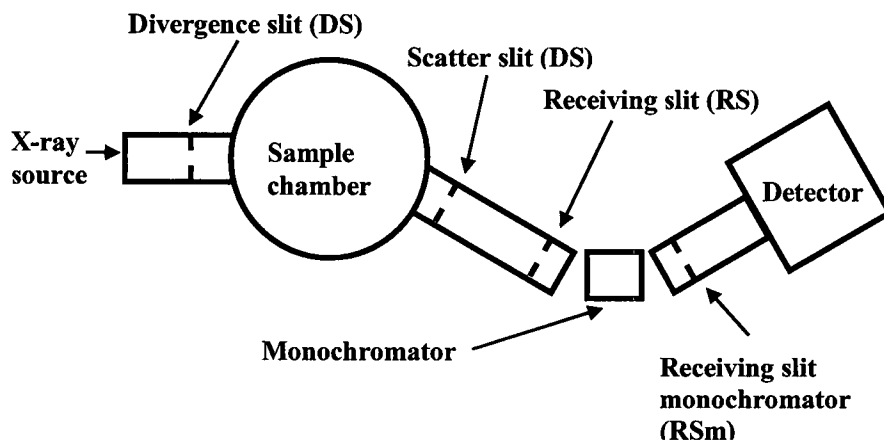
$$C_M = \frac{1}{1 + \frac{R_M I_H}{R_H I_M} + \frac{R_M I_W}{R_W I_M}} \quad (3.14)$$

$$C_H = \frac{1}{1 + \frac{R_H I_W}{R_W I_H} + \frac{R_H I_M}{R_M I_H}} \quad (3.15)$$

The data obtained from the X-ray analysis was converted to computer spreadsheets and graphs with Microsoft Excel 2000. Then, Adobe Photoshop 5.0 (Adobe Systems Incorporated, San Jose, CA) was used to convert the graphs to JPG images with a resolution of 28.346 pixels/cm. The areas under each diffraction peak or integrated intensities I_W , I_M and I_H were measured in the JPG images with the image analyzer software (Vision PE 5.0, Clemex). The R factor for the reflections used in the phase analysis (111) FeO, (200) FeO, (220) Fe₃O₄, (400) Fe₃O₄, (104) Fe₂O₃ and (113) Fe₂O₃ is shown in Table 3.3. Depending on the scale composition, the number of the selected reflections for the phase analysis varied from two to six. The selected reflections for the phase analysis are presented in Tables (A.2)-(A.7) in Appendix B.



a)



b)

Figure 3.1 Schematic diagram of: a) Bragg-Brentano geometry, b) diffractometer.

Table 3.3 *R factor intensity analysis.*

<i>hkl</i> *	2θ *	$\sin \theta$	F^2 **	p **	ν^2 **	<i>R</i>
(111) FeO	36.04	0.3093	2544	8	6383	57.9459
(200) FeO	41.92	0.3577	8339	6	6383	101.918
(220) Fe ₃ O ₄	30.10	0.2595	22983	12	350287	21.1581
(400) Fe ₃ O ₄	43.12	0.3669	93754	6	350287	19.6711
(104) Fe ₂ O ₃	33.27	0.2862	12304	12	90546	35.2834
(113) Fe ₂ O ₃	40.96	0.3498	6967	12	90546	12.643

* Obtained from 6-0615, 11-614 and 13-534 JCPDS cards (1974).

** Taken from Biederman *et al.* (1974).

3.4 Results and Discussion

Figure 3.2 illustrates some of the oxide powder diffraction patterns obtained in this study. The composition of scales was influenced by the free oxygen, water vapour, temperature and oxidation time. Carbon dioxide showed a small influence at 1100°C, and a negligible one at 1250°C.

Two types of scale were observed in the present work:

- (i) The first type called throughout the text “crystalline scale” has a surface made up of crystal facets and has a crystalline appearance. This crystalline scale is composed mostly of wüstite and a negligible amount of magnetite, Figure 3.3(a).
- (ii) The second type is the classical three-layer scale, composed of wüstite, magnetite and hematite, Figure 3.3(b). The classical three-layer scale is crystalline as well, but it doesn't have a surface with a crystalline appearance.

The gas mixtures, oxidation times and temperatures at which each scale was observed are illustrated in Figures (3.4)(3.5)(3.7). The crystalline scale with an irregular outer surface is commonly observed when pure iron is oxidized in carbon dioxide (Sachs and Tuck, 1968), and when steel is oxidized in pure carbon dioxide and in oxidizing atmospheres diluted sufficiently with nitrogen (Preece *et al.*, 1939). Sachs and Tuck (1968) attributed the formation of the irregular outer surface to the formation of idiomorphic crystals at the surface. They hypothesized that during the initial oxidation in dilute atmospheres, the rate-controlling mechanism is the surface reaction, hence the adsorption of oxygen atoms or absorption of ions would occur faster at preferred planes of the oxide crystal, leading to idiomorphic crystals at the surface and a scale with an irregular outer surface.

After 60 min. of oxidation at 1150, 1200 and 1250°C in 1O₂-15CO₂-10H₂O-N₂ mixture, and at 1250°C in 1O₂-10H₂O-N₂ mixture, a transition occurred from the initial

crystalline scale with an irregular outer surface to the classical three-layer scale. This transition was due to an increase in the oxide thickness with time. As the oxide thickened, the diffusion of iron slowed down, and a change in the rate-controlling mechanisms occurred when the diffusion of iron was slower than the incorporation of oxygen to the scale. In this situation, the rate-controlling mechanism changed from being the surface reaction and became the diffusion of iron. Consequently, idiomorphic oxide growth no longer occurred, and posterior oxidation in the scale with an irregular outer surface was faster in the thin areas of the scale than in the thick areas until the scale developed equal thickness, forming the classical three-layer scale.

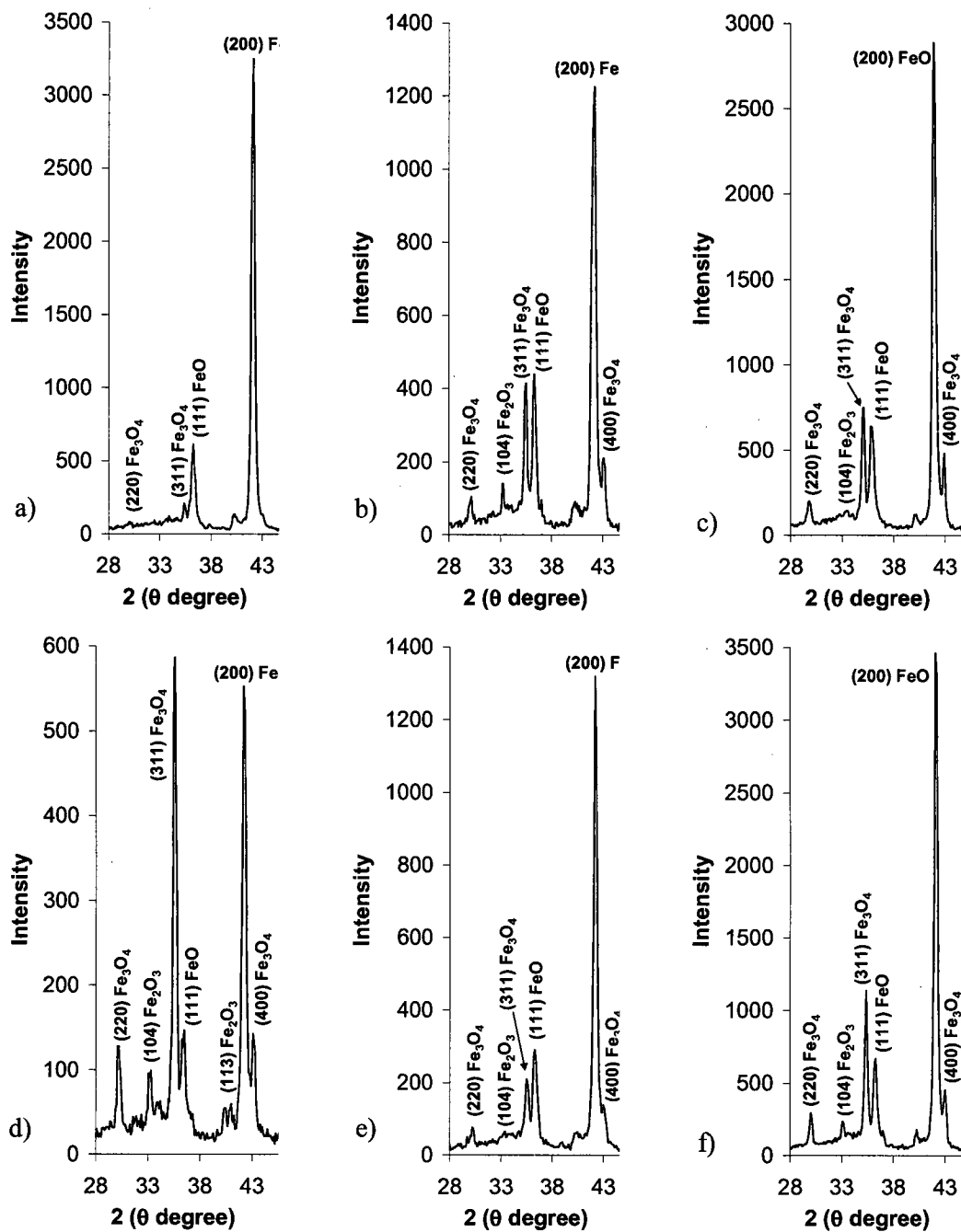


Figure 3.2 Oxide powder diffraction patterns illustrating the influence of: free oxygen a), c); carbon dioxide c), e); oxidation time a), b); water vapour b), d); temperature a), f). The scales were formed in: a) $1\text{O}_2\text{-}15\text{CO}_2\text{-}10\text{H}_2\text{O-N}_2$ for 12 min. at 1250°C , b) $1\text{O}_2\text{-}15\text{CO}_2\text{-}10\text{H}_2\text{O-N}_2$ for 120 min. at 1250°C , c) $5\text{O}_2\text{-}15\text{CO}_2\text{-}10\text{H}_2\text{O-N}_2$ for 12 min. at 1250°C , d) $1\text{O}_2\text{-}15\text{CO}_2\text{-N}_2$ for 120 min. at 1250°C , e) $5\text{O}_2\text{-}10\text{H}_2\text{O-N}_2$ for 12 min. at 1250°C , f) $1\text{O}_2\text{-}15\text{CO}_2\text{-}10\text{H}_2\text{O-N}_2$ for 12 min. at 1050°C .

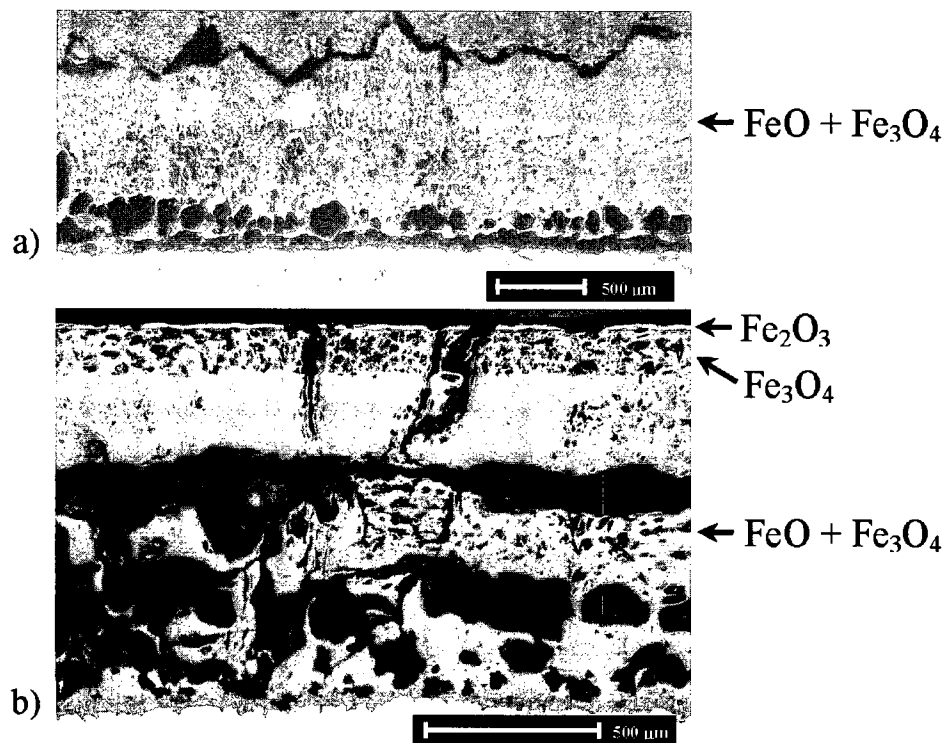


Figure 3.3 Scales formed at 1250°C for 60 min. in: a) 1O₂-15CO₂-10H₂O-N₂, crystalline scale with an irregular outer surface; b) 5O₂-15CO₂-10H₂O-N₂, classical three-layer scale. During cooling with a flow of argon, some wüstite decomposed resulting in the precipitation of magnetite in the wüstite layer.

Figure 3.4 show the mole fraction of the iron oxides grown in the low oxygen content gas mixture $1\text{O}_2-15\text{CO}_2-10\text{H}_2\text{O}-\text{N}_2$ and in the high oxygen content gas mixture $5\text{O}_2-15\text{CO}_2-10\text{H}_2\text{O}-\text{N}_2$. The error of the phase analysis is presented in Tables (A.2)(A.3) in Appendix B. As the percentage of the free oxygen in the gas mixture was increased from 1% to 5%, higher percentages of magnetite and hematite were present in the scale, Figures 3.4(a)-(h). These results correspond with the observations mentioned above of Preece *et al.* (1939), Sheasby *et al.* (1984) and Abuluwefa (1996), which indicated that a rise in free oxygen increases the presence of magnetite and hematite in the scale. After 12 min. of isothermal oxidation in both low and high oxygen content gas mixtures, scales of less than 300 μm in thickness offered little resistance to the diffusion of iron. A high concentration of iron formed scales with a high percentage of wüstite (the most iron-rich oxide). As the oxidation time was prolonged to 30, 60 and 120 min., the scale thickened, slowing down iron diffusion and restricting the supply of iron. As a result, the concentration of iron decreased, reducing the percentage of wüstite, while the percentages of magnetite and hematite increased. The highest percentages of wüstite were observed at 1200 and 1250°C. The rate of lattice diffusion (predominant at high temperatures) increases exponentially with increases in temperature (Mrowec, 1980). Therefore, at 1200 and 1250°C, the concentration of iron at the surface and the percentage of wüstite were high despite a thick scale (up to 2 mm in thickness).

In hot strip mills using thin slab casting and rolling technology, a thin scale of around 200 μm in thickness is formed on the surface of the steel during reheating operations (Donini *et al.*, 1997). In this type of hot strip mill, tunnel furnaces are the central link between the caster and rolling mill. They are used to heat and/or equalize the slab temperature in reheating operations of about 12-20 min. In general, tunnel furnaces operate over the temperature range of 1000-1200°C. Typical delivery temperatures are in the range of 1050-1150°C (Ramírez-Cuellaret *et al.*, 2003). In this type of hot strip mill, the experiments indicated that reheating at high temperatures for short times results in thin scales rich in wüstite with either the crystalline structure or the classical three-layered formation, Figures 3.4(a)(b)(e)(f). Tunnel furnaces can hold slabs and act as a buffer during mill delays (Skagen and Gilbert, 1995). If a delay occurs, the phase composition of the scales changes with the length of the delay,

temperature and furnace atmosphere. Generally, the experiments indicated that during a mill delay the scale thickens, reducing the percentage of wüstite, while the percentages of magnetite and hematite increase.

In hot strip mills using the traditional thick slab casting and rolling technology, a thick scale of around 2 mm is formed on the surface of the steel during reheating operations. Slabs can be charged in the furnace at different temperatures, cold (from the slab yard) or hot (directly from the continuous caster). The slabs are then reheated to 1250-1260°C in approximately 2 to 3 hours. In this type of hot strip mill, the experiments showed that reheating at high temperatures for prolonged times are likely to form a scale rich in wüstite with the classical three-layered formation in both low and high oxygen content atmospheres, Figures 3.4(d)(h).

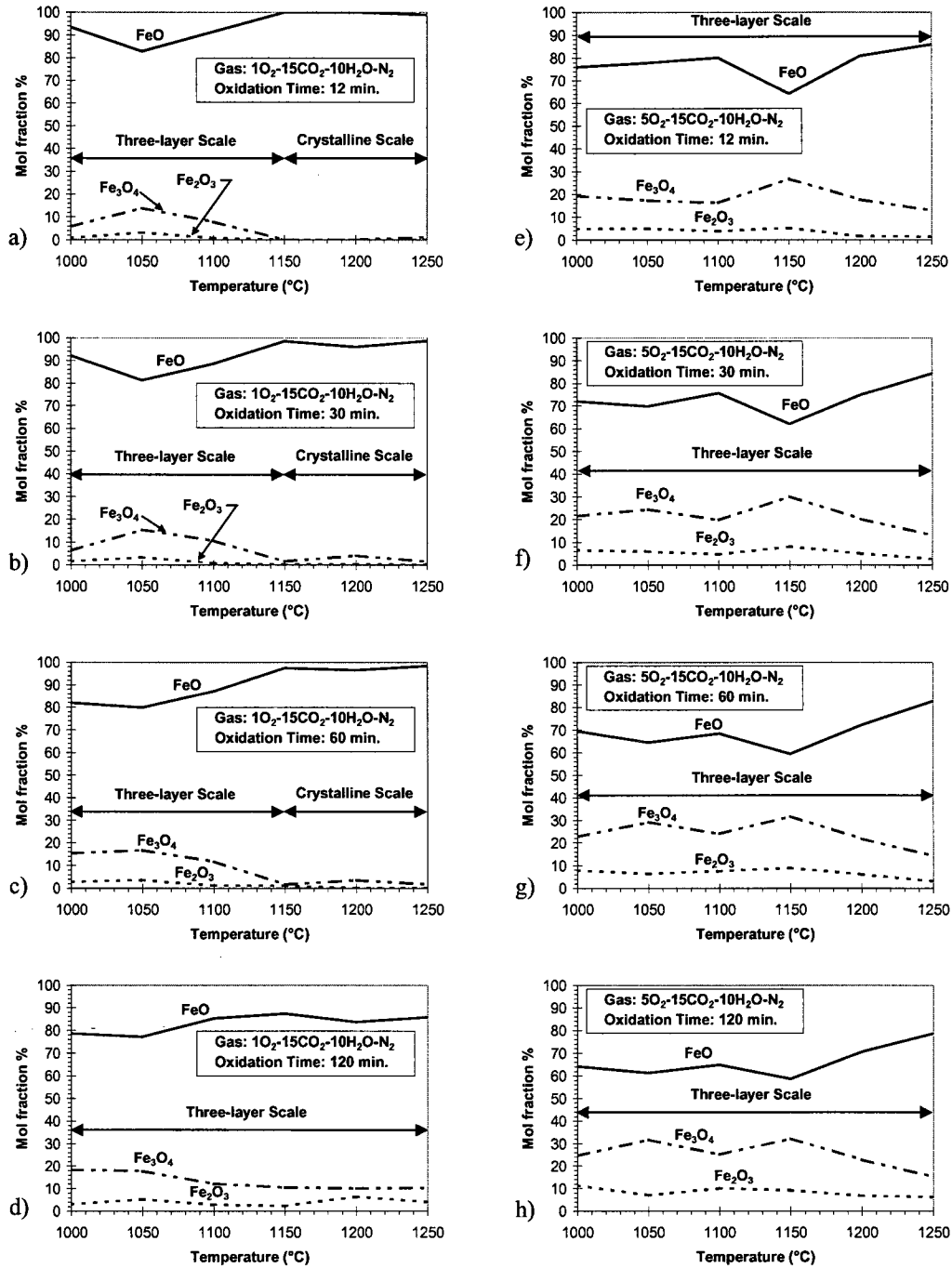


Figure 3.4 Effect of free oxygen, oxidation time and temperature on the percentages of FeO, Fe₃O₄ and Fe₂O₃ in the scales formed on low carbon steel. Samples a), b), c), d) oxidized in 10O₂-15CO₂-10H₂O-N₂ for: a) 12 min., b) 30 min., c) 60 min., d) 120 min.; samples e), f), g), h) oxidized in 5O₂-15CO₂-10H₂O-N₂ for: e) 12 min., f) 30 min., g) 60 min., h) 120 min.

Figures 3.5(a)(b) are included for comparison purposes. They represent the mole fraction of the iron oxides shown in Fig. (3.4) for scales formed at 1100°C in low 1O_2 - 15CO_2 - $10\text{H}_2\text{O}$ - N_2 and in high 5O_2 - 15CO_2 - $10\text{H}_2\text{O}$ - N_2 oxygen content gas mixtures, respectively.

Figures 3.5(c)(d) display the mole fraction of the iron oxides at 1100°C in carbon dioxide-free atmospheres: 1O_2 - $10\text{H}_2\text{O}$ - N_2 and 5O_2 - $10\text{H}_2\text{O}$ - N_2 mixtures, respectively. The error of the phase analysis is presented in Tables (A.5)(A.7) in Appendix B. The absence of CO_2 resulted in a small influence on the phase composition at 1100°C (see Figures 3.5(a)(c) and Figures 3.5(b)(d)).

Figures 3.5(e)(f) show the mole fraction of the iron oxides at 1100°C in water vapour-free atmospheres: 1O_2 - 15CO_2 - N_2 and 5O_2 - 15CO_2 - N_2 mixtures, respectively. The error is presented in Tables (A.4)(A.6) in Appendix B. The scale formed in water vapour-containing atmospheres is more plastic and creeps easily, enhancing the contact of the oxide to the metal substrate (Sachs and Tuck, 1968; Tuck *et al.*, 1969; Hedden and Lehmann, 1964). In contrast, the absence of water vapour forms an oxide that loses contact with metal substrate (Sheasby *et al.*, 1984; Sachs and Tuck, 1968; Tuck *et al.*, 1969). This explains the gap formation near the scale/steel interface in the scales grown in the absence of water vapour, Figure 3.6. In the presence of gaps, the diffusion of iron is considerably slower, and magnetite grows into the wüstite layer (Sachs and Tuck, 1968). The presence and size of the gaps increased as the oxidation time was extended. Therefore, as the oxidation time increased, the absence of water vapour resulted in a reduction in the percentage of wüstite while increasing the percentages of magnetite and hematite (see Figures 3.5(a)(e) and Figures 3.5(b)(f)).

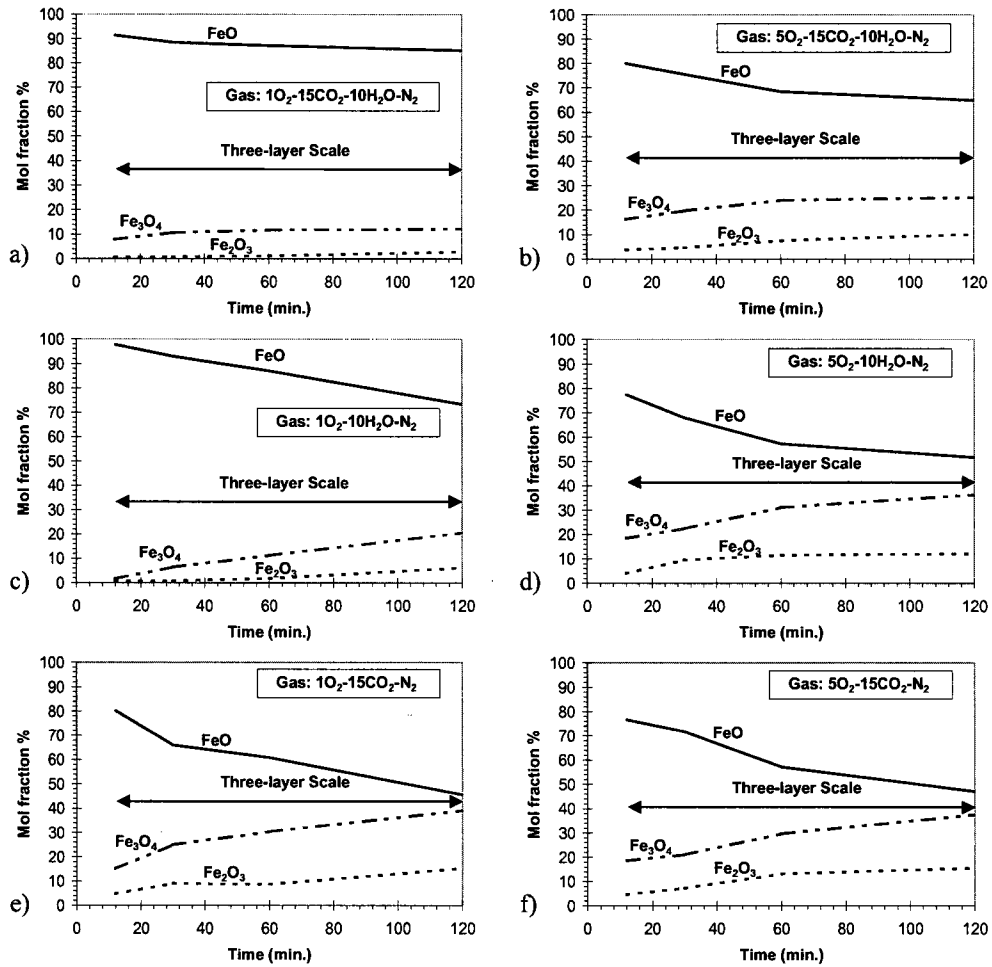


Figure 3.5 Effect of free oxygen, carbon dioxide, water vapour and oxidation time on the percentages of FeO, Fe₃O₄ and Fe₂O₃ in the scales formed on low carbon steel oxidized at 1100°C in: a) 1O₂-15CO₂-10H₂O-N₂, b) 5O₂-15CO₂-10H₂O-N₂, c) 1O₂-10H₂O-N₂, d) 5O₂-10H₂O-N₂, e) 1O₂-15CO₂-N₂, f) 5O₂-15CO₂-N₂.

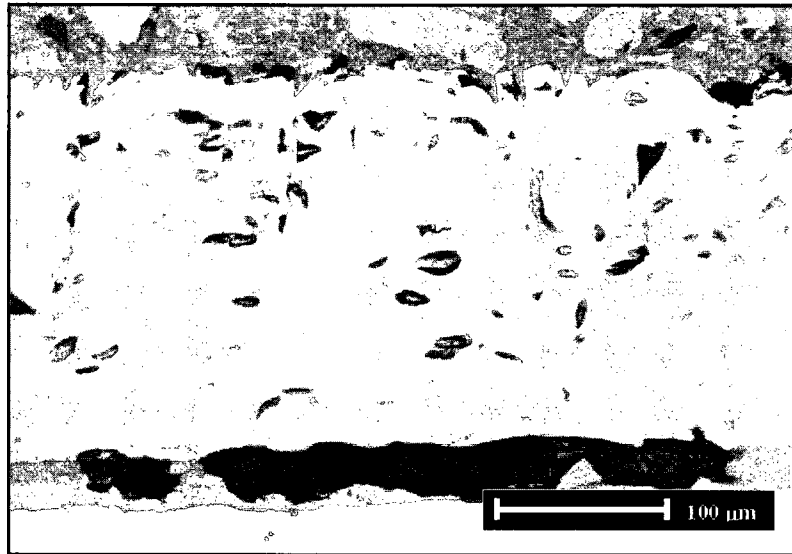


Figure 3.6 Scale formed in $1\text{O}_2\text{-}15\text{CO}_2\text{-N}_2$ at 1100°C for 60 min.

Figure 3.7 reveals the mole fraction of the iron oxides grown at 1250°C in $\text{O}_2\text{-CO}_2\text{-H}_2\text{O-N}_2$, $\text{O}_2\text{-H}_2\text{O-N}_2$ and $\text{O}_2\text{-CO}_2\text{-N}_2$ gas mixtures. Figures 3.7(a)(b) are included for comparison. They illustrate the mole fraction of the iron oxides of Fig. (3.4) for scales grown at 1250°C in low $1\text{O}_2\text{-}15\text{CO}_2\text{-}10\text{H}_2\text{O-N}_2$ and high $5\text{O}_2\text{-}15\text{CO}_2\text{-}10\text{H}_2\text{O-N}_2$ oxygen content gas mixtures, respectively. Figures 3.7(c)(d) represent the mole fractions of iron oxides at 1250°C in carbon dioxide-free atmospheres: $1\text{O}_2\text{-}10\text{H}_2\text{O-N}_2$ and $5\text{O}_2\text{-}10\text{H}_2\text{O-N}_2$ gas mixtures, respectively. The error of the phase analysis is presented in Tables (A.5)(A.7) in Appendix B. The absence of CO_2 resulted in a negligible influence on the phase composition at 1250°C (see Figures 3.7(a)(c) and Figures 3.7(b)(d)). Figures 3.7(e)(f) show the mole fraction of the iron oxides at 1250°C in water vapour-free atmospheres: $1\text{O}_2\text{-}15\text{CO}_2\text{-N}_2$ and $5\text{O}_2\text{-}15\text{CO}_2\text{-N}_2$ gas mixtures, respectively. The error of the phase analysis is in Tables (A.4)(A.6) in Appendix B. As in the case of scales grown in water vapour-free atmospheres at 1100°C , the absence of water vapour resulted in large gaps parallel to the scale/steel interface, Figure 3.8. The extended gap formation resulted in a considerable reduction in the diffusion of iron and in a low percentage of wüstite and high percentages of magnetite and hematite (see Figures 3.7(a)(e) and Figures 3.7(b)(f)).

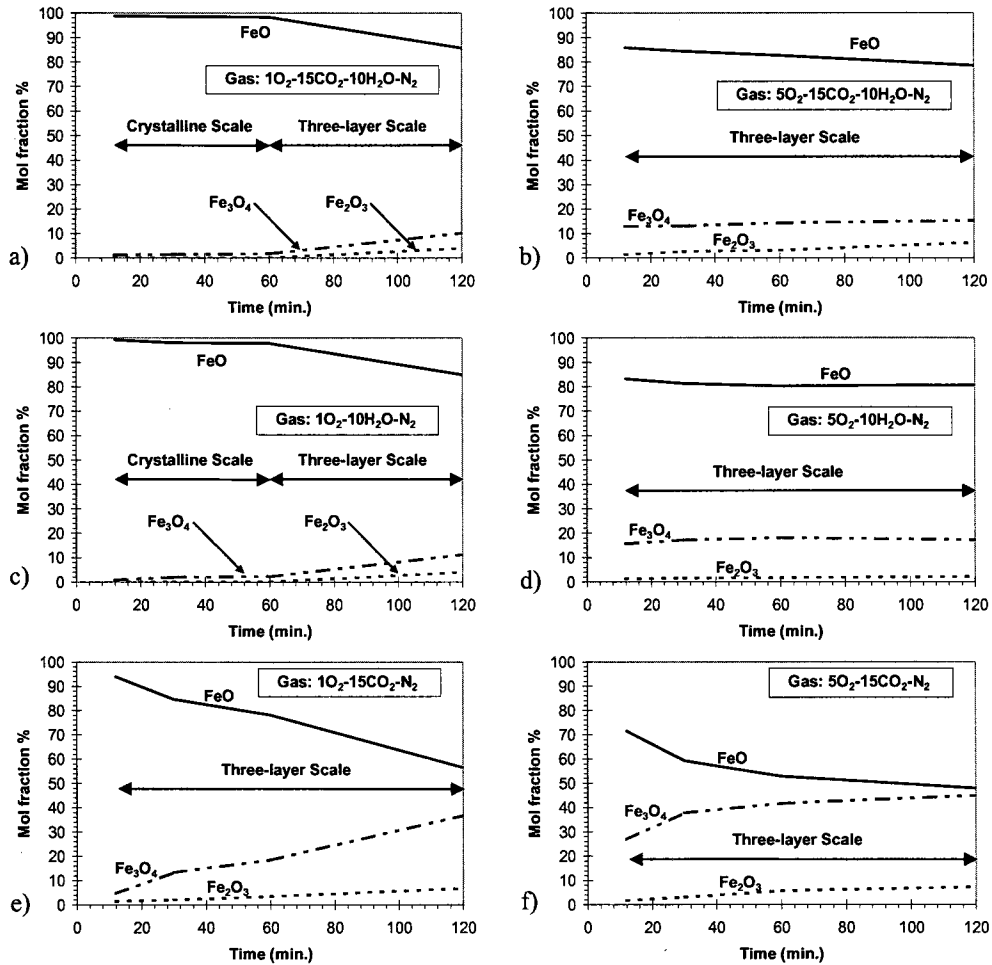


Figure 3.7 Effect of free oxygen, carbon dioxide, water vapour and oxidation time on the percentages of FeO, Fe₃O₄ and Fe₂O₃ in the scales formed on low carbon steel oxidized at 1250°C in: a) 1O₂-15CO₂-10H₂O-N₂, b) 5O₂-15CO₂-10H₂O-N₂, c) 1O₂-10H₂O-N₂, d) 5O₂-10H₂O-N₂, e) 1O₂-15CO₂-N₂, f) 5O₂-15CO₂-N₂.

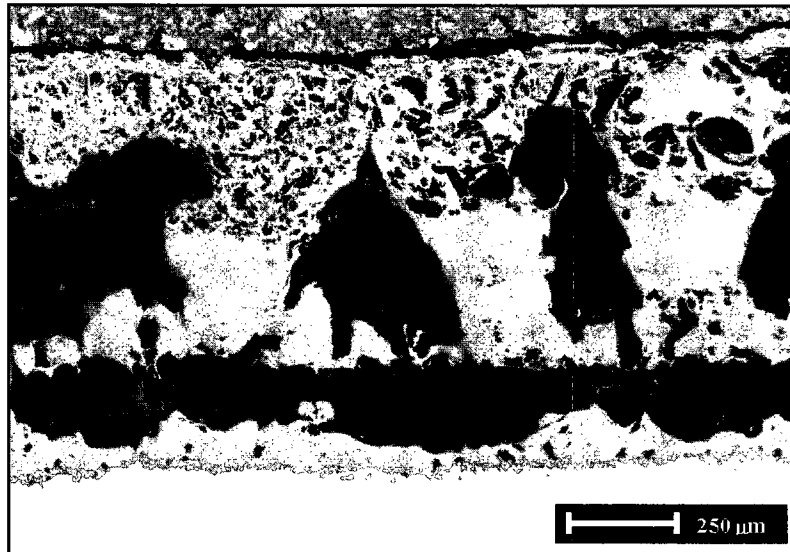


Figure 3.8 Scale formed in 1O₂-15CO₂-N₂ at 1250°C for 120 min.

3.5 Summary

The phase composition of scales grown on low carbon steel in O_2 - CO_2 - H_2O - N_2 , O_2 - H_2O - N_2 and O_2 - CO_2 - N_2 gas mixtures under conditions similar to those of reheating furnaces in hot strip mills was investigated and the results are summarized as follows:

- 1) The scales could be classified as two types: crystalline scale and classical three-layer scale. The crystalline scale with an irregular outer surface was composed mostly of wüstite (FeO) and a negligible amount of magnetite (Fe_3O_4). The classical three-layer scale was composed of wüstite (FeO), magnetite (Fe_3O_4) and hematite (Fe_2O_3).
- 2) A rise in free oxygen increased the percentages of magnetite and hematite in the scales as reported in previous studies (Preece *et al.*, 1939; Sheasby *et al.*, 1984; Abuluwefa, 1996). Furthermore, in dilute atmospheres an increase in oxidation time at a constant temperature increased the percentages of magnetite and hematite.
- 3) In water vapour-free atmospheres, the absence of water vapour formed gaps near the scale/steel interface that resulted in a reduction of the percentage of wüstite and an increase in the percentages of magnetite and hematite.
- 4) The influence of carbon dioxide on the phase composition of the scales was small at $1100^\circ C$, and negligible at $1250^\circ C$.

**Chapter
Four**

**Secondary and Tertiary Scales
in Hot Rolling**

4.1 Introduction

There has been extensive work relating temperature to scale thickness, surface quality and/or work roll wear (Blazevic, 1996; Li *et al.*, 2001; Vergne, *et al.*, 2001; Wolf, October 2000), blistering (Matsuno, 1980) and oxidizing mechanisms (Schwerdtfeger and Zhou, 2003). Therefore, in this chapter the influence of temperature and time on oxidation rate and morphology of secondary and tertiary scales is investigated in order to better understand work roll wear and surface defects in hot strip rolling.

After the first descaling, secondary and tertiary scales grow in short oxidation times in the different stages of the hot rolling process. When analyzing the phase composition of scales grown in short oxidation times, e.g. 30 seconds, “in-situ” analyses by neutron and X-ray diffraction are not suitable due to the lengthy time required for measurements. In addition, these analyses cannot be applied to low volume fractions of the oxides in the early stage of oxidation. As an alternative, quantitative X-ray diffraction phase analysis by a direct comparison method has been applied in this study.

4.2 Objectives

The objective of this chapter is to investigate scales grown in air for short oxidation times ≤ 120 s under conditions similar to those of secondary and tertiary scales in hot strip mills. The specific objective of this chapter is to investigate:

- 1 - The influence of oxidation time and temperature on the phase composition of the scale, scale thickness (oxidation rate) and porosity of scales.
- 2 - The texture and microstructure of scales in the initial stage of oxidation.

- 3 - The most beneficial conditions for hot rolling for reducing surface defects and work roll wear.

4.3 Experimental

Low carbon steel samples were obtained with the chemical composition given in Chapter 3 (Table 3.1). The (200) pole figure of the steel used for the experiments is given in Figure 4.1. For the oxidation tests, the samples were ground to a 1200 grit surface finish with SiC paper and cleaned with alcohol. The dimensions of samples for the phase composition analysis were 30 mm in width, 70 mm in length and 1 mm in thickness. The dimensions of samples for scale rate measurements and microscopic observations were 15 mm in width, 20 mm in length and 1 mm in thickness.

4.3.1 Rate of Scale Growth and Scale Thickness Measurements

The oxidation rate increases with the air velocity until a critical value of 4.2 cm/s (Abuluwefa, 1996). In this study, the air velocity of 4.2 cm/s was chosen to simulate most oxidizing conditions in air during hot rolling. The weight gained by the steel sample during oxidation was measured in an ATI Cahn thermogravimetric analyzer (Model TGA 171). This thermogravimetric analyzer consists of a tubular vertical furnace equipped with a microbalance with a sensitivity of 1 μg , Figure 4.2. For the thermogravimetric analysis, the samples were heated to the desired oxidation temperature in an argon atmosphere. Then, the argon was replaced by dry air with a velocity of 15 cm/s in order to change the atmosphere in 2 s. After this time interval, the flow of air was adjusted to obtain an air velocity of 4.2 cm/s. The samples were isothermally oxidized for 40, 80 and 120 s, over the temperature range 600-1200°C. After oxidation, a cooling rate of $-5^\circ\text{C}/\text{min}$. was used to cool the oxidized samples with a flow of argon to prevent any further oxidation. Then, the oxidized samples were hot mounted in a resin and polished with SiC paper to a 1200 grit surface finish. Colloidal

silica of 0.05 μm was used in the final stage. The scale/steel cross-sections were observed with a scanning electron microscope (Model Philips XL-30 FEG) and an optical microscope equipped with an image analyzer. The rate of oxidation was followed by measuring the scale thickness. The increase in scale thickness during the oxidation interval of 1-120 s was estimated by correlating the weight gain per unit surface area to the scale thickness measured at ten different points in the scale/steel cross-sections of the samples isothermally oxidized for 40, 80 and 120 s.

4.3.2 Phase Composition

A tubular horizontal furnace (Model Mellen Microtherm 1300°C) was used to heat the samples in argon atmosphere to 750, 800, 850, 900, 950, 1000, 1050, 1100, 1150 and 1200°C. The argon was then replaced by dry air with a velocity of 15 cm/s in order to change the atmosphere in 2 s; later the velocity was reduced to 4.2 cm/s. After isothermal oxidation of 30, 120 and 600 s, the samples were quenched in water in order to avoid the decomposition of wüstite. The volume fraction of wüstite, magnetite and hematite was determined by the experimental procedure described in Chapter 3.

4.3.3 Texture and Microstructure Analyses

Electron backscatter diffraction (EBSD) can be used to reveal the microstructure of the scales grown on steels (Burke and Higginson, 2000; Kim and Szpunar, 2001; Higginson *et al.*, 2002; Biroasca *et al.*, 2004). Nevertheless, there is a lack of information on the microstructure of scales in the initial stage of oxidation. In the finishing strip mill, the oxidation time between the finishing descaler and the first finishing stand and between stands is about ≤ 10 s and mostly over the temperature range 850-950°C. In order to approximate the formation of tertiary scales in hot rolling, the samples were isothermally oxidized in air at 850, 900 and 950°C for 10 s. The velocity of the dry air was initially 15 cm/s in order to change the atmosphere in 2 s, later the velocity was

decreased to 4.2 cm/s. After oxidation, the samples were quenched in water in order to avoid the decomposition of wüstite and stop any further oxidation. Scale/steel cross-sections were hot mounted in a conductive resin and polished with SiC paper to a 1200 grit surface finish. Colloidal silica of 0.05 μm was then used in the final stage for several hours. A scanning electron microscope (Model Philips XL-30 FEG) with a TSL orientation imaging system was used to reveal the microstructure and texture of the scales. The experimental parameters used in the EBSD analysis were: acceleration voltage 20 KeV, working distance 15 mm, spot size 5 and tilted angle of 70°.

In EBSD an electron beam generated in a scanning electron microscope (SEM) is used for microstructure analysis (Dingley *et al.*, 1995; Reimer, 1998; Brandon and Kaplan, 1999; Schwartz *et al.*, 2000; Randle and Engler, 2000). Figure 4.3 shows a diagram of the components of an EBSD system. In an SEM the incident electron beam is scattered in all directions when it strikes a crystalline solid sample, Figure 4.4. Therefore, there are always some electrons that satisfy Bragg's law (at every set of planes). Kikuchi diffraction occurs when the electrons arriving at the Bragg angle undergo elastic scattering that results in a strong reinforced beam (Randle and Engler, 2000). Since diffraction takes place in all directions, the diffracted electrons assume a cone shape (Kossel cones). The intersections of the Kossel cones with a recording medium, e.g. a phosphor screen interfaced to a camera or a piece of cut film, reproduce a Kikuchi pattern. In this pattern, each intersection of the Kossel cones with the recording medium form a pair of parallel lines (called Kikuchi lines or Kikuchi band). The position of the bands is a function of the phase and orientation of the crystal lattice (Schwartz *et al.*, 2000; Randle and Engler, 2000; Fultz and Howe, 2002). As a result, Kikuchi patterns contain all the angular relationships in a crystal (interzonal angles, interplanar angles and crystal symmetry). Fully automated processes are available to identify the bands and poles of a Kikuchi pattern in order to determine the phase and orientation of the diffracting volume from which the pattern was collected (TSL manual, 2001; Schwartz *et al.*, 2000; Randle and Engler, 2000).

In the characterization of the scales using EBSD, the information recorded in a phosphor screen was automatically processed by TSL software. This software processes

the data obtained and defines orientation by three Euler angles. In the analysis of the Kikuchi patterns, the TSL software considers only the planes that can be observed in the diffraction patterns, and all their possible combinations and symmetries. The software determines the Miller indices (indexing process) associated with the Kikuchi bands in order to calculate the orientation of the crystal lattice. Usually, more than one solution (i.e. Miller indices assigned to a set of three bands that satisfy the interplanar angles) is possible. Therefore, a voting process in which each solution is voted (counted) takes place, identifying the most probable solution. Once the best solution is identified, the Kikuchi pattern is indexed, and the orientation of the crystal is determined. A confidence index (CI) and a fit parameter (Fit) are used to evaluate the voting process (TSL manual, 2001). The CI is calculated by subtracting the votes of the second most voted solution from those of the most voted solution. Then, the difference is divided by the number of all the possible triplets (i.e. set of three bands that satisfy the interplanar angles) that can be formed from the detected Kikuchi bands. The Fit parameter represents the average angular difference between the expected position of the bands calculated with the voting process and the detected bands. The TSL software can represent the texture of the specimen by many features such as pole figure, orientation distribution function (ODF), inverse pole figure, etc. In this study, the (001) pole figure was selected to represent the texture of the scales. This pole figure shows the position of the {001} poles relative to the sample reference frame.

In addition to the orientation analysis, the TSL software has a phase indicator, which indicates the phase observed in multiphase analysis. The software selects the right phase with a ranking factor (the highest ranking value determines the phase to be selected), which is calculated as follows:

$$R_i = votes_i / votes_{max} + fit_{min} / fit_i + CI_i / CI_{max} \quad (4.1)$$

where R_i is the ranking of the candidate phase, $votes_i$ are the votes of the candidate phase, $votes_{max}$ are the maximum votes observed in a candidate phase, fit_{min} is the minimum Fit parameter observed in a candidate phase, fit_i is the Fit parameter of the

candidate phase, CI_i is the confidence index of the candidate phase and CI_{\max} is the maximum confidence index observed in a candidate phase.

In the microstructure analysis of the scales, EBSD was also used to obtain maps of the image quality parameter (IQ). The IQ describes the quality of an electron backscatter diffraction pattern (TSL manual, 2001). In EBSD, any imperfection of crystal lattice produces an inferior pattern revealing its presence. Thus, the IQ has been successfully used to describe the presence of defects, e.g. grain boundaries (Adams, 1997; Humphreys, 2001). For a deeper explanation of EBSD, the reader is referred to advanced texts, e.g. those of Schwartz *et al.* (2000), Randle and Engler (2000) and Reimer (1998).

4.3.4 Pore Formation

A few samples were heated to 900 and 950°C in an argon atmosphere. Then, the argon was replaced by dry air with a velocity of 15 cm/s to change the atmosphere in 2 s; later the velocity was adjusted to 4.2 cm/s. After isothermal oxidation of 5 and 10 s, the samples were quenched in water. Scale/steel cross-sections were prepared following the procedure described above for microstructure analysis with EBSD. The image quality parameter (IQ) was used to reveal the origin of porosity in the initial seconds of oxidation.

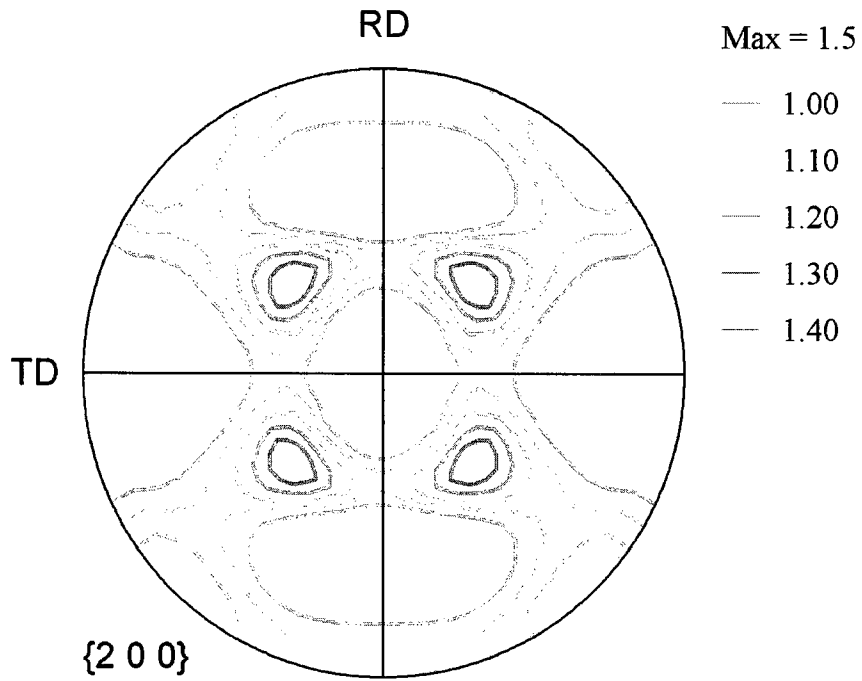


Figure 4.1 $\{200\}$ pole figure of the low carbon steel used for the oxidation tests.

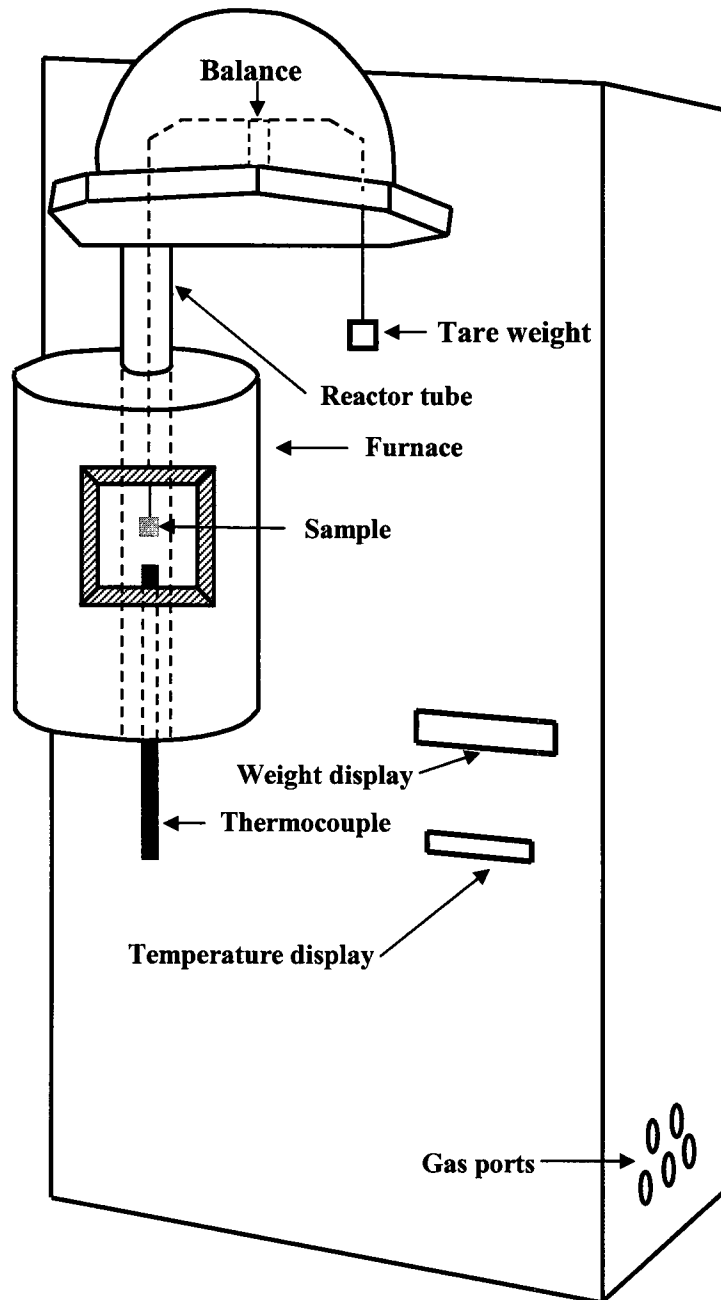


Figure 4.2 Schematic diagram of the thermogravimetric analyzer.

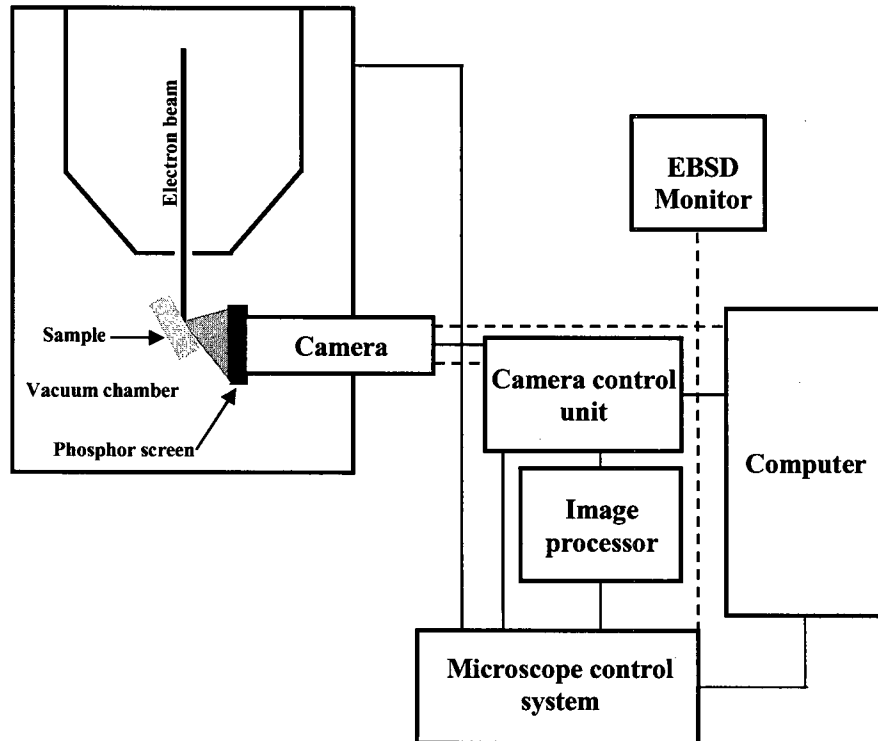


Figure 4.3 Diagram of the components of an EBSD system.

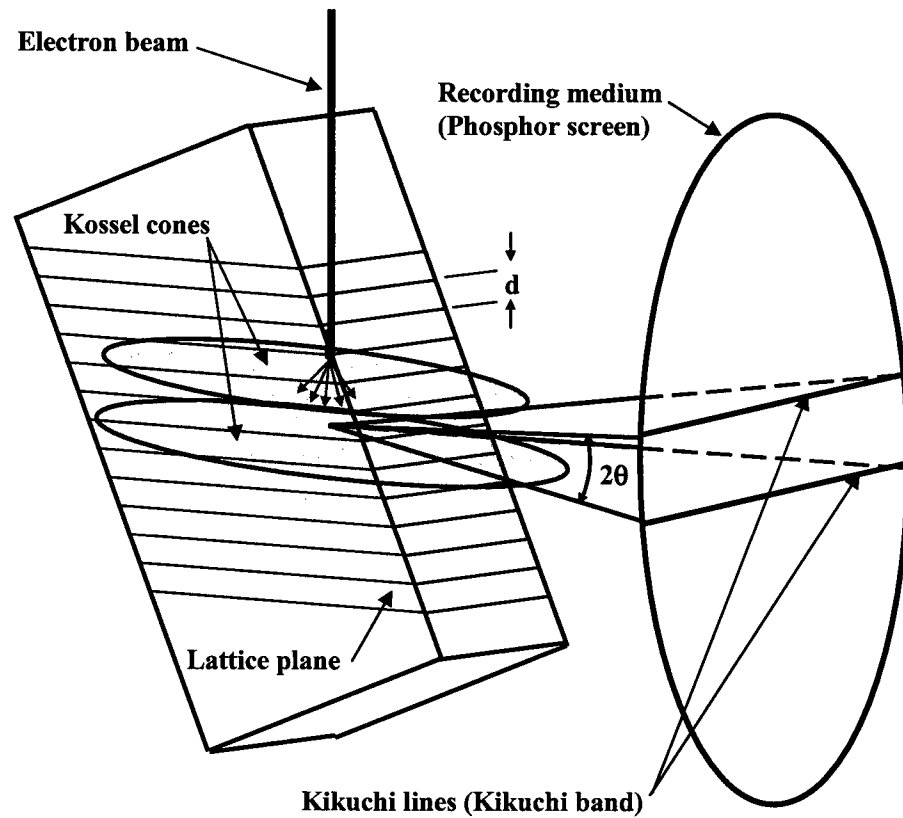


Figure 4.4 Diagram illustrating the origin of Kikuchi lines in EBSD.

4.4 Results and Discussion

4.4.1 Scale Morphology

The scale/steel cross-sections showed that in isothermal oxidation at temperatures up to 850°C, the scales have low porosity and low density of micro-cracks (homogeneous scale); above 850°C, they have medium and high porosity, macro-cracks and blisters (non-homogeneous scale), Figure 4.5. The transition from a homogeneous to a non-homogeneous scale occurred at 850°C, Figure 4.6.

The Pilling-Bedworth ratio (PBR) for iron/wüstite is 1.78 (Jones, 1996). Consequently, during oxide growth, compressive stresses are present in the wüstite layer, which is the predominant phase in the early stages of isothermal oxidation above 700°C (Basabe and Szpunar, 2004). Matsuno (1980) studied blistering during isothermal oxidation and during cooling in air. He concluded that oxidation stresses form blisters in isothermal oxidation at temperatures above 850°C. Oxidation stresses induced during oxide growth generates porosity in the oxide (Kofstad, 1985, 1988). Thus, the loss of homogeneity observed in the scales formed at temperatures above 850°C can be attributed to oxidation stresses induced during oxide growth. As the oxidation temperature was increased, the oxidation rate increased (see Figure 4.8) generating higher compressive stresses induced by oxide growth. As a result, the concentration and size of the defects increased as the oxidation temperature was increased.

In the presence of high porosity and blisters, the tensile stresses acting in the surface of the stock in the process of hot rolling can initiate crack propagation and fracturing of the oxide. This may result in an uneven oxide that can cause surface defects during hot strip rolling. The present investigation showed that high porosity and blisters are observed above 850°C, therefore, a strip surface temperature $\leq 850^\circ\text{C}$ is desirable in the hot rolling process to avoid surface defects.

4.4.2 Pore Formation

The image quality (IQ) of the scale/steel cross-sections showed that the mechanism of pore formation during the initial oxidation in air above 850°C is:

- (i) Columnar grains of wüstite grow perpendicular to the metal substrate, leaving pores at the grain boundaries, Figure 4.7(a).
- (ii) As the oxidation proceeds, oxidation stresses induced during oxide growth generate high porosity in the oxide, Figure 4.7(b).
- (iii) During further oxidation, pores are incorporated in a denser layer, Figure 4.7(c).

4.4.3 Rate of Scale Growth

Figure 4.8 shows the thickness of the scales formed in air over the temperature range 600-1200°C for 120 s. An initial linear rate of oxidation was observed at all temperatures. In the temperature range 600-1000°C, the increase in scale thickness with increasing temperature resulted in an oxidation controlled mainly by the diffusion of metal ions (parabolic rate) through an adherent compact scale with low porosity or medium porosity, Figure 4.6(a) and Figure 4.6(c) respectively; therefore, the period for the initial linear oxidation decreased with increasing temperature from 600 to 1000°C. Above 1000°C, the high oxidation rates induced high stresses during oxide growth, which in turn resulted in high porosity. This high density of pores (see Figure 4.9) allowed the air to reach the reaction surface, prolonging the period for the initial linear oxidation. Therefore, the period for the initial linear oxidation increased and was observed for longer periods of time when the temperature was increased from 1000 to 1200°C.

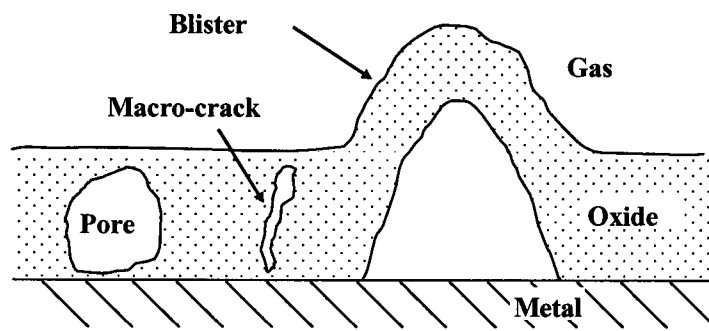


Figure 4.5 Schematic representation of scale defects in isothermal oxidation above 850°C.

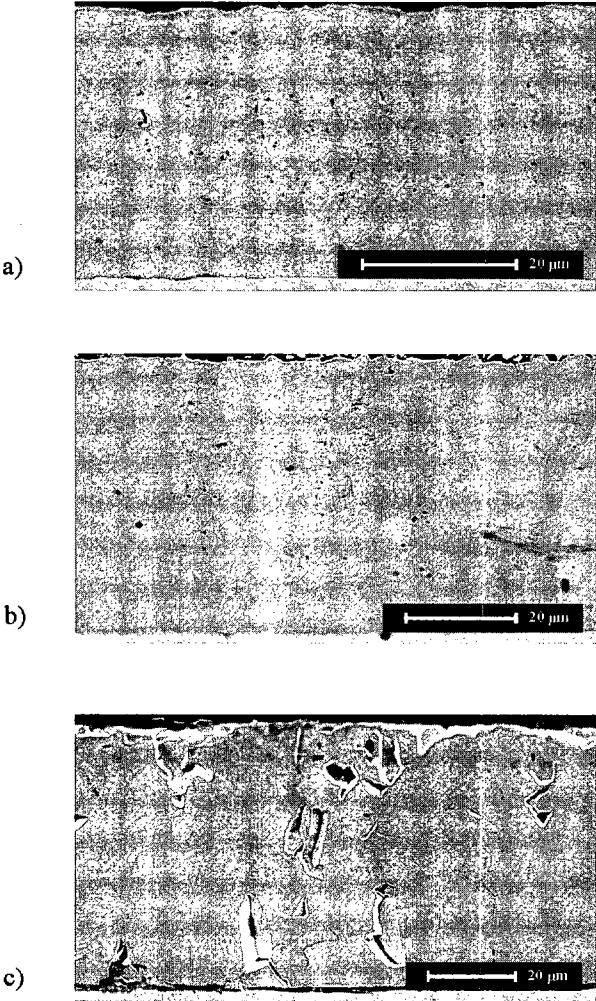


Figure 4.6 Scales formed in air for 120 s at the temperature of: a) 800°C, b) 850°C, c) 900°C.

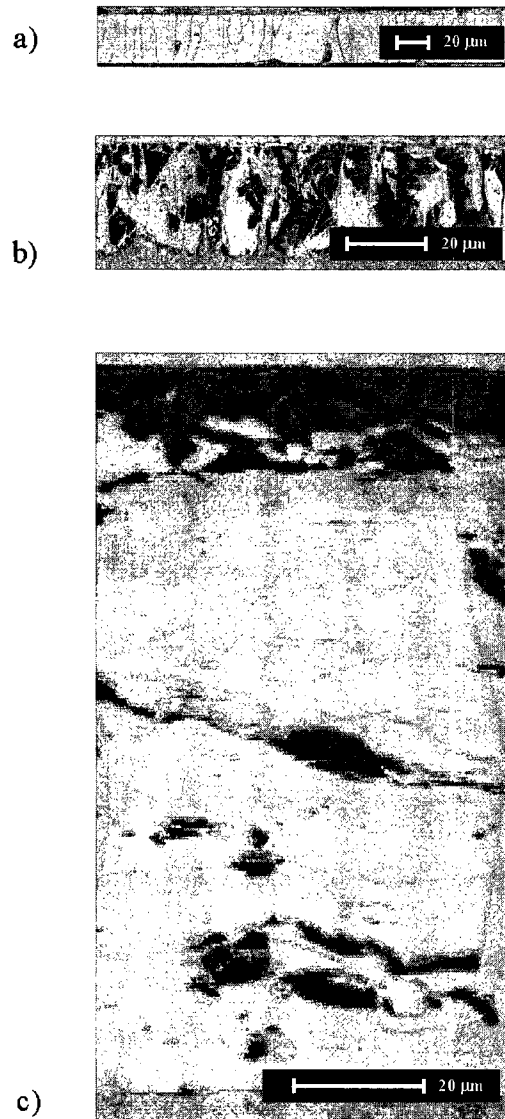


Figure 4.7 The image quality (IQ) of scales formed at 950°C in air for: a) 5 s, b) 10 s, c) 120 s.

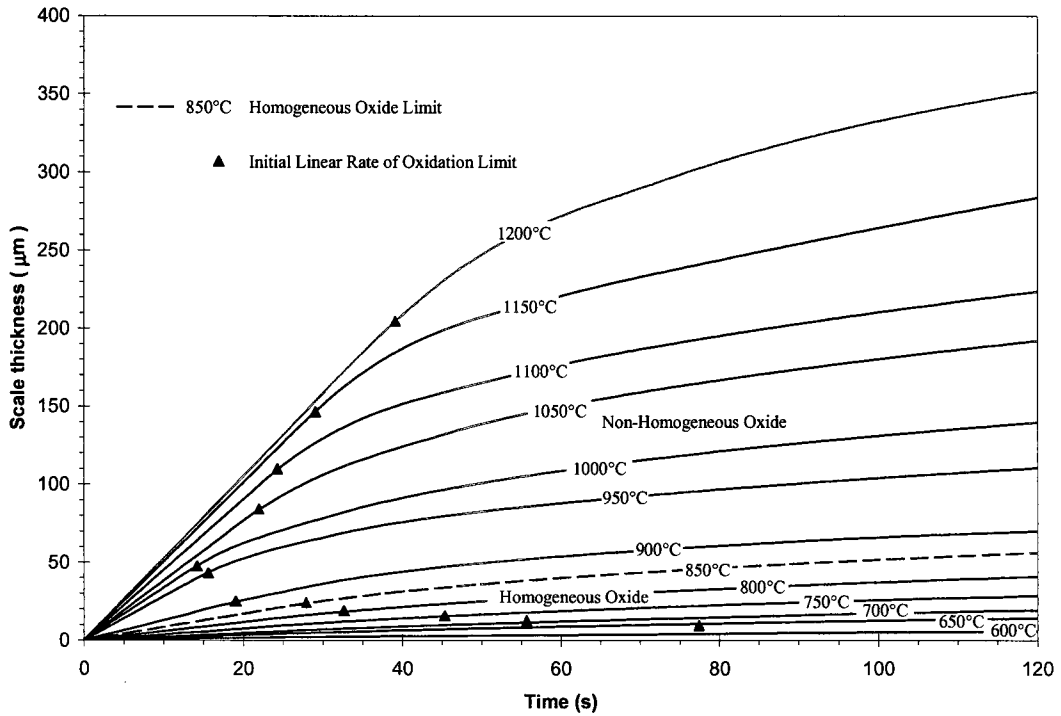


Figure 4.8 Thickness of scales formed on low carbon steel in air over the temperature range 600-1200°C for 120 s. The dashed line for the temperature of 850°C indicates the division between homogeneous oxide and non-homogeneous oxide.



Figure 4.9 Scale formed in air for 40 s at 1200°C showing high porosity.

4.4.4 Phase Composition

Figure 4.10 illustrates the evolution of the iron oxides with time after isothermal oxidation in air at 1050°C. Oxidation is a complex process in which time plays a decisive role in the phase composition of the iron oxide scales. In the early stages of isothermal oxidation in air for temperatures above 700°C, wüstite was the predominant phase on the scale. As oxidation proceeded, the percentages of magnetite and hematite increased.

Figure 4.11 shows the mole fraction of the iron oxides grown in an isothermal oxidation in air for 30, 120 and 600 s over the temperature range 750-1200°C. The error of the phase analysis is presented in Table (A.8) in Appendix B. Secondary and tertiary scales grow in the roughing and finishing mill operations in less than 100 s. Therefore, it was extremely important to determine the phase composition of the scales in less than 100 s. Figure 4.11(a) shows the mole fraction of the iron oxides for 30 s of oxidation. The percentage of wüstite was high for temperatures between 800-1200°C. The percentage of magnetite was low over the temperature range 900-1050°C. The percentage of magnetite increased for temperatures lower than 900°C and higher than 1050°C. Hematite was not detected over the temperature range 850-1050°C and 1150-1200°C. Figure 4.11(b) illustrates the mole fraction of the iron oxides for 120 s of oxidation. The percentage of wüstite was high over the temperature range 850-1000°C. Outside this range, the percentage of wüstite decreased, while percentages of magnetite and hematite increased. Hematite was not detected at temperatures between 900-1000°C. Figure 4.11(c) represents the mole fraction for 600 s of oxidation. The percentage of wüstite was high in the temperature range 900-1000°C. Outside the range, the percentage of wüstite decreased, while the percentages of magnetite and hematite increased considerably.

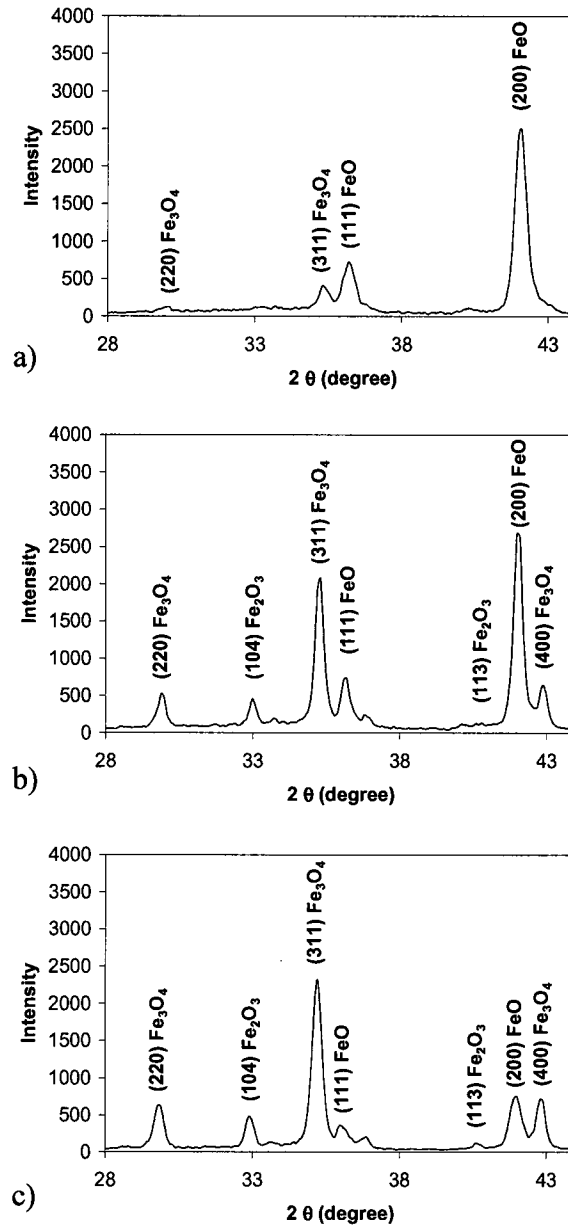


Figure 4.10 Oxide powder diffraction patterns after isothermal oxidation in air at 1050°C for: a) 30 s, b) 120 s, c) 600 s.

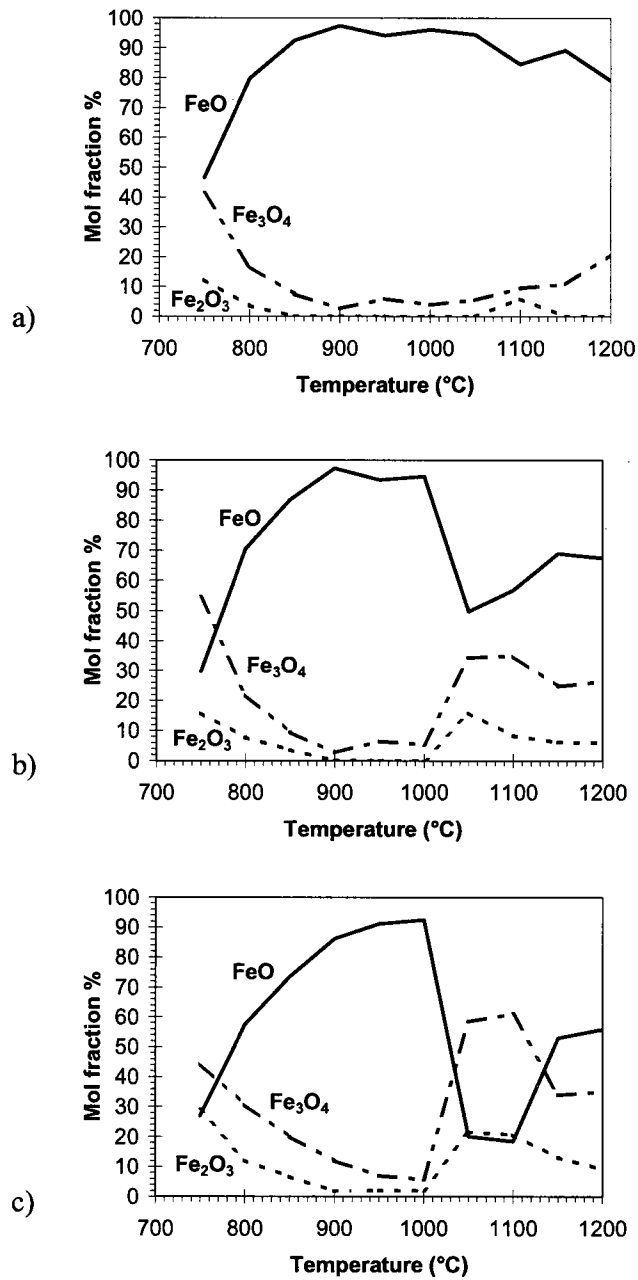


Figure 4.11 Iron oxide composition as a function of temperature and oxidation time for: a) 30 s, b) 120 s, c) 600 s.

4.4.5 Texture and Microstructure Analyses

The EBSD pattern image quality map (IQ) of the scales formed at 850, 900 and 950°C in air for 10 s is given in Figure 4.12. At all temperatures, the scales had a columnar growth. The dark areas in the oxide layer are physical defects (pores and cracks). The EBSD phase map of a scale grown for 10 s of isothermal oxidation at 950°C is shown in Figure 4.13.

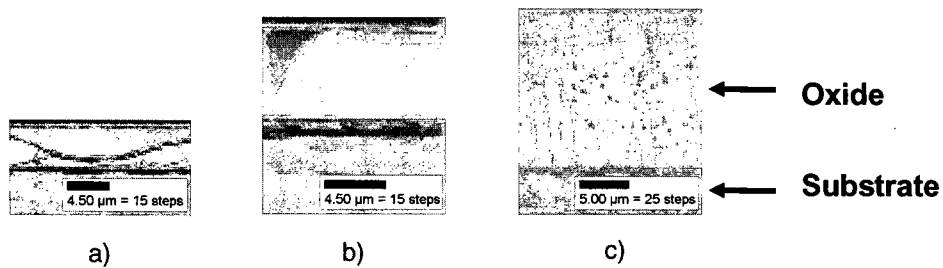


Figure 4.12 The image quality (IQ) of scales formed in air for 10 s at the temperature of: a) 850°C, b) 900°C, c) 950°C.

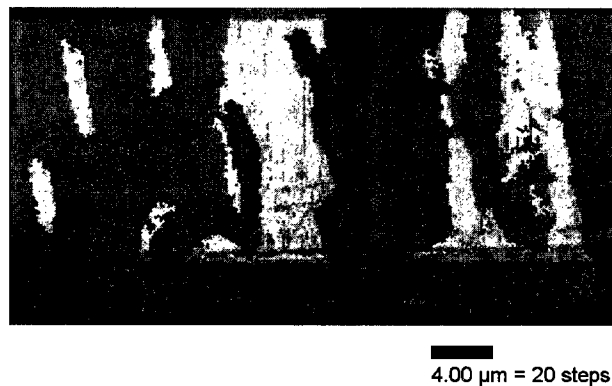


Figure 4.13 The EBSD phase map of a scale grown for 10 s at 950°C. The blue region: bcc iron; the red: wüstite; the yellow: magnetite.

Figure 4.14 shows the pole figures of the wüstite and magnetite phases formed at the temperature of 850, 900 and 950°C. At 850°C, the wüstite texture and magnetite texture were weak and had no dominant texture components. For the oxidation temperatures of 900 and 950°C, wüstite and magnetite had a cube texture $\{001\}\langle 100\rangle$.

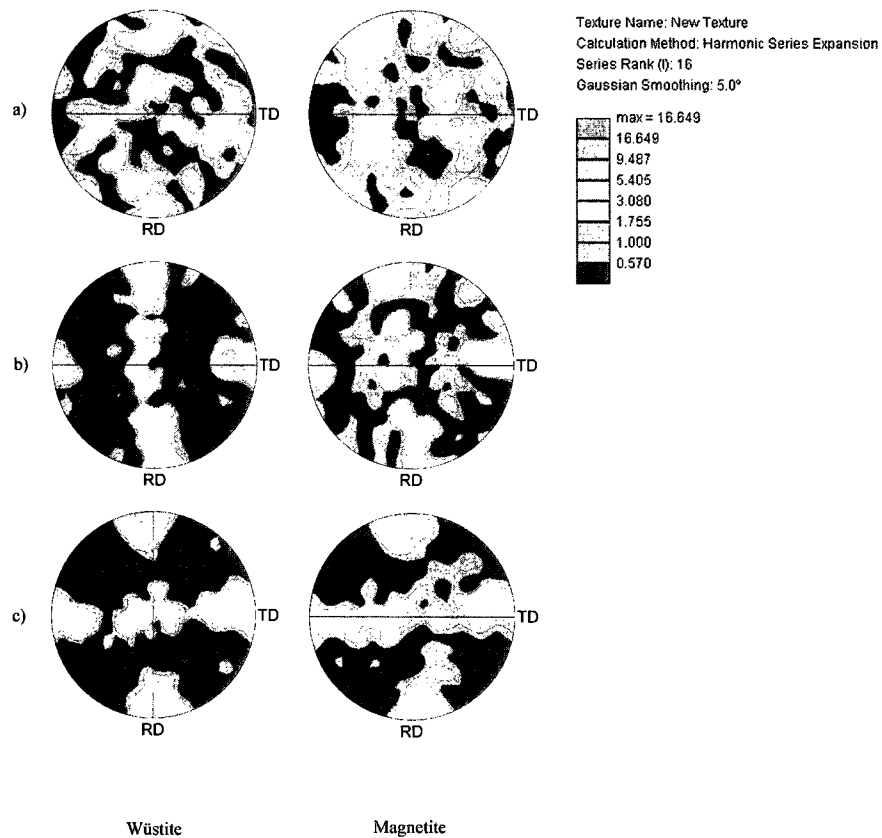


Figure 4.14 (001) pole figures of the wüstite and magnetite phases for the temperatures of: a) 850°C, b) 900°C, c) 950°C.

The experimental results are in agreement with other studies that have observed a dominant {001} texture component at high temperature in iron oxide scales (Kim and Szpunar, 2001; Higginson *et al.*, 2002; Buscail *et al.*, 1995). In addition, the present work revealed that in scales grown in an oxidation time as short as 10 s, the dominant {001} texture component observed at 900 and 950°C developed a cube texture {001}<100>. The thin oxide formed in 10 s was influenced by the texture of the steel substrate. As a result, wüstite and magnetite at 900 and 950°C grew not only with a preferred {001} texture component, but also the substrate determined the development of a preferred <001> direction parallel to the rolling direction of the substrate. Apparently the symmetry of the substrate texture determined the cube texture {001}<100> in the wüstite and magnetite phases at 900 and 950°C.

4.5 Summary

The growth rate, phase composition, texture and microstructure of scales grown on low carbon steel in air for short oxidation times ≤ 120 s were investigated. The results are summarized below:

- 1) The method of quantitative X-ray diffraction phase analysis used in this work proved to be of great value when analysing the volume fractions of wüstite, magnetite and hematite grown in oxidation times as short as 30 s.
- 2) The phase composition of the scale was influenced by the oxidation time and temperature. In the first 30 s of oxidation over the temperature range 800-1200°C, wüstite was predominant and hematite was negligible. As oxidation proceeded, the percentages of magnetite and hematite increased.
- 3) The reduction in scale thickness and increase in scale homogeneity were only achieved for temperatures ≤ 850 °C.

- 4) In the temperature range 850-950°C and for an oxidation time as short as 10 s, the oxidation temperature determined the intensity and texture of the scale. At 850°C, the scale had a weak texture with no dominant texture components. At the temperature of 900 and 950°C, wüstite and magnetite developed a cube texture $\{001\}\langle 100\rangle$.

**Chapter
Five**

Adhesion of Oxide Scales

5.1 Introduction

In the hot rolling process, scales are removed in descaling operations to prevent the formation of surface defects. Low adhesion of scales to the steel substrate facilitates the descaling process. Hence studies of scale adhesion are of great interest. In this chapter, the adhesion of scales thermally grown on low carbon steel in different oxidizing conditions is analyzed in order to better understand the adhesion of scales.

Several techniques have been developed to evaluate the adhesion of coatings to substrates and the fracture behavior of ceramic-to-metal joints. Micro hardness indentation has been used to evaluate the adhesion of cemented carbide specimens with TiC CVD coatings (Mehrotra and Quinto, 1985) and also the adhesion of thin films of ZnO on Si substrates (Marshall and Evans, 1984). The scratch adhesion test has been used in coated carbide inserts, on which TiC-Al₂O₃-TiN CVD coatings were deposited (Mehrotra and Quinto, 1985). Three-point or four-point bending tests can be used to assess the adhesion of ceramic-to-metal joints, e.g. the joint of hot-pressed silicon nitride and Zr has been successfully studied with a three-point bending test (Elsner *et al.*, 1985).

The above techniques are also applicable for assessing the adhesion of thermally grown scales to metal substrates. Atkinson and Guppy (1991) studied the adhesion of thermally grown oxides on pure nickel and nickel alloys. They used various techniques to evaluate adhesion, and concluded that the most suitable method for assessing adhesion is the four-point bending test since it avoids misalignment of the specimen.

In the four-point bending test, a starter crack at the ceramic/metal interface is introduced to obtain the fracture energy and fracture toughness of the interface, which represent a quantitative measure of the bond strength of the ceramic-to-metal interface (Elsener, 1985). However, the introduction of a started crack by mechanical means in the scale/metal interface of thermally grown scales is extremely difficult. As an alternative, practical adhesion can be used to assess the adhesion of scales. In this method, a normal tensile stress is applied perpendicular to the surface of the scale, and

the practical adhesion is quantified in terms of the normal required tensile stress to deadhere the scale. In the present work, a four-point bending test was applied to analyze the practical adhesion of scales thermally grown on low carbon steel in different oxidizing conditions.

5.2 Objectives

The objective of this chapter is to investigate:

- 1 - The adhesion of scales thermally grown under continuous heating and isothermal conditions.
- 2 - The influence of scale morphology on the adhesion of scales.
- 3 - The fracture of scales under a normal tensile stress.
- 4 - The spallation of scale.

5.3 Experimental

5.3.1 Four-Point Bending Test

Two stainless steel loading bars (9.8x9.8x40mm) and the oxidized steel sample were bonded for performing the four-point bending test as illustrated in Figure 5.1. In order to make the system reproducible, a mounting jig was designed by the present author to align and bond the two stainless steel loading bars and the oxidized steel sample, Figure 5.2. Several epoxies were tested and the best results were obtained with regular epoxy "Lepage". This epoxy created a strong bond between the surface of the stainless steel loading bars and the oxidized surfaces of the steel sample.

The four-point bending jig had two upper cylindrical load points 20 mm apart and two lower cylindrical load points 37.5 mm apart, Figure 5.3. A crosshead speed of 0.5 mm min^{-1} was used in a Tinius Olsen tensile tester (Model H25K-S) to deadhere the scales in the four-point bending jig, Figure 5.4. The load required to deadhere the scale was taken from the recording of the load-cross head displacement behavior, and the corresponding tensile stress was obtained with the expression given by Atkinson and Guppy (1991):

$$\sigma = \frac{3}{2} F \left(\frac{l_o - l_i}{bd^2} \right) \quad (5.1)$$

where l_o is the distance between outer load points (37.5 mm), l_i is the distance between inner load points (20 mm), b is the width of the bar (9.8 mm), d is the depth of the bar (9.8 mm) and F is the applied load to deadhere the scale.

5.3.2 Sample Preparation

The samples (9.8x9.8x5mm) were obtained from low carbon steel with the chemical composition given in Table 5.1. A tubular horizontal furnace (Model Mellen Microtherm 1300°C) was used to anneal and oxidize the samples. The annealing of the samples was carried out in an argon atmosphere at 950°C for 30 min. After annealing, the samples were polished with SiC paper to a 1200 grit surface finish and cleaned with alcohol for the oxidation test. In order to oxidize both sides of the sample, a hole of 1 mm in diameter was drilled to pin the sample in a boron nitride sample holder (see Figure 5.5). The experiments were divided into two groups. In the first set of experiments, the samples were oxidized in air under a continuous heating schedule from room temperature to 800, 880, 950 and 1200°C, Figure 5.6. In the second set of experiments, the samples were heated to the desired oxidation temperature in an argon atmosphere. Then, the argon was replaced with air by opening both sides of the horizontal tube furnace. The samples were isothermally oxidized at 700, 800 and 950°C

for 4320, 150 and 10 min. respectively (see Figure 5.7) in order to obtain scales of 130 μm in thickness. In order to diminish the decomposition of wüstite when cooling to room temperature, the samples were rapidly extracted from the furnace and placed in a chamber with an argon atmosphere. This rapid cooling method impeded any further oxidation and partially prevented the decomposition of wüstite.

After cooling, the samples were bonded to the stainless steel loading bars in the mounting jig for 24 hours. In each experimental condition, eight samples were oxidized at the same time to obtain the mean value of the load required to deadhere the scales in the four-point bending test. Microscopic examinations of the scales before and after the four-point bending test were carried out with a scanning electron microscope (SEM) model XL-30 FEG from Philips with TSL electron backscatter diffraction (EBSD) orientation imaging system. An optical microscope equipped with an image analyzer was also used to observe the fractures and morphologies of the scales. The scale/steel cross-sections for the microscopic examination were hot mounted in a resin and polished with SiC paper down to a 1200 grit and colloidal silica of 0.05 μm .

Table 5.1 *Chemical composition of the steel (wt %).*

C	Mn	Si	Cu	P	S	Ni	Mo	V	Sn	Cr
0.069	1.266	0.048	0.02	0.009	0.004	0.009	0.006	0.003	0.004	0.025

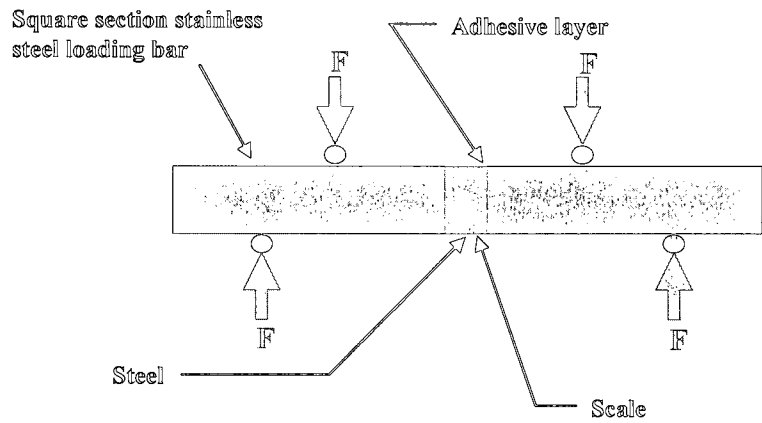


Figure 5.1 Schematic representation of the four-point bending arrangement.

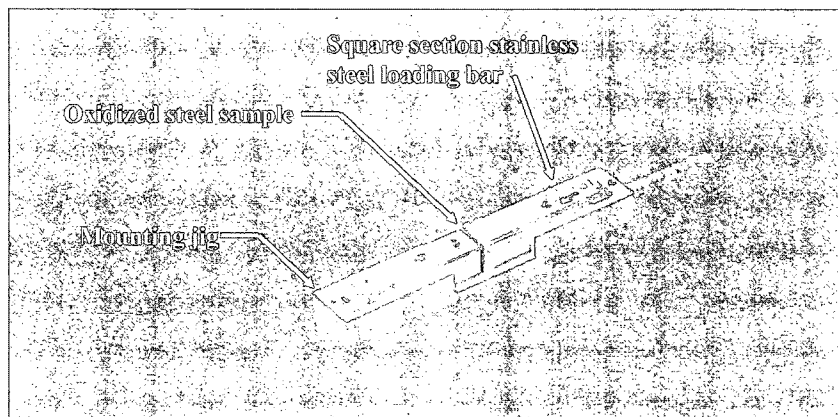


Figure 5.2 Mounting jig used to align the oxidized steel sample and stainless steel loading bars.

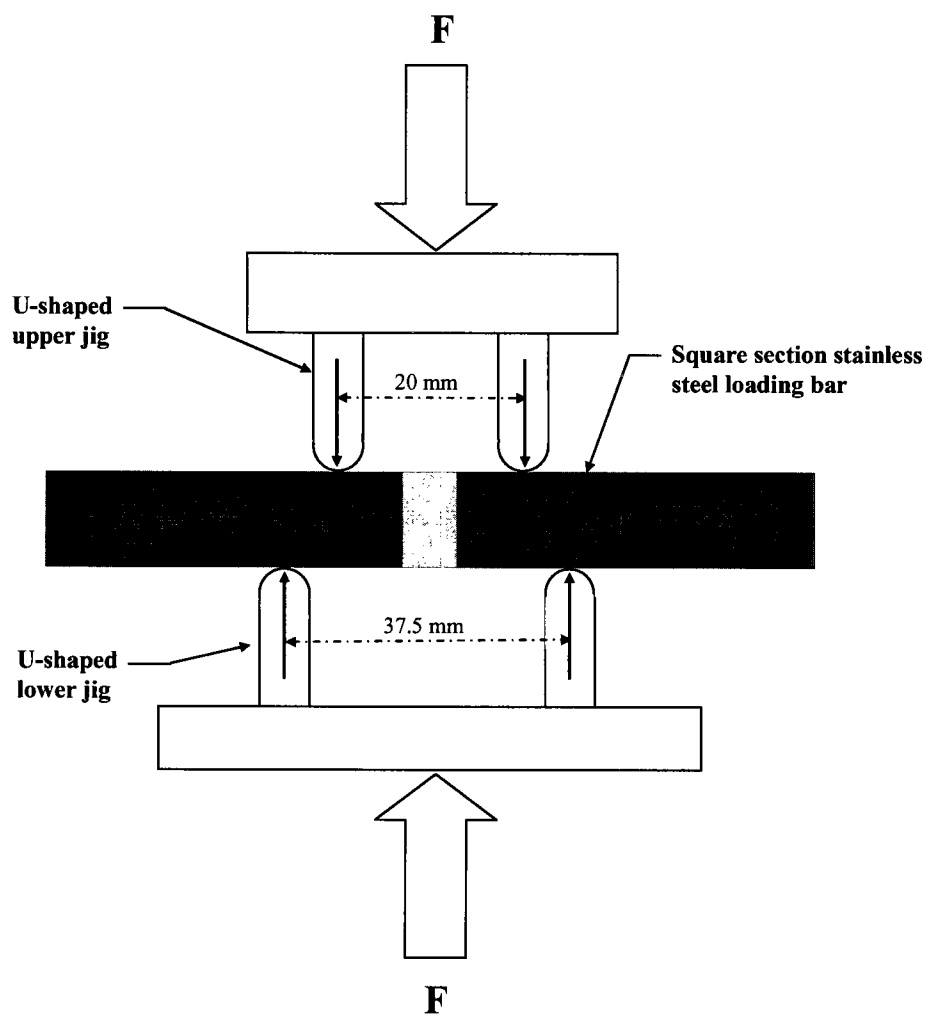


Figure 5.3 Schematic representation of the four-point bending jig.

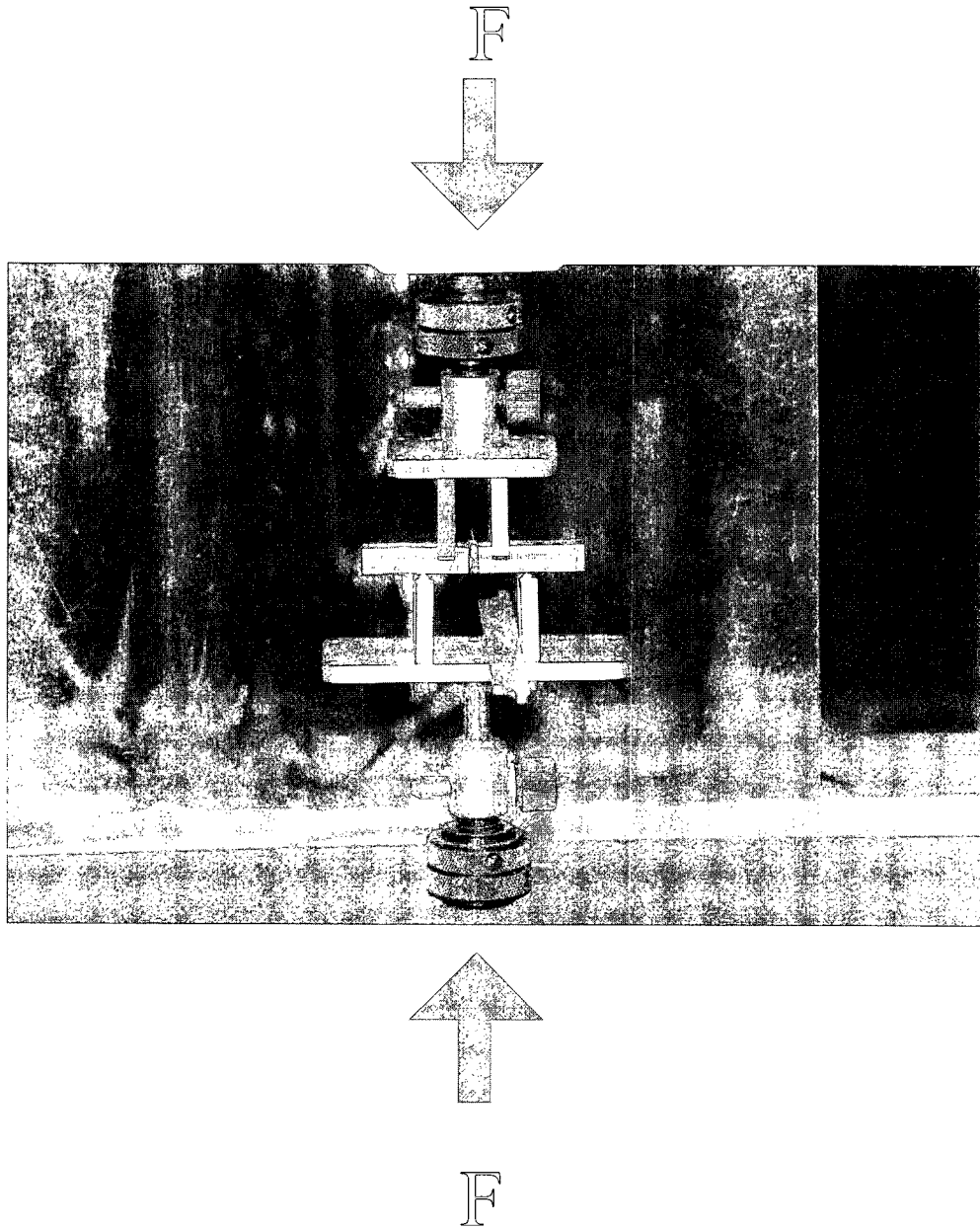


Figure 5.4 Four-point bending test.

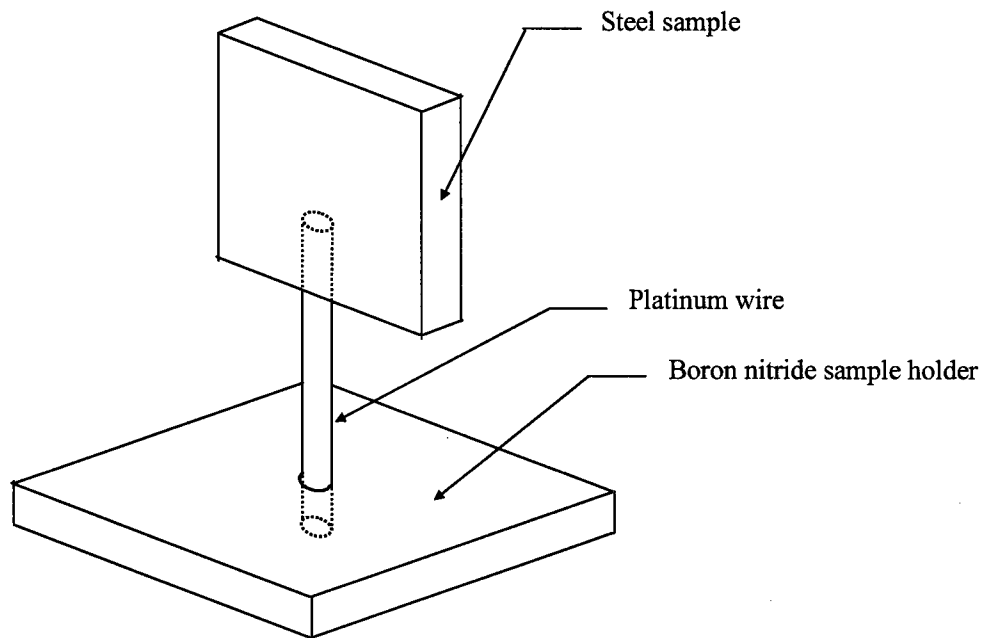


Figure 5.5 Schematic representation of the sample holder used to mount the steel samples for oxidation experiments.

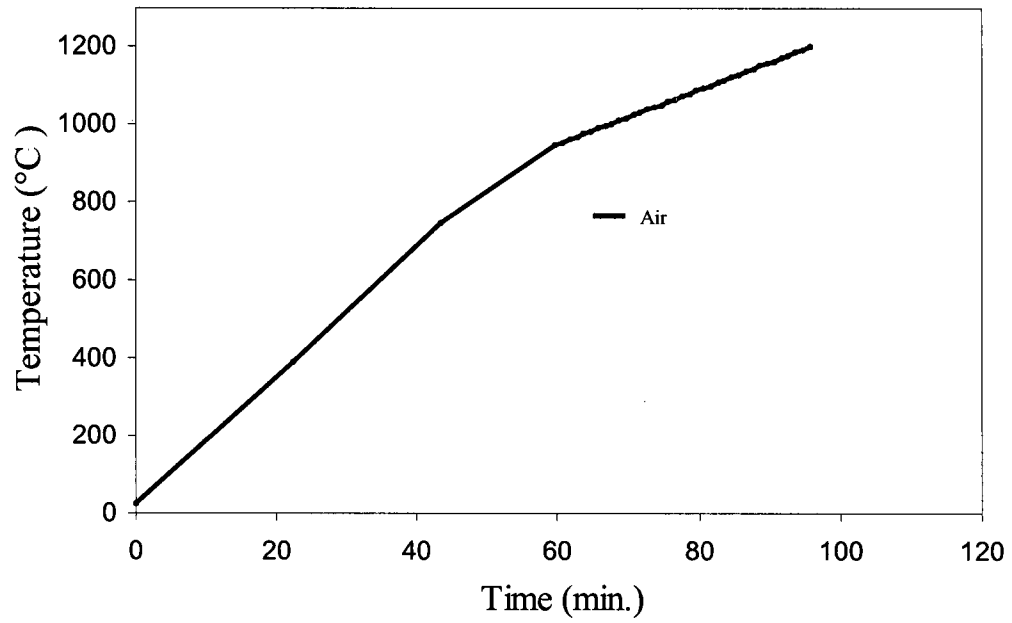


Figure 5.6 Continuous heating schedule adopted for oxidizing the steel samples.

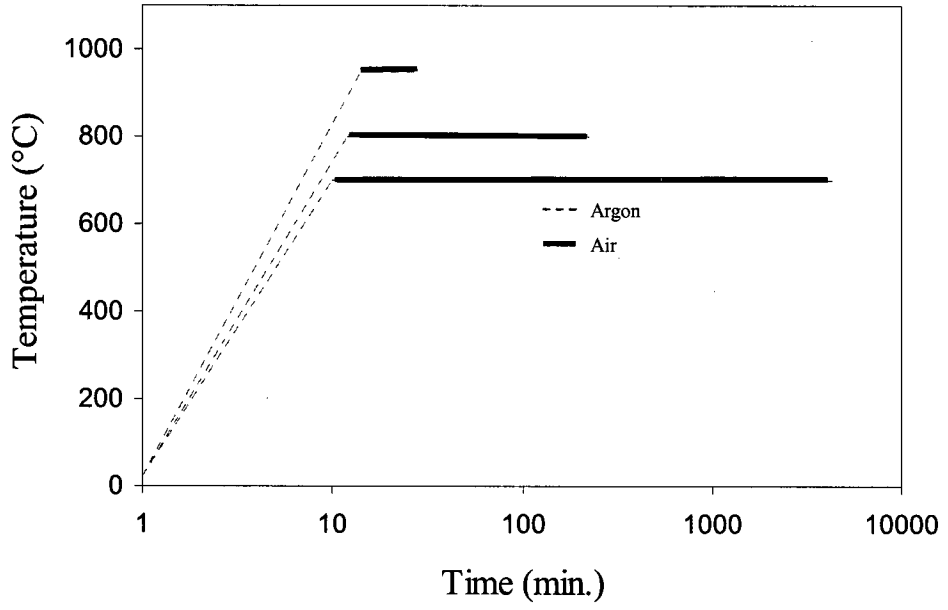


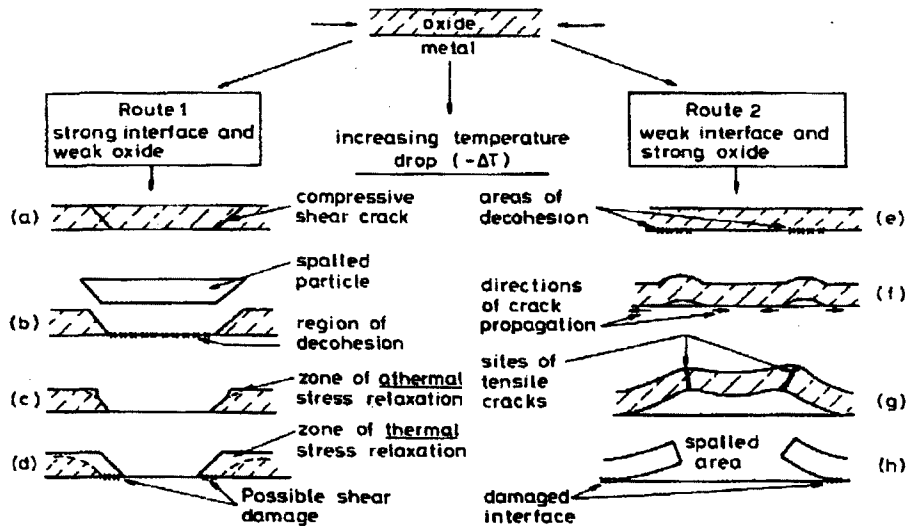
Figure 5.7 Isothermal experiments at 700, 800 and 950°C.

5.4 Results and Discussion

5.4.1 Continuous Heating Experiments

Oxide spallation occurs when the elastic energy stored in the scale is higher than the fracture energy G_C (the energy required to enlarge a crack) of the interface (Evans, 1948). A drop in temperature generates stresses in the scale due to the different thermal expansion coefficient of the oxide and metal substrate. This stress, arising from temperature change may result in spallation if the elastic energy stored is higher than the fracture energy. Two routes of spallation have been identified for scales under compressive stresses (Evans and Lobb, 1984; Evans, 1988) (see Figure 5.8). Route 1 is the “strong interface and weak oxide,” and route 2 is the “weak interface and strong oxide.” In route 1, it is assumed that the oxide is weak and fails under the compressive stress; posterior decohesion and compressive stress result in spallation. In route 2, as the oxide is in compression, decohesion occurs at the scale/metal interface; subsequent buckling and compressive stress result in spallation.

In the spallation process, the delamination (decohesion) can occur at the scale/steel interface or parallel to it in the oxide. Frequently, scale/metal interfaces are as strong as the bulk oxide, and failure takes place within the bulk oxide rather than at the interface (Stott, 1988). In the present work, the compressive stress induced during cooling from 800°C to room temperature resulted in spallation; the delamination crack was localized in the oxide parallel to the scale/steel interface. Furthermore, it was observed that the compressive stress generated shear cracks through the oxide thickness according to route 1 (strong interface and weak oxide) (see Figure 5.9). The location of the plane of decohesion in the oxide suggests that the fracture strength of the scale/steel interface was higher than the fracture strength of the scale. As a result of spallation, the four-point bending test was not used in the samples cooled from 800°C.



Route 1: (a) shear cracks develop throughout the oxide layer; (b) decohesion between cracked regions; (c) local athermal stress relaxation; (d) thermal stress relaxation.

Route 2: (e) and (f) localized decohesion can lead to buckling; (f) buckles can coalesce leading to film fracture; (g) coalesced buckle fractures; (h) release of spalled particle.

Figure 5.8 Schematic of cracking and spallation caused by compressive oxide stress (Evans and Lobb, 1984; Evans, 1988).

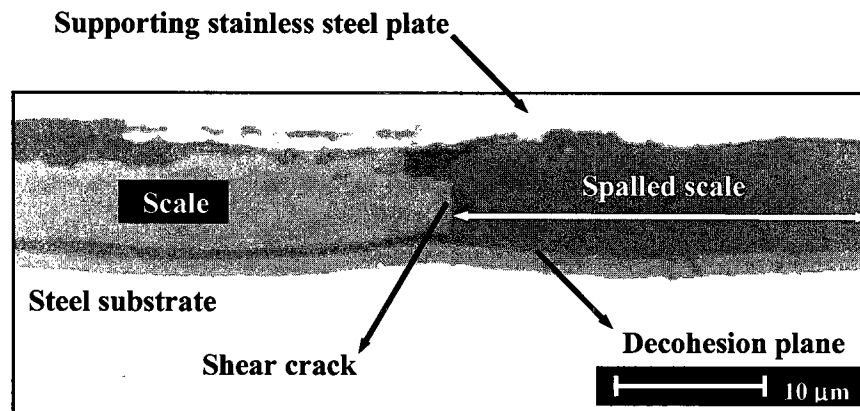


Figure 5.9 Spallation of scale during cooling from 800°C. The decohesion plane (crack) was localized in the scale. The shear crack through the scale thickness reveals that spallation occurred according to route 1 (strong interface and weak oxide). The scale was formed in air during continuous heating to 800°C.

The load-displacement in the four-point bending test was linear, Figure 5.10. This indicates that scales in the four-point bending test failed by brittle fracture. In this situation, linear elastic fracture mechanics (LEFM) can be applied. Irwin (1957) determined that in linear elastic fracture mechanics, a crack can experience three kinematically independent motions of the upper and lower surfaces of the crack: mode I loading is normal to the crack plane, in mode II the load is in-plane shear and mode III characterized by out-of-plane shear loading (see Figure 5.11).

The stress intensity factor K is used in LEFM to predict the stress state (stress intensity) near the tip of a crack caused by a remote load or residual stresses. The stress intensity factor K depends on the geometry of the crack body, on its size and on the mode and magnitude of loading (Miannay, 1998). In mode I, the stress intensity factor K_I can be obtained by the following expression (Schütze, 1997):

$$K_I = \sigma_{ox} \sqrt{\pi c} f \quad (5.2)$$

where c is the half length of the crack-line defect within the scale or the total length of a surface defect, σ_{ox} is the stress in the oxide and f is the factor reflecting the influence of the defect geometry ($f \approx 1$).

In mode I, the minimum value of K_I necessary to propagate the crack is called the critical fracture toughness K_{Ic} . If the defect size, the critical strain for crack formation ε_c and the elastic modulus of the oxide E_{ox} are known, the critical fracture toughness K_{Ic} of the oxide can be experimentally determined by the expression (Schütze, 1997):

$$K_{Ic} = f \varepsilon_c E_{ox} \sqrt{\pi c} \quad (5.3)$$

In linear elastic fracture mechanics, the stress intensity factor K_I and critical fracture toughness K_{Ic} are used to predict the beginning of crack growth. A crack will propagate only when the stress intensity factor K_I reaches or exceeds the value of the critical fracture toughness K_{Ic} :

$$K_I \geq K_{Ic} \quad (5.4)$$

In the four-point bending test, the scales were not completely removed; in some small areas the scales remained attached on the steel substrate. In the areas where the scale was removed, the separation of the scale always took place at the wüstite layer close to the scale/steel interface. Figure 5.12 shows a typical scale after debonding in the four-point bending test; the scale was formed in air during continuous heating to 950°C. The separation at the wüstite layer indicates that the fracture strength of the scale was lower than the fracture strength of the scale/steel interface.

Scales always have physical defects such as pores and micro-cracks (Schütze, 1997). The defects in scales may act as stress concentrators that initiate and propagate cracks (Stott, 1988). In the present experiments under a continuous heating schedule, the increasing temperature and time resulted in larger pores, Figure 5.13. The stress intensity factor K_I increases as the size of the defects in the scale is increased (see Equation 5.2). Thus, a direct consequence of the increase in pore size with increasing temperature and time in the continuous heating schedule was a reduction in the value of the load required to deadhere the scales, Figure 5.15.

Fracture in oxides can occur along cleavage planes (transgranular cleavage fracture) or along grain boundaries (brittle intergranular fracture). Gandhi and Ashby (1979) identified the following fracture mechanism in oxides (see Figure 5.14):

- Cleavage 1 and brittle intergranular fracture 1 (called BIF 1 in the map). In this regime, a crack or flow in the oxide allows crack propagation at a lower stress

than that required for slip; therefore, no plasticity is present in the oxide before fracture.

- Cleavage 2 and brittle intergranular fracture 2 (called BIF 2 in the map). The initial cracks or flaws are small or absent in the oxide, allowing the stress to be raised before fracture. In this situation, the stress necessary for slip or twinning is reached. The slip or twinning generates internal stress, which can nucleate and propagate cracks. This regime has a brittle fracture in which some microplasticity is present.
- Cleavage 3 and brittle intergranular fracture 3 (called BIF 3 in the map). The rise in temperature results in a fall in the flow stress and in general plasticity before failure. In this regime, the general plasticity or grain boundary sliding nucleate cracks or propagates pre-existing cracks.
- Intergranular creep fracture. Failure occurs at high temperature and low stress. Voids and wedge cracks nucleate and grow on grain or phase boundaries. This concentration of voids and cracks results in a low ductility fracture (brittle fracture) in the oxide under creep conditions.

The fracture analysis for the four-point bending test is presented in Table 5.2. Only the minimum and maximum loads required to detach a scale are included in the table since they represent all the other parameters relevant to the process of identifying the fracture mechanism. The fracture map of Gandhi and Ashby indicated that the dominant fracture mechanism in the four-point bending test was Cleavage 1 (see Figure 5.14). Furthermore, the image quality (IQ) of the scale/steel cross-sections also indicated that the fracture occurred by cleavage. Figure 5.12 shows the image quality of a typical crack after the four-point bending test of a scale formed in air during continuous heating to 950°C; the crack propagated across the grains (cleavage fracture).

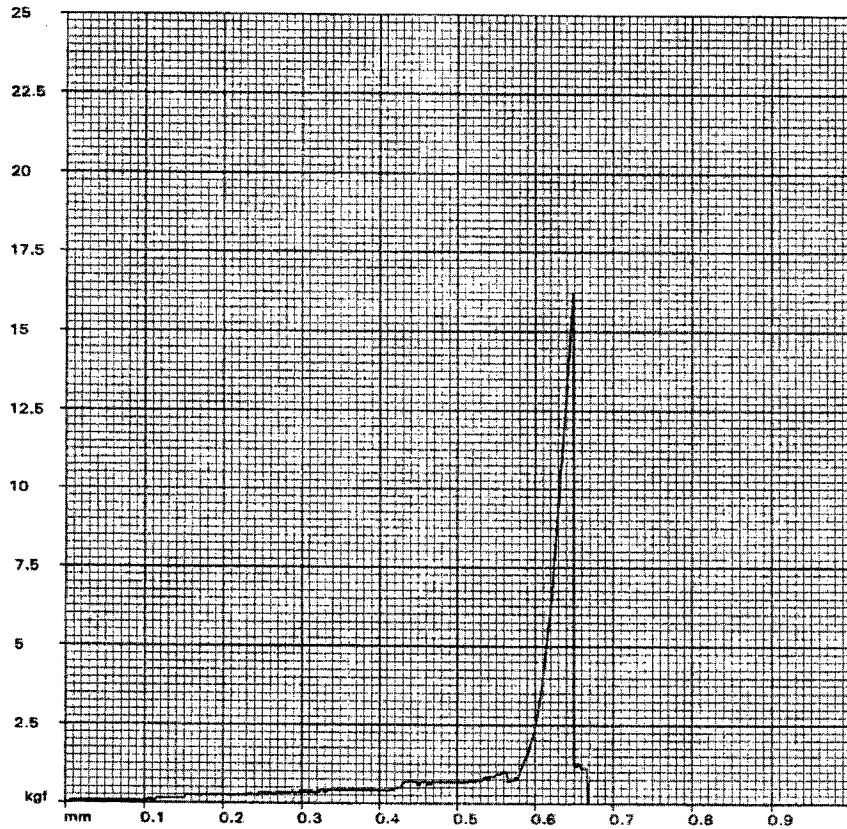


Figure 5.10 Linear load-displacement behavior in the four-point bending test. The scale was formed in air during continuous heating to 880°C.

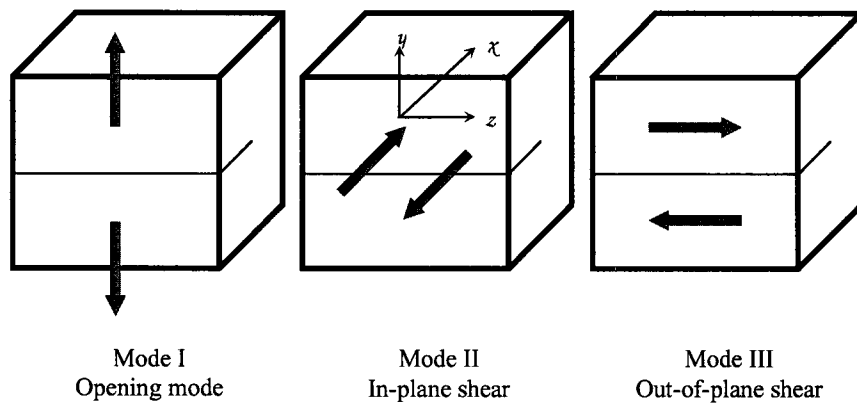


Figure 5.11 The three modes of loading in a crack.

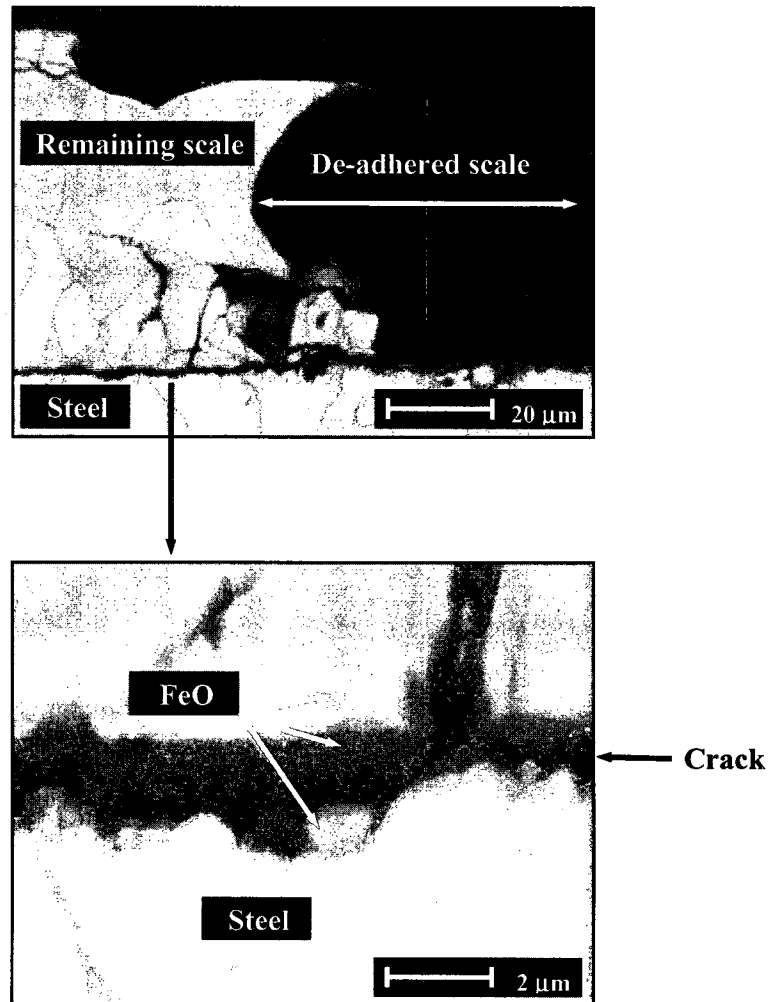


Figure 5.12 The image quality (IQ) of a scale after debonding in the four-point bending test. Some scale remained on the steel after debonding. The crack detached the scale close to the scale/steel interface. After detaching the scale, the crack propagated into the remaining scale showing the exact position of the plane of decohesion (crack), which is located in the wüstite grains (cleavage fracture). The scale was formed in air during continuous heating to 950°C.

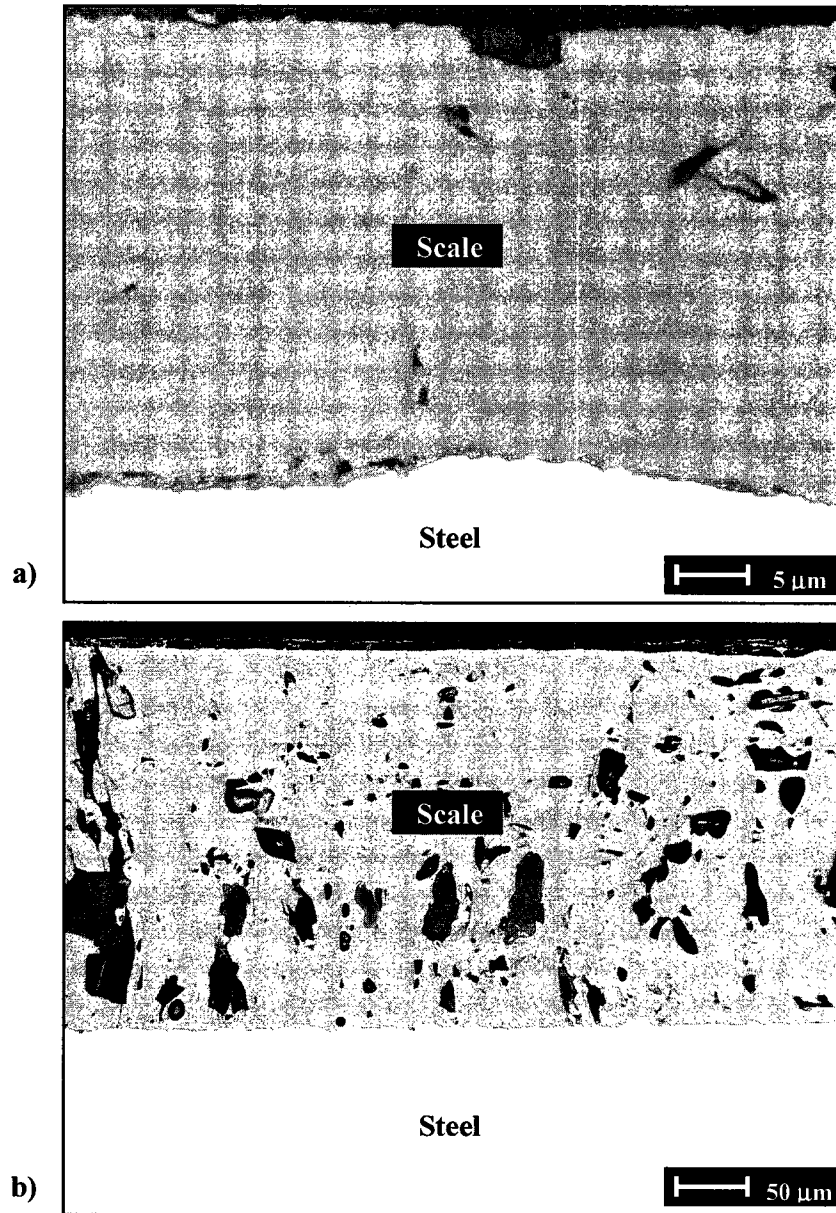


Figure 5.13 Scales formed in air during continuous heating to: a) 880°C, b) 1200°C. The increase in time and temperature in the continuous heating schedule resulted in an increase in the size and concentration of pores.

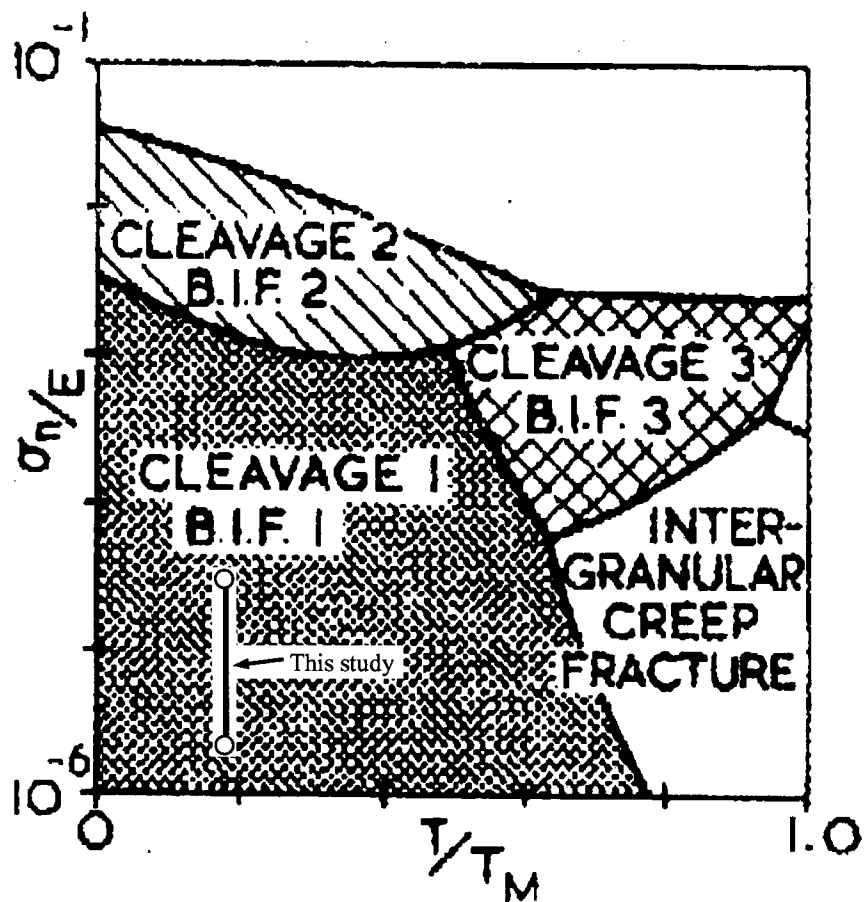


Figure 5.14 Fracture map for oxides (Gandhi and Ashby, 1979). The interval in which the fractures occurred in the present study is indicated.

Table 5.2 Fracture mechanism analysis in the four-point bending test.

Load	F (Kgf)	σ_n^* (GPA)	E^{**} (GPA)	σ_n/E	T_M^{**} (K)	T^{***} (K)	T/T_M	FM
Minimum load	1.444	39×10^{-5}	130	3×10^{-6}	1647	300	0.18	Cleavage 1
Maximum load	23.028	629×10^{-5}	130	4.84×10^{-5}	1647	300	0.18	Cleavage 1

F = force required to deadhere the scale; σ_n = Nominal tensile stress obtained from Equation 5.1; E = Elastic moduli of FeO (Robertson and Manning, 1990); T_M = melting point of FeO (The Oxide Handbook, 1982); T = room temperature; FM = fracture mechanism obtained from the fracture map for oxides of Gandhi and Ashby (1979).

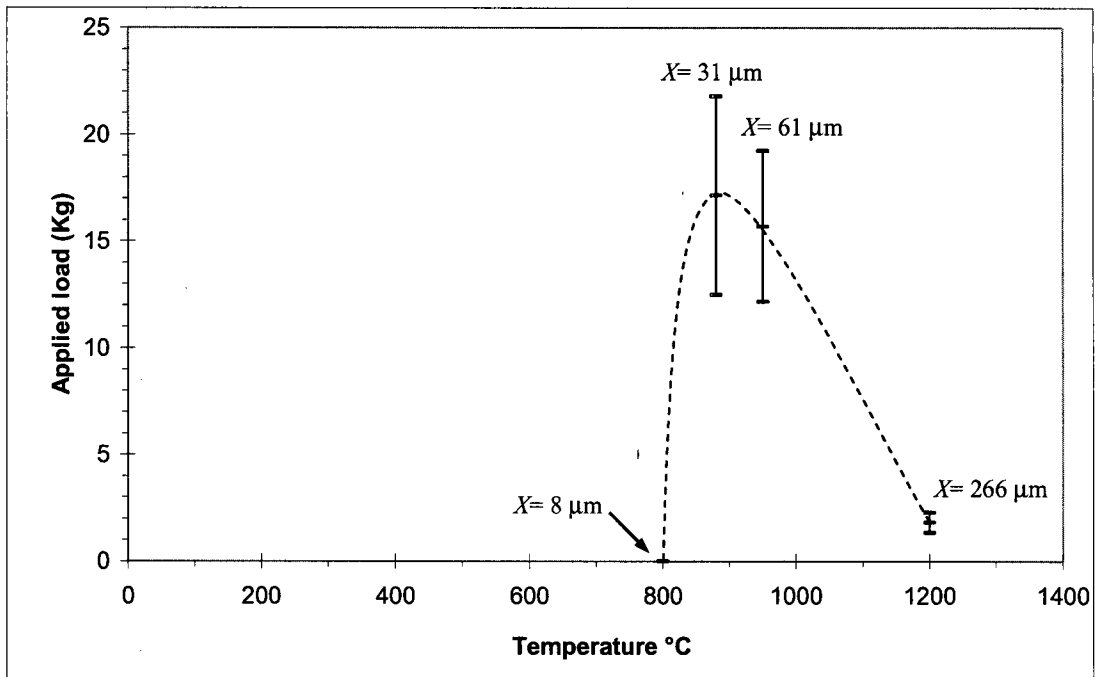


Figure 5.15 Critical load required to deadhere scales in the four-point bending test at room temperature. The scales were grown in air under a continuous heating to 800, 880, 950 and 1200°C. A zero value was assigned to the scales that spalled when cooling from the temperature of 800°C. The mean scale thickness, X , is indicated beside each data point.

5.4.2 Isothermal Experiments

The scales formed at 700°C had large pores close to the scale/steel interface, Figure 5.16. As mentioned earlier, an increase in the defect size (see Equation 5.2) increases the stress intensity factor, K_I , which in turn decreases the stress (load) required to propagate a crack. Thus, the load required to deadhere the scales formed at 700°C was low \cong 3.7 Kg (see Figure 5.17).

The compressive stress induced during cooling from the temperature of 800°C resulted in spallation of the scale. The spallation observed in the isothermal experiments was similar to the one observed in the continuous heating experiments when spallation followed route 1, and the plane of decohesion was located in the oxide, Figure 5.18.

Several researchers have observed blistering of scales during isothermal oxidation in air of steels (Griffiths, 1934), rimmed steel and iron (Matsuno, 1980), Bisra iron (Tylecote, 1960) and steels with various C content (Modin, 1962; Griffiths, 1934). During oxide growth, the change in volume as the metal is converted into oxide results in compressive stress that may form blisters if the critical value necessary to lift the scale is reached (Matsuno, 1980). In the isothermal oxidation of low carbon steel at 950°C, the compressive stress arising from oxide growth reached the critical value needed to lift the scale; therefore, scales with blisters were formed at 950°C. The blistered scale had low adhesion and was partially detached during sample handling, Figure 5.19. This is in agreement with the observations of Tylecote (1960) and Matsuno (1980) who reported that blistering results in a loss of contact of the scale. The poorly adhered blistered scale could not be tested in the four-point bending test. Therefore, a zero value was assigned to the critical load required to deadhere scales formed at 950°C, Figure 5.17.

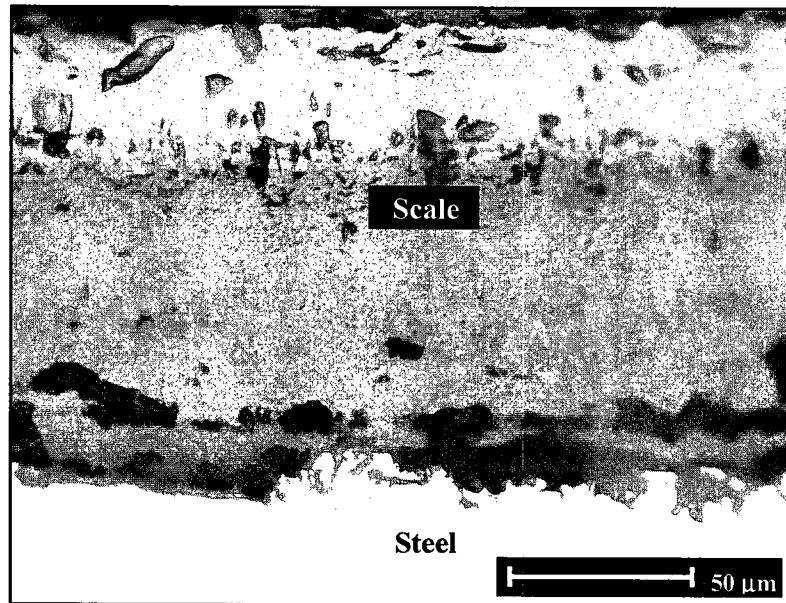


Figure 5.16 Scale formed in air at the temperature of 700°C for 4320 min. showing large pores near the scale/steel interface.

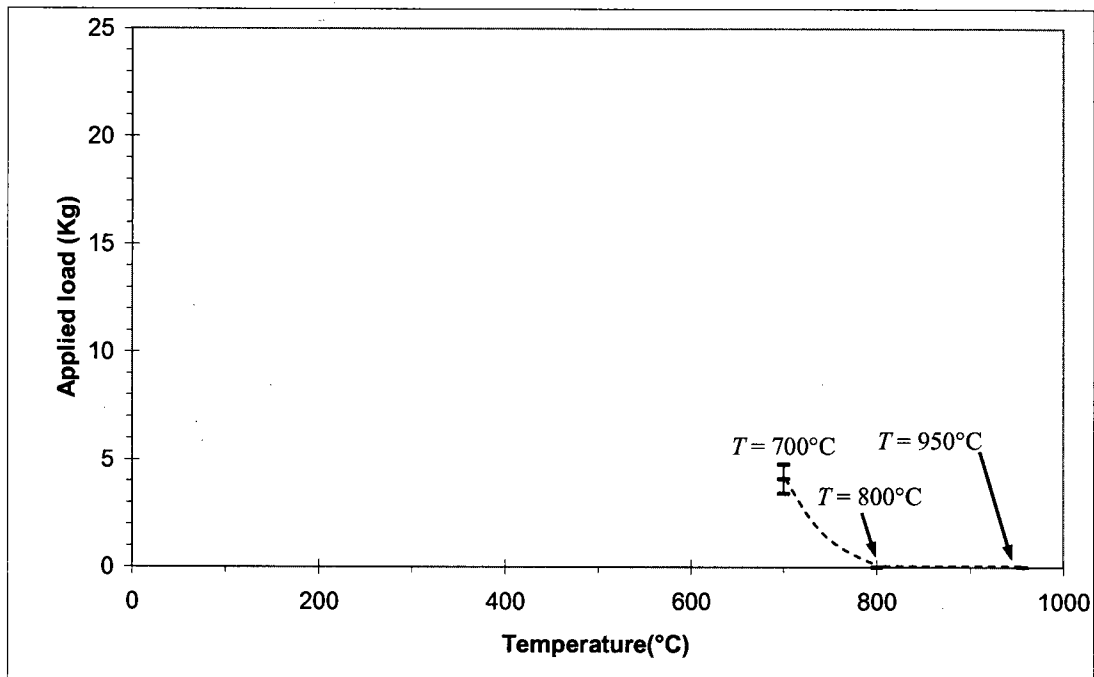


Figure 5.17 Critical load required to deadhere scales of 130 μm in thickness in the four-point bending test at room temperature. The scales were grown in air at the temperatures of 700, 800 and 950°C for 4320, 150 and 10 min. respectively. A zero value was assigned to the scales that spalled when cooling from the temperature of 800°C, and to the detached scales by blistering at 950°C.

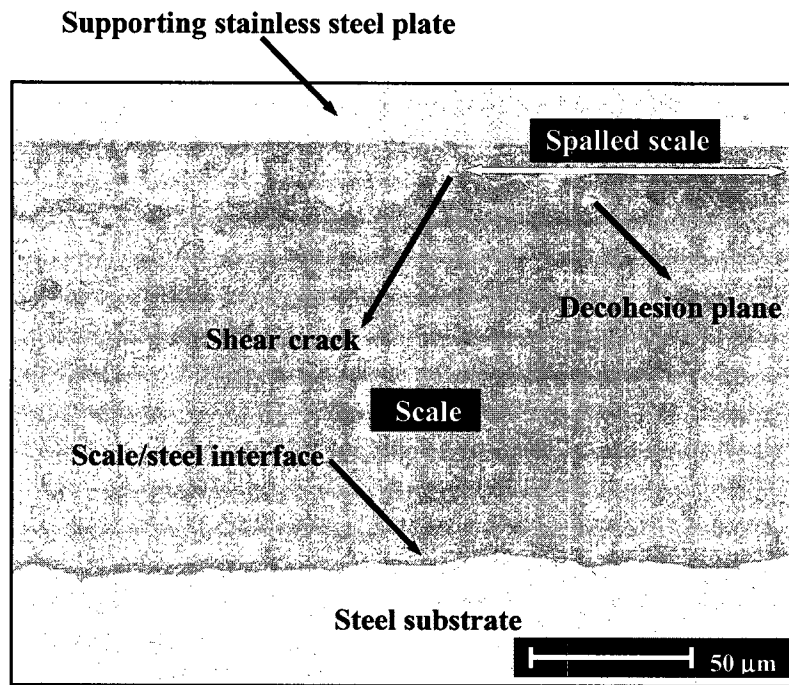


Figure 5.18 Spallation of scale during cooling from 800°C in the isothermal experiments. The decohesion plane was localized in the scale. The spallation occurred close to the outer surface of the scale according to route 1 (strong interface and weak oxide). The scale was formed in air at the temperature of 800°C for 150 min.

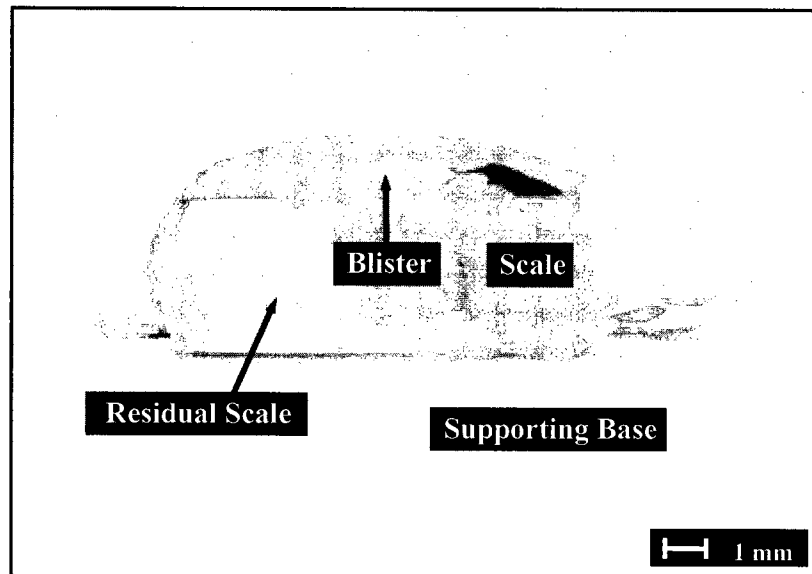


Figure 5.19 Side view photo of a blistered scale formed in air at the temperature of 950°C for 10 min. The adhesion of the blistered scale was low. As a result, during sample handling some blistered scale detached leaving a thin layer of residual scale on the steel substrate.

5.5 Summary

The adhesion of scales grown in air on low carbon steel in continuous heating and isothermal conditions were investigated with a four-point bending test. The results are summarized as follows:

- 1) At room temperature, iron scales were brittle and failed by cleavage. The localization and propagation of the crack always occurred in the scale. This indicated that the fracture strength of the scale/steel interface was higher than the fracture strength of the scale.
- 2) Scale spallation occurred during cooling from 800°C to room temperature in both continuous heating and isothermal conditions. The spallation followed route 1 “strong interface and weak oxide.”
- 3) The increasing temperature and time in the continuous heating schedule increased the porosity of the scale, which in turn reduced the fracture strength of the scale.
- 4) The isothermal experiments at 700, 800 and 950°C showed that thin scales of 130 μm in thickness had low adhesion. The prolonged oxidation at 700°C formed large pores that facilitated the propagation of cracks. Spallation at 800°C and blisters at 950°C formed non-adherent scales.
- 5) In general, the results obtained in the continuous heating and isothermal experiments showed that good adherence required a scale with low porosity, and that bad adherence resulted from high porosity and blisters in scales.

**Effect of O₂ in Heating Atmosphere
on Hydraulic Descaling**

6.1 Introduction

During the hot rolling of steel strip, scales can generate surface defects. To prevent these defects, hydraulic descaling is necessary to remove scales formed during reheating and to ensure the required quality of the final product. There has been considerable work relating hydraulic descaling to scale thickness (Sheppard and Steen, 1970), descaling systems (Sheppard and Steen, 1970; Becker *et al.*, 2000; Frick, 2004; Wolf, September 2000), steel temperature (Sheppard and Steen, 1970; Asai *et al.*, 1997), steel composition (Wolf, September 2000; Asai *et al.*, 1997; Nakamura and Sato, 1994) and scale morphology (Nakamura and Sato, 1994). However, there is relatively little information available on how the heating atmosphere influences hydraulic descaling.

Industrial reheating operations are usually carried out in atmospheres of relatively low oxidizing potential, composed mainly of some free oxygen, carbon dioxide, water vapour and nitrogen. Therefore, hydraulic descaling studies of steels oxidized in atmospheres composed of O₂-CO₂-H₂O-N₂ are of great interest in better understanding hydraulic descaling. In the present work, the effect of O₂ in the heating atmosphere on hydraulic descaling of low carbon steel was analyzed, and results were discussed in relation to scale morphology.

6.2 Objectives

The objective of this chapter is to investigate:

- 1 - The hydraulic descaling of scale grown on low carbon steel under conditions similar to those of reheating furnaces in hot strip mills.
- 2 - The effect of free oxygen on the removability of scale.

- 3 - The influence of oxidation time and temperature on the removability of scale.
- 4 - The influence of scale morphology on the removability of scale.

6.3 Experimental

Low carbon steel specimens were obtained with the chemical composition given in Table 6.1. Before oxidation, the specimens were polished with SiC paper and cleaned with alcohol. A tubular horizontal furnace (Model Mellen Microtherm 1300°C) was used to heat the specimens (50x50x13mm) in an argon atmosphere to 1050, 1100, 1150, 1200 and 1250°C. Then, the inert gas was replaced by the selected oxidizing gas mixture. The specimens were isothermally oxidized for 15, 30, 60 and 120 min. in 1O₂-15CO₂-10H₂O-N₂ and 5O₂-15CO₂-10H₂O-N₂ gas mixtures with a gas velocity of 11.7 cm/s. The gas mixtures of O₂-CO₂-H₂-N₂ were obtained by the experimental procedure described in Chapter 3.

After taking the specimen out of the furnace, the specimen was placed in a rotary disc and accelerated to an angular velocity of 110 rpm (equivalent to a linear velocity of 1.11 m/s), Figure 6.1. The oxide film was removed using a high pressure water jet with a descaling angle of 15°, spray width of 7 mm (at the sample surface), water pressure of 11.37 Mpa and flow rate of 6.8 l/min. Immediately after the hydraulic descaling test, the specimen was placed into a steel tube with a flow of argon and cooled to room temperature. Fast cooling in an argon atmosphere was used to avoid further oxidation and to minimize the decomposition of wüstite. After cooling, scale/steel cross-sections were cut from the slab and mounted for metallographic analyses. In addition to the specimens for the hydraulic descaling test, extra specimens (15x30x13mm) were oxidized for scale morphology observations.

An optical microscope equipped with an image analyzer was used to determine the porosity of the scale by measuring the pore areas and subtracting them from the total

scale area. Before the hydraulic descaling test, the optical microscope was used to measure the scale thickness and inner porous layer thickness, Figure 6.2. After the hydraulic descaling test, the thickness of the residual scale was measured. All the measurements were carried out at ten different points.

Table 6.1 Chemical composition of the steel (wt %).

C	Mn	Si	Cu	P	S	Ni	Mo	V	Sn	Cr
0.06	0.27	0.005	0.006	0.004	0.012	0.01	0.008	0.006	0.003	0.049

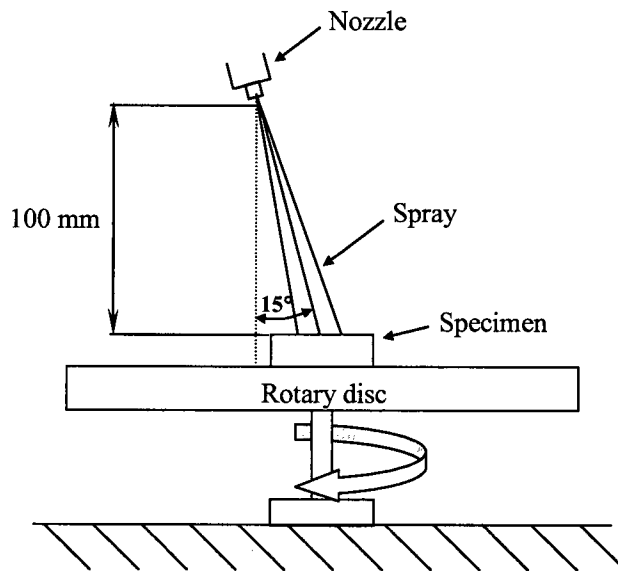


Figure 6.1 Schematic diagram of the hydraulic descaling test.

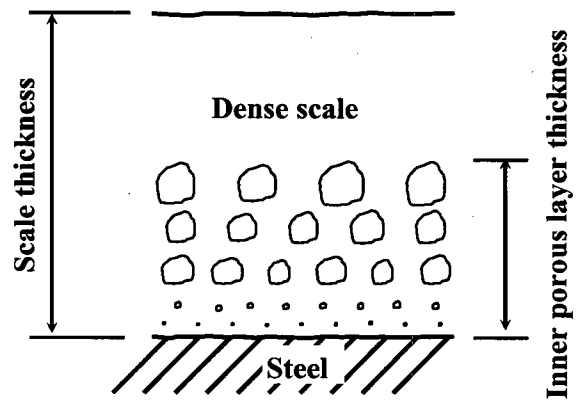


Figure 6.2 Schematic diagram of the scale measurements.

6.4 Results and Discussion

6.4.1 Scale Morphology

Two types of scale were observed: crystalline scale and classical three-layer scale (see Figure 6.3 and Table 6.2). These results correspond with the previous microscopic observations of Chapter 3, in which it was observed that in the oxidation of low carbon steel in weakly oxidizing atmospheres, scales have a crystalline appearance or the classical three-layered formation.

In the 1O₂-15CO₂-10H₂O-N₂ gas mixture, a transition from crystalline scale to three-layer scale was observed at 1150, 1200 and 1250°C, Table 6.2. As mentioned in Chapter 3, this transition occurs when the oxidation time is prolonged, increasing the thickness of the scale. The thicker scale reduces the diffusion of iron, changing the rate-controlling mechanism from the surface reaction (crystalline scale) to the diffusion of iron (classical three-layer scale).

The scales were porous, particularly close to the metal substrate, forming an inner porous layer between the metallic core and dense scale, Figure 6.3. These results correspond to the work of several researchers that observed a concentration of pores close to the metal substrate in the oxidation of steel in laboratory conditions simulating industrial furnaces (Pfeil, 1929; Sachs and Tuck, 1968; Sheasby *et al.*, 1984; Basabe and Szpunar, 2006; Trenkler, 1971; Zitterman *et al.*, 1982) and in industrial furnaces (Sheasby *et al.*, 1984; Abuluwefa *et al.*, 1994). The scales were denser close to the gas phase. This dense scale has been attributed to its formation by outward diffusion of iron (Pfeil, 1929; Sachs and Tuck, 1968).

In the oxidation of iron, porous scales are formed during prolonged oxidation at 850°C and during progressively shorter times at higher temperatures (Sachs and Tuck, 1968; Engell and Wever, 1957). The results of this study showed the same tendency; the

porosity increased with an increase in oxidation time and/or temperature, Table 6.2. It seems that there are two major reasons for the development of porosity: idiomorphic growth and growth stress.

6.4.1.1 Formation of Pores due to Idiomorphic Growth

Sheasby *et al.* (1984) reported that in the initial oxidation of Fe-C alloys in weakly oxidizing atmospheres, pores are formed when some favored grains overgrow others as larger idiomorphic crystals, leaving small pores trapped at the crystal junctions. They also observed that in oxidizing gas mixtures containing water vapour, the pores migrated from the scale/steel interface to the wüstite layer. This pore migration has been attributed to oxidation and reduction reactions that take place in opposite sides of pores filled with H₂O-H₂ or CO₂-CO (Sachs and Tuck, 1968; Sheasby *et al.*, 1984; Rahmel and Tobolski, 1965).

6.4.1.2 Formation of Pores due to Growth Stress

Growth stress in an oxide can result in diffusion creep such as Nabarro-Herring creep and Coble creep (Kofstad, 1988). In Nabarro-Herring creep, an applied shearing stress can cause a solid to yield by a diffusional flow of matter (migration of lattice vacancies or interstitial atoms) within each crystal grain (Herring, 1950), Figure 6.4(a). In Coble creep, the grain boundary, rather than bulk diffusion, is the dominant process that can cause a solid to yield under a shearing stress (Coble, 1963), Figure 6.4(b). Coble creep is the rate controlling process for materials at low or intermediate temperatures, e.g. 0.5 T_{melting} (Evans and Langdon, 1976). Nabarro-Herring creep is the dominant rate controlling process at high temperatures (Nabarro 1948; Herring, 1950). In the present work, the low carbon steel was oxidized over the temperature range 1050-1250°C; therefore, diffusional creep in the oxide occurred most probably through vacancy lattice diffusion (Nabarro-Herring creep).

The mechanism proposed by Evans and Langdon (1976) explains how stress in grains of a polycrystalline material causes diffusion creep and the grains to move relative to each other through the following processes:

- (i) Build-up of material along boundary BC and AB give rise to a velocity vector v_1 and v_2 respectively at the diffusion center of grain (3) (see grain (3) in Figure 6.5(a)). The diffusion center of grain (3) moves away from the triple point B with a velocity \bar{v} . The same diffusion process occurs in all the grains. As a result of the diffusional deformation, all the grains are elongated, Figure 6.5(b).
- (ii) The grains move relative to each other to maintain coherency during diffusion creep, Figure 6.5(c).

The model proposed by Kofstad (1985, 1988) attributes the formation of pores to growth stress in the oxide that causes diffusion creep and grain movement. In his model, grain moves according to the mechanism, described above, of Evans and Langdon (1976), and the formation of pores is controlled by the rates of diffusion creep and grain movement. In the model, porosity is expected to develop at the grain boundaries when the rate of grain movement decreases faster than the rate of diffusion creep.

The scale/steel cross-sections revealed that pores were continuously formed at the grain boundaries, Figure 6.6. Pore formation by idiomorphic growth takes place only in the initial minutes of oxidation (Sheasby *et al.*, 1984). This suggests that the continuous pore formation observed in the present work during 120 min. of oxidation were caused mainly by growth stress in agreement with the model proposed by Kofstad.

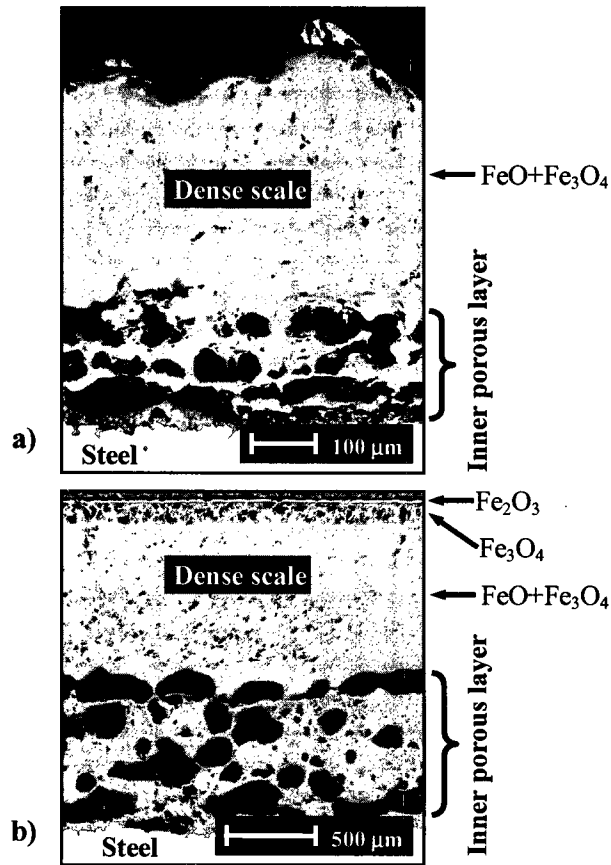


Figure 6.3 Cross-sections of scales formed at 1250°C in: a) 10₂-15CO₂-10H₂O-N₂ for 30 min., crystalline scale showing inner porous layer formation, b) 50₂-15CO₂-10H₂O-N₂ for 120 min., classical three-layer scale showing inner porous layer formation. During cooling some wüstite decomposed, resulting in the precipitation of magnetite in the wüstite layer.

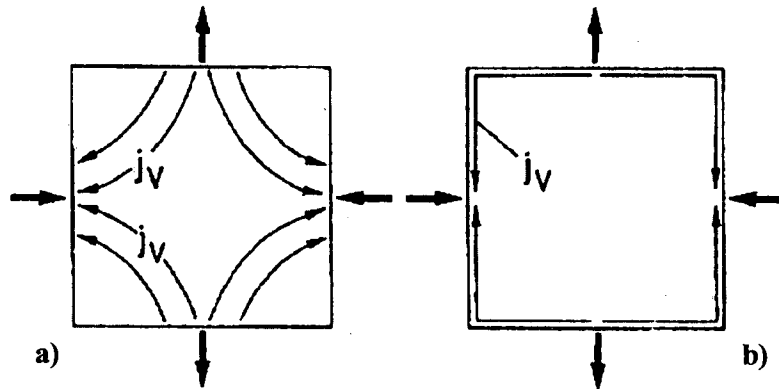


Figure 6.4 Vacancy fluxes, J_v , in single grains due to imposed stresses: a) through vacancy-lattice diffusion (Nabarro-Herring creep); b) through diffusion along grain boundaries (Coble creep). Interstitial defects move in the opposite direction as the vacancies (Kofstad, 1985).

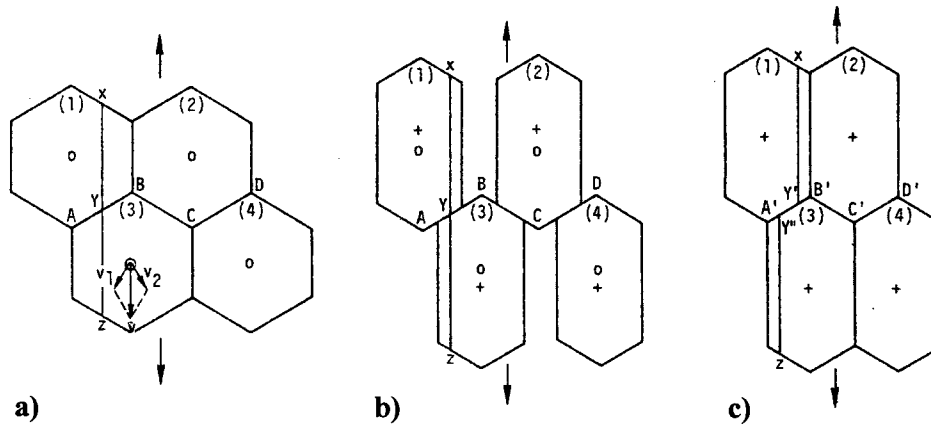


Figure 6.5 a) Four grains in a hexagonal array; the diffusion centers are marked with circles. XYZ is a marker line parallel to the tensile axis. b) The same grains after diffusion creep in the absence of any relative grain movement; the new diffusion centers are marked with crosses. XYZ is in the same relative position. c) The same grains after diffusion creep in the presence of relative grain movement. The marked line is now divided into segments, XY' and Y''Z (After Evans and Langdon, 1976).

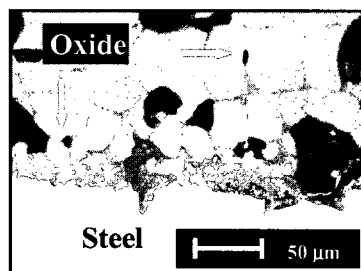


Figure 6.6 Cross-section of scale formed at 1250°C in 5O₂-15CO₂-10H₂O-N₂ for 60 min. showing pore formation (arrowed) at the grain boundaries.

6.4.2 Modes of Scale Removal

In all the hydraulic descaling tests, the scale was removed in the jet impact zone, where the thickness of the residual scale was measured, Figure 6.7. Sheppard and Steen (1970) observed that during hydraulic descaling of steel oxidized in air, the removal of scale occurred when thermal and mechanical impacts of the water jet propagated a horizontal undercutting (crack) at the scale/metal interface. The position of the horizontal undercutting determines the thickness of the residual scale (Sheppard and Steen, 1970; Asai *et al.*, 1997). In the present work, the position of the horizontal undercutting was controlled by the scale morphology. The localization and propagation of the crack always occurred in the scale. This corresponds with the results of Chapter 5, in which it was observed that the fracture strength of the scale is lower than the fracture strength of the scale/steel interface. During the hydraulic descaling tests, two modes of scale removal were observed.

6.4.2.1 Mode I

In mode I, the horizontal undercutting occurred at the boundary of the inner porous layer and dense scale, Figures 6.8 and 6.10. Mode I was observed in three-layer scales that developed a solid inner porous layer with low or medium porosity that resisted the impact of the water jet, Table 6.2.

Previous works on the oxidation of low carbon steel (Preece *et al.*, 1939; Abuluwefa *et al.*, 1997) and steels with various Si content (Nakamura and Sato, 1993) in O₂-CO₂-H₂O-N₂ atmospheres showed that a rise in free oxygen results in higher oxidation rates. In the present work, the rate of oxidation was followed by measuring the scale thickness. A rise in free oxygen from 1% to 5% increased the oxidation rates as reported in previous studies, Figure 6.9(a). In addition, it was observed that the thickness of the inner porous layer increased with increasing free oxygen, oxidation time and/or temperature, Figure 6.9(b).

In mode I, the thickness of the inner porous layer determined the thickness of the residual scale. Therefore, an increase in the inner porous layer thickness with increasing free oxygen, oxidation time and/or temperature, resulted in a thicker residual scale. This point will be taken up in more detail later.

6.4.2.2 Mode II

In mode II, the horizontal undercutting occurred at the first plane of large pores relative to the scale/steel interface, Figures 6.11, 6.12 and 6.14. Mode II was observed in three-layer scales that developed an inner porous layer with high porosity and in crystalline scales, Table 6.2.

The adhesion of scales thermally grown on low carbon steel was studied in Chapter 5. It was found that the fracture strength of scales decreased with increasing porosity. In the hydraulic descaling of a three-layer scale with high porosity, the same tendency was observed (i.e. high porosity resulted in weak scales). In the hydraulic descaling test in mode II, the weak inner porous layer yielded to the impact of the water jet, resulting in a horizontal undercutting at the first plane of large pores relative to the scale/steel interface.

The phase composition of scales formed in O₂-CO₂-H₂O-N₂ gas mixtures was analyzed in Chapter 3; the X-ray analysis showed that crystalline scales were composed mostly of wüstite and a negligible amount of magnetite. Hematite and magnetite form rigid layers in three-layer scales (Tuck *et al.*, 1966). The irregular outer surface and the lack of the rigid layers in crystalline scales, which are mostly formed by wüstite (the softest of the iron oxides), resulted in a deep impact of the water jet. Consequently, in the hydraulic descaling of crystalline scales, the horizontal undercutting always occurred deep in the scale in mode II, independently of the state of porosity.

In mode II, the proximity of the first plane of large pores to the scale/steel interface determined the thickness of the residual scale in both three-layer scales with

high porosity and crystalline scales. Therefore, in mode II, a close first plane of large pores to the scale/steel interface resulted in a thin residual scale, while a distant first plane of large pores from the scale/steel interface resulted in a thick residual scale.

Table 6.2 Mode of scale removal and scale morphology for different temperatures, gas mixtures and oxidation times.

Temp. (°C)	Gas mixture	Time = 15 min.			Time = 30 min.			Time = 60 min.			Time = 120 min.		
		Mode	Structure	Porosity	Mode	Structure	Porosity	Mode	Structure	Porosity	Mode	Structure	Porosity
1050	1O ₂ -15CO ₂ -10H ₂ O-N ₂	1	T	L	1	T	M	2	T	H	2	T	H
1050	5O ₂ -15CO ₂ -10H ₂ O-N ₂	1	T	M	1	T	M	2	T	H	2	T	H
1100	1O ₂ -15CO ₂ -10H ₂ O-N ₂	1	T	M	1	T	M	2	T	H	2	T	H
1100	5O ₂ -15CO ₂ -10H ₂ O-N ₂	1	T	M	1	T	M	2	T	H	2	T	H
1150	1O ₂ -15CO ₂ -10H ₂ O-N ₂	2	C	M	2	C	M	2	C	H	2	T	H
1150	5O ₂ -15CO ₂ -10H ₂ O-N ₂	1	T	M	1	T	M	2	T	H	2	T	H
1200	1O ₂ -15CO ₂ -10H ₂ O-N ₂	2	C	H	2	C	H	2	C	H	2	T	E
1200	5O ₂ -15CO ₂ -10H ₂ O-N ₂	2	T	H	2	T	H	2	T	H	2	T	E
1250	1O ₂ -15CO ₂ -10H ₂ O-N ₂	2	C	H	2	C	H	2	C	H	2	T	E
1250	5O ₂ -15CO ₂ -10H ₂ O-N ₂	2	T	H	2	T	H	2	T	H	2	T	E

Scale structure: T = three-layer scale; C = crystalline scale.

Scale porosity: L = low (porosity ≤ 5%); M = medium (5% < porosity ≤ 10%); H = high (10% < porosity ≤ 20%);

E = extra high (20% < porosity ≤ 30%).

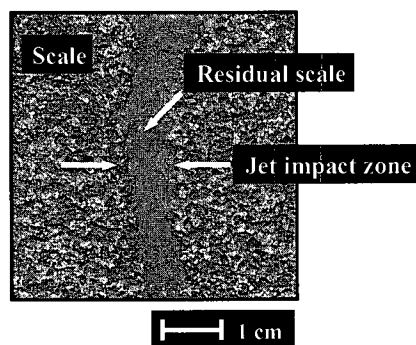


Figure 6.7 Top view of specimen after hydraulic descaling test. The crystalline scale was formed in 1O₂-15CO₂-10H₂O-N₂ for 60 min. at 1250°C.

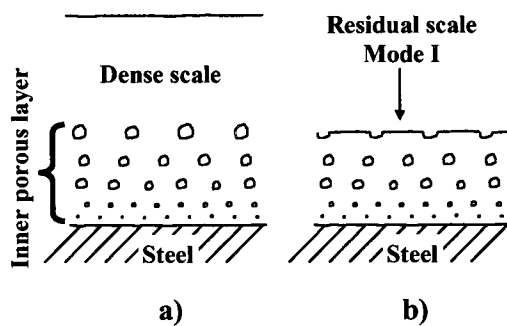


Figure 6.8 Schematic diagram of: a) three-layer scale before hydraulic descaling in mode I, b) residual scale after hydraulic descaling in mode I.

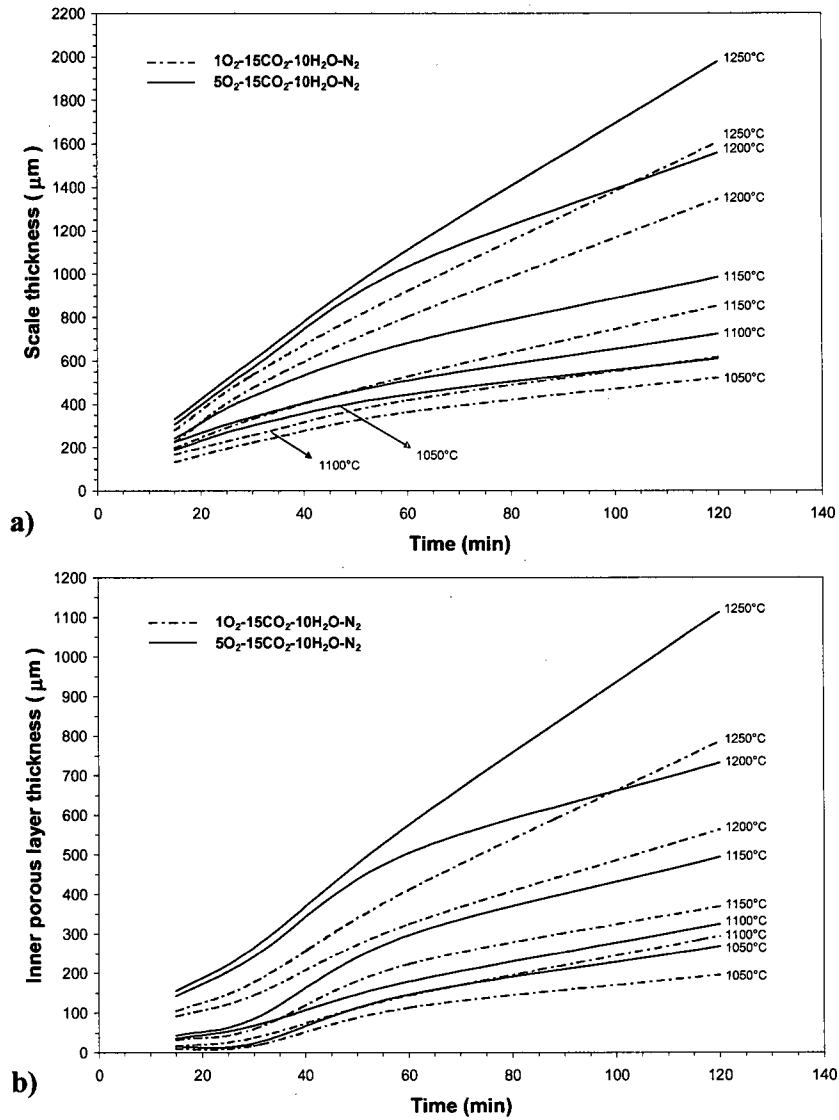


Figure 6.9 Effect of free oxygen, oxidation time and temperature on: a) scale thickness, b) inner porous layer thickness.

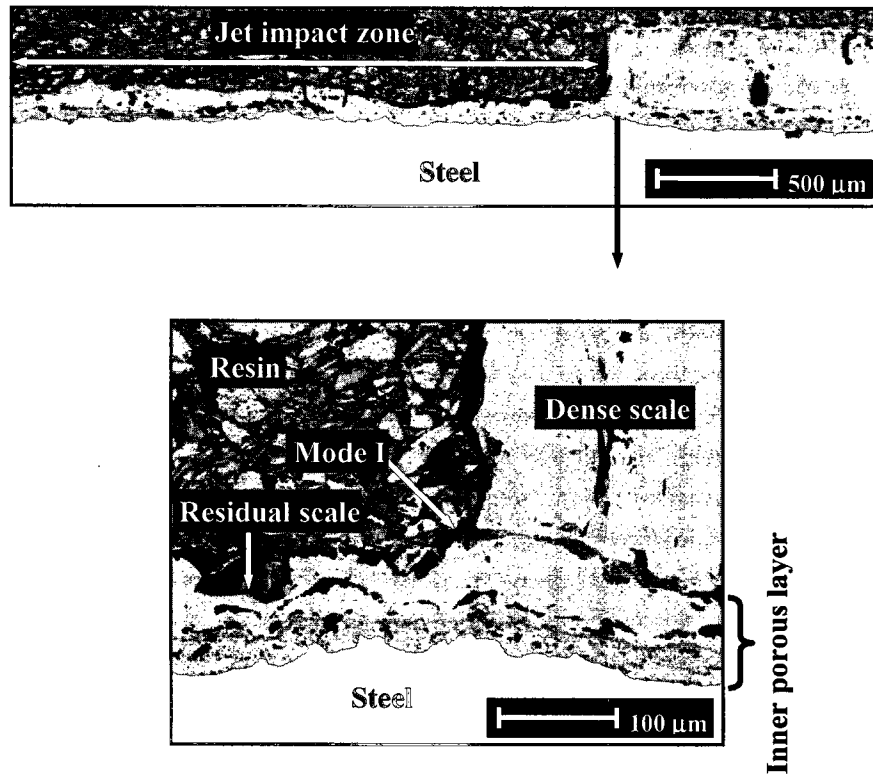


Figure 6.10 Cross-section of three-layer scale after hydraulic descaling in mode I. The three-layer scale was formed in 5O₂-15CO₂-10H₂O-N₂ for 30 min. at 1150°C.

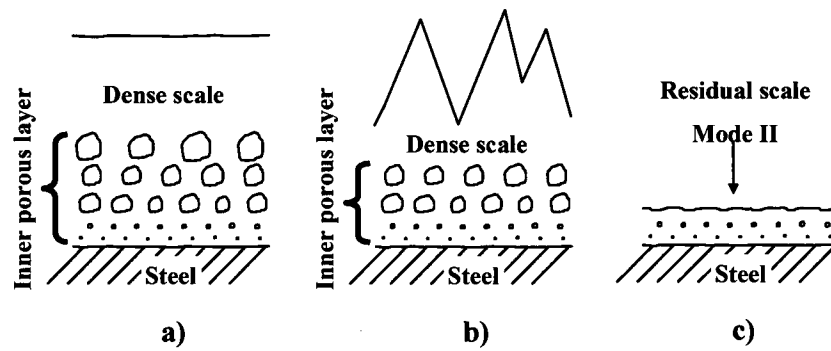


Figure 6.11 Schematic diagram of: a) three-layer scale before hydraulic descaling in mode II, b) crystalline scale before hydraulic descaling in mode II, c) residual scale after hydraulic descaling in mode II.

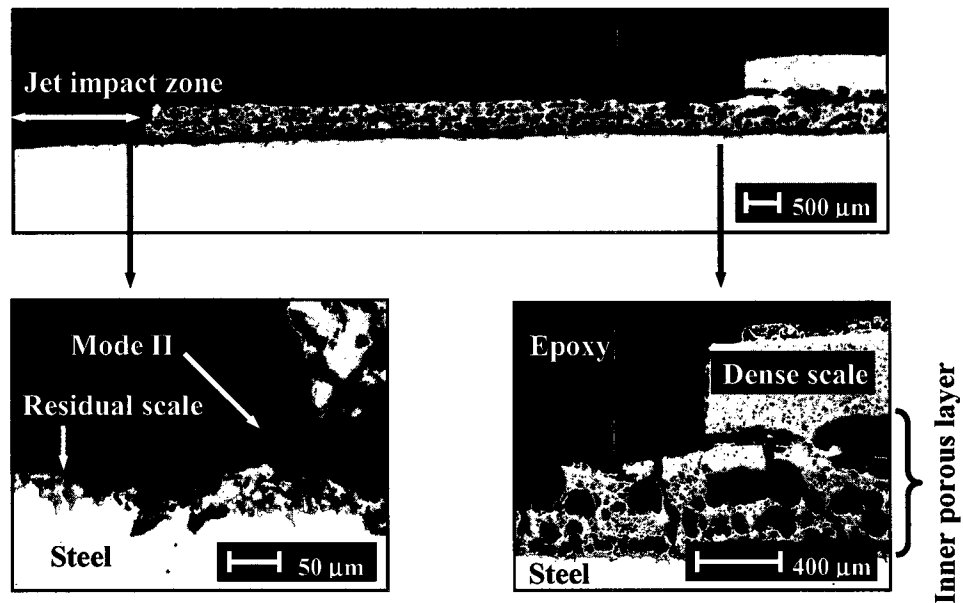


Figure 6.12 Cross-section of three-layer scale after hydraulic descaling in mode II. The three-layer scale was formed in 5O₂-15CO₂-10H₂O-N₂ for 60 min. at 1250°C. Outside of the jet impact zone some dense scale was removed together with the scale of the jet impact zone.

6.4.2 Removability of Scale

Figure 6.13 illustrates the mean thickness of the residual scale, standard deviation and mode of scale removal. For the hydraulic descaling test, the low carbon steel was oxidized for 15, 30, 60 and 120 min. over the temperature range 1050-1250°C in 1O₂-15CO₂-10H₂O-N₂ and 5O₂-15CO₂-10H₂O-N₂ gas mixtures.

Figures 6.13(a)(b) reveal the results for the low carbon steel oxidized at 1050°C in 1O₂-15CO₂-10H₂O-N₂ and 5O₂-15CO₂-10H₂O-N₂ gas mixtures respectively. As mentioned earlier, a rise in free oxygen, oxidation time and/or temperature increased the thickness of the inner porous layer (see Figure 6.9(b)), which in turn resulted in a thicker residual scale in the hydraulic descaling in mode I. During the initial 30 min. of oxidation in 1O₂-15CO₂-10H₂O-N₂ and 5O₂-15CO₂-10H₂O-N₂ gas mixtures, the scales were removed in mode I. Therefore, an increase in the residual scale thickness occurred when the free oxygen and/or oxidation time were raised in the initial 30 min. of oxidation.

After 30 min. of oxidation in 1O₂-15CO₂-10H₂O-N₂ and 5O₂-15CO₂-10H₂O-N₂ gas mixtures, the porosity increased from medium to high porosity, Table 6.2. As a result, the inner porous layer with high porosity could not resist the impact of the water jet and yielded at the weak and porous oxide at the scale/steel interface. Therefore, after 30 min. of oxidation, the potential location for the horizontal undercutting changed from the boundary of the inner porous layer and dense scale (mode I) to the first plane of large pores relative to the scale/steel interface (mode II).

An increase in the oxidation time from 60 to 120 min. in 1O₂-15CO₂-10H₂O-N₂ and 5O₂-15CO₂-10H₂O-N₂ gas mixtures resulted in a first plane of large pores closer to the scale/steel interface. This shifted the horizontal undercutting in mode II closer to the scale/steel interface, reducing the thickness of the residual scale. Figures 6.14(a)(b) show the reduction in residual scale thickness when the oxidation time was increased from 60 to 120 min. in the 1O₂-15CO₂-10H₂O-N₂ gas mixture.

Figures 6.13(c)(d) show the results obtained at 1100°C in 1O₂-15CO₂-10H₂O-N₂ and 5O₂-15CO₂-10H₂O-N₂ gas mixtures respectively. During the initial 30 min. of oxidation in 1O₂-15CO₂-10H₂O-N₂ and 5O₂-15CO₂-10H₂O-N₂ gas mixtures, the horizontal undercutting occurred in mode I. Therefore, thicker residual scales were observed when the free oxygen was increased from 1 to 5%, the oxidation time from 15 to 30 min. and/or the temperature from 1050 to 1100°C, Figures 6.13 (a)-(d).

Similar transitions to the ones observed at 1050°C occurred after 30 min. of oxidation when the porosity increased, changing the mode of scale removal from mode I to mode II, Table 6.2. As a result of the transition from mode I to mode II, the position of the horizontal undercutting became controlled by the proximity of the first plane of large pores to the scale/steel interface. After 120 min. of oxidation, the proximity of the first plane of large pores to the scale/steel interface was similar in 1O₂-15CO₂-10H₂O-N₂ and 5O₂-15CO₂-10H₂O-N₂ gas mixtures, resulting in small differences in the residual scale thickness.

Figures 6.13(e)(f) illustrate the results at 1150°C in 1O₂-15CO₂-10H₂O-N₂ and 5O₂-15CO₂-10H₂O-N₂ gas mixtures respectively. In the 1O₂-15CO₂-10H₂O-N₂ gas mixture, crystalline scales formed during the initial 60 min. of oxidation, and three-layer scales with high porosity formed after 60 min. of oxidation had the horizontal undercutting at the first plane of large pores relative to the scale/steel interface (mode II), Table 6.2. During the initial 30 min. of oxidation, the hydraulic descaling in mode II resulted in a thinner residual scale in the 1O₂-15CO₂-10H₂O-N₂ gas mixture; the horizontal undercutting took place closer to the scale/steel interface than in the scales grown in the 5O₂-15CO₂-10H₂O-N₂ gas mixture, which were removed farther away from the scale/steel interface in mode I. Figure 6.14(c) shows a typical crystalline scale removed in mode II.

In the 5O₂-15CO₂-10H₂O-N₂ gas mixture, mode I was observed during the initial 30 min. of oxidation; therefore, a rise in oxidation time from 15 to 30 min. increased the thickness of the residual scale. In addition, a rise in temperature from 1050, 1100 to 1150°C increased the thickness of the inner porous layers (see Figure 6.9(b)), which in

turn resulted in thicker residual scales in the hydraulic descaling in mode I. Figures 6.13 (a)-(d) and (f). As in the experiments at 1050 and 1100°C, an increase in porosity from medium to high resulted in a transition from mode I to mode II after 30 min. of oxidation, Table 6.2.

After 120 min. of oxidation, pore migration was observed in the scales formed in low 1O₂-15CO₂-10H₂O-N₂ and high 5O₂-15CO₂-10H₂O-N₂ oxygen content gas mixtures. The migration of pores from the scale/steel interface to the wüstite layer is counteracted in the opposite direction by creep of the oxide, which accompanies scale growth (Sheasby *et al.*, 1984). In general, creep increases with temperature; therefore, it is reasonable to assume that a rise in temperature from 1050 and 1100 to 1150°C increased creep in wüstite, facilitating the migration of pores into the wüstite layer. Pore migration after 120 min. of oxidation at 1150°C shifted the horizontal undercutting in mode II farther away from the scale/steel interface, resulting in thicker residual scales. In the migration process, pores usually acquire a cap shape with the convex surface in the direction of scale growth (Sheasby *et al.*, 1984). Figure 6.14(d) shows a typical scale with migrated pores (cap shape).

Figures 6.13(g)(h) show the results at 1200°C in 1O₂-15CO₂-10H₂O-N₂ and 5O₂-15CO₂-10H₂O-N₂ gas mixtures respectively. In the oxidation of steel at high temperatures, pore coalescence forms large pores in thick scales (Tuck *et al.*, 1966). At 1200 and 1250°C, pore coalescence formed large pores in the scales. The high porosity and pore coalescence masked the migrated pores in the wüstite layer. The pores were large and distributed across the inner porous layer. Figures 6.12 and 6.14(e)(f) show typical scales with large pores formed by coalescence. The inner porous layers with high porosity could not resist the impact of the water jet and were removed. Therefore, mode I was absent in all the experiments at 1200 and 1250°C. The extremely weak oxide close to the scale/steel interface was the potential location for the horizontal undercutting at 1200°C and 1250°C. Consequently, the horizontal undercutting occurred at the first plane of large pores relative to the scale/steel interface (mode II). In general, at 1200 and 1250°C the concentration of free oxygen in the gas mixture had little effect on the proximity of the first plane of large pores to the scale/steel interface. As a result,

the differences in the residual scale thickness with increasing free oxygen were small at 1200°C.

Figures 6.13(i)(j) reveal the results at 1250°C in 1O₂-15CO₂-10H₂O-N₂ and 5O₂-15CO₂-10H₂O-N₂ gas mixtures respectively. As mentioned above, at 1250°C the concentration of free oxygen in the gas mixture had little effect on the proximity of the first plane of large pores to the scale/steel interface, resulting in residual scales with similar thickness in the 1O₂-15CO₂-10H₂O-N₂ and 5O₂-15CO₂-10H₂O-N₂ gas mixtures.

Typical delivery temperatures of a tunnel furnace are in the range of 1050-1150°C (Ramírez-Cuellar *et al.*, 2003). The experiments showed that during the initial 30 min of oxidation at 1050, 1100 and 1150°C, scales formed in the low oxygen content 1O₂-15CO₂-10H₂O-N₂ gas mixture had thinner residual scales than scales formed in high oxygen content 5O₂-15CO₂-10H₂O-N₂ gas mixture. This suggests that reducing the concentration of free oxygen in the tunnel furnace atmosphere is important for increasing scale removability.

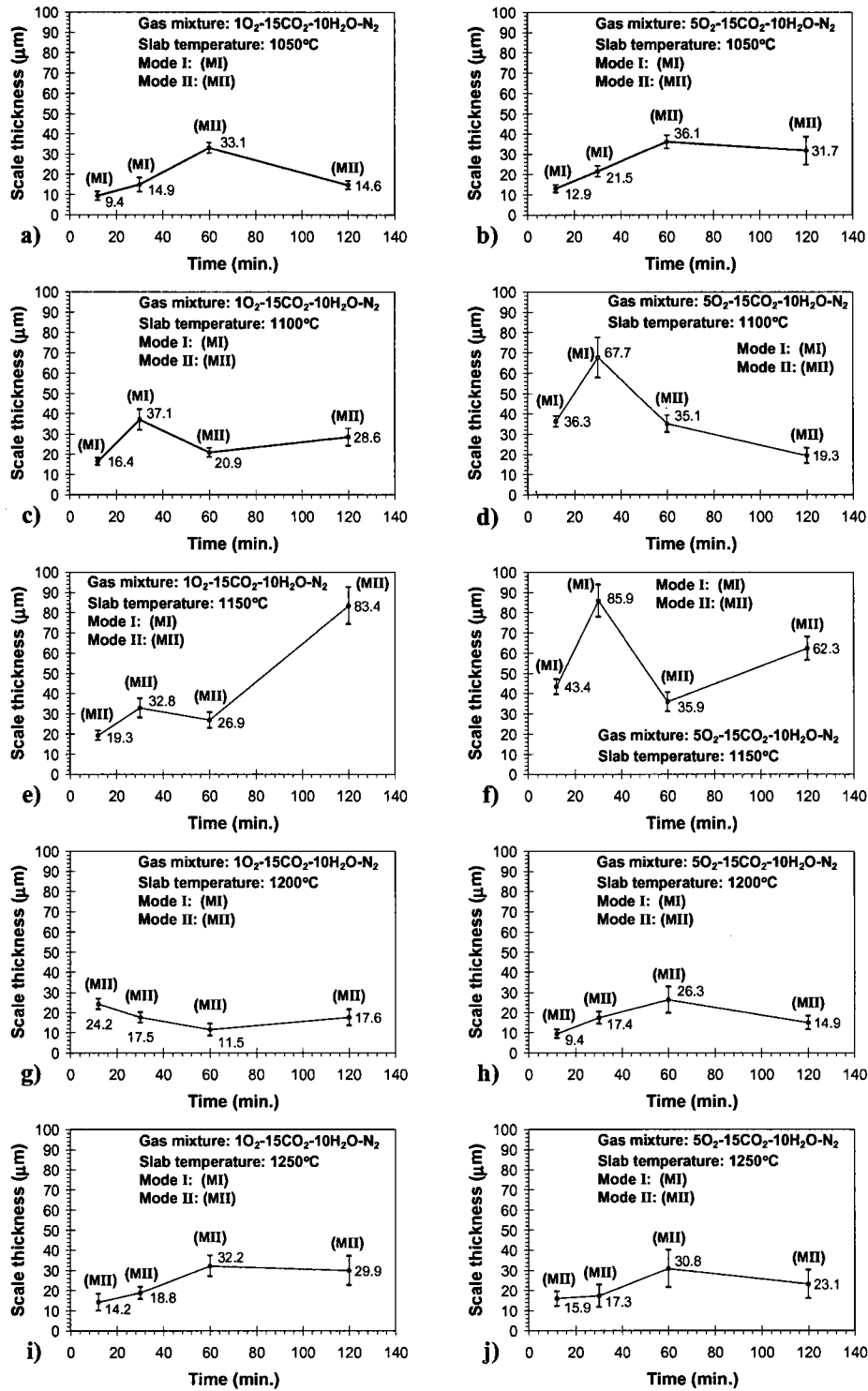


Figure 6.13 Mean thickness of the residual scale, standard deviation and mode of scale removal as a function of temperature, free oxygen and oxidation time. The low carbon steel was oxidized for 15, 30, 60, 120 min. in 10₂-15CO₂-10H₂O-N₂ at: a) 1050°C, c) 1100°C, e) 1150°C, g) 1200°C, i) 1250°C, and in 50₂-15CO₂-10H₂O-N₂ at: b) 1050°C, d) 1100°C, f) 1150°C, h) 1200°C, j) 1250°C.

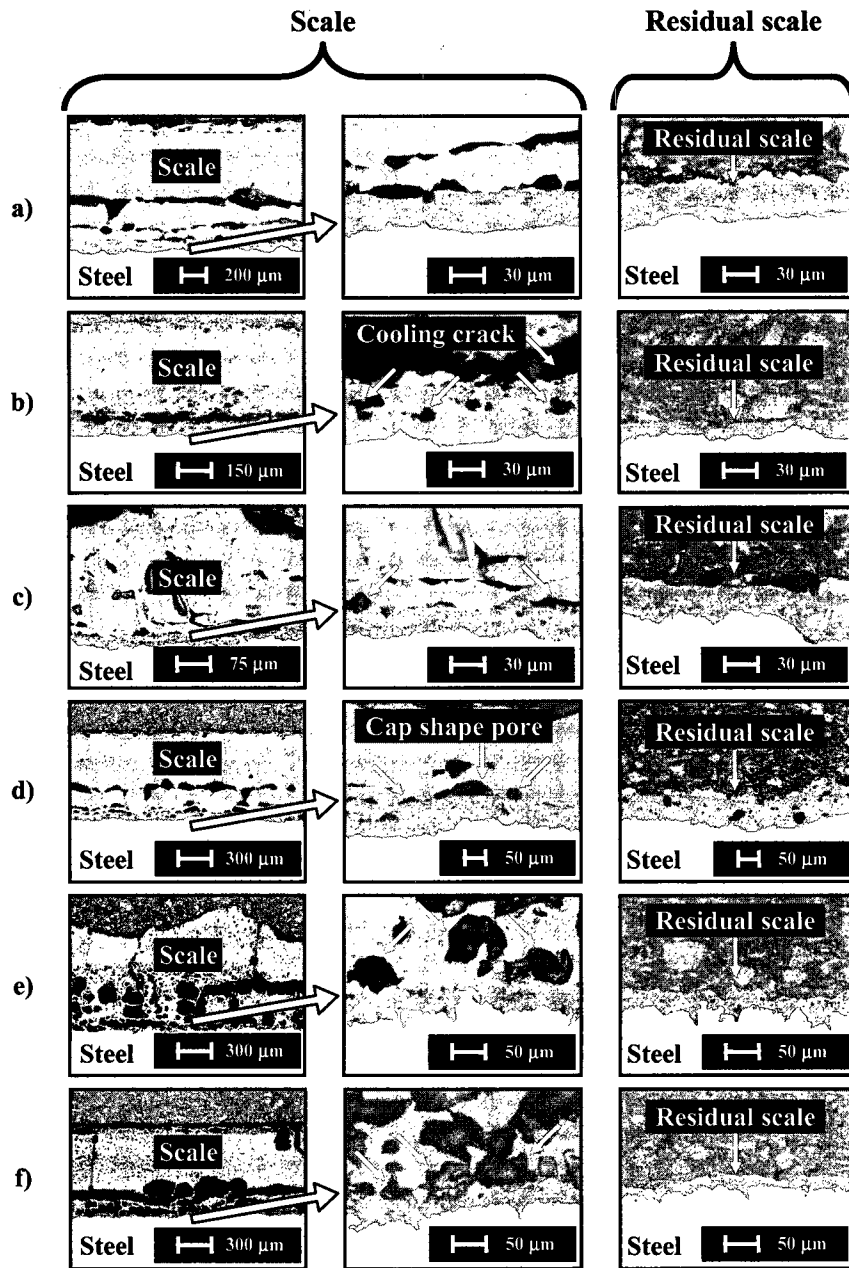


Figure 6.14 Cross-sections of scales and their residual scales after hydraulic descaling in mode II. The pores (arrowed) of the first plane of large pores relative to the scale/steel interface are indicated in the middle column. The scales were formed in: a) 1O₂-15CO₂-10H₂O-N₂ for 60 min. at 1050°C, three-layer scale, b) 1O₂-15CO₂-10H₂O-N₂ for 120 min. at 1050°C, three-layer scale, c) 1O₂-15CO₂-10H₂O-N₂ for 30 min. at 1150°C, crystalline scale, d) 1O₂-15CO₂-10H₂O-N₂ for 120 min. at 1150°C, three-layer scale, e) 1O₂-15CO₂-10H₂O-N₂ for 60 min. at 1250°C, crystalline scale, f) 5O₂-15CO₂-10H₂O-N₂ for 30 min. at 1250°C, three-layer scale.

6.5 Summary

The effect of O₂ in the heating atmosphere on hydraulic descaling of low carbon steel was investigated, and the results are summarized as follows:

- 1) Two modes of scale removal were observed. In the first mode, the horizontal undercutting occurred at the boundary of the inner porous layer and dense scale. In the second mode, the horizontal undercutting occurred at the first plane of large pores relative to the scale/steel interface.
- 2) A rise in the concentration of free oxygen resulted in an increase in thickness of the residual scale at 1050°C. At 1100°C and 1150°C, the increase in residual scale thickness with increasing free oxygen was significant in the initial 60 min. of oxidation; after this period of time the differences in the thickness of the residual scale became smaller. The influence of free oxygen in the residual scale thickness was small at 1200°C, and negligible at 1250°C.
- 3) The oxidation time and temperature influenced the removability of scale. During the initial 30 min. of oxidation, an increase in the oxidation time and/or temperature in the formation of three-layer scales in the temperature range 1050-1150°C resulted in thicker residual scales. After 30 min. of oxidation, an increase in the oxidation time caused a transition from mode I to mode II in three-layer scales formed in the temperature range 1050-1150°C. At 1200°C and 1250°C, the high temperatures formed scales with high porosity that were removed in mode II.
- 4) The phase composition of the scale influenced the mode of scale removal. Crystalline scales mostly composed of soft wustite always had the horizontal undercutting at the first plane of large pores relative to the scale/steel interface (mode II), independently of the state of porosity.

**Conclusions, Contribution to Knowledge
and Suggested Future Work**

7.1 Conclusions

The analysis of the scales formed on low carbon steel in O_2 - CO_2 - H_2O - N_2 , O_2 - H_2O - N_2 and O_2 - CO_2 - N_2 gas mixtures over the temperature range 1000-1250°C indicated that scales can be classified as two types: crystalline scale and classical three-layer scale. The results obtained are in agreement with the work of several researchers (Preece *et al.*, 1939; Sheasby *et. al.*, 1984; Abuluwefa, 1996) who reported that an increase in free oxygen in the furnace atmosphere increases the percentages of magnetite and hematite in the scale. In addition, it was observed that an increase in oxidation time at a constant temperature increased the percentages of magnetite and hematite. Furthermore, it was found that in water vapour-free atmospheres, the gaps near the scale/steel interface resulted in a reduction of the percentage of wüstite and in an increase in the percentages of magnetite and hematite. The present study showed that: a) in hot strip mills utilizing the traditional thick slab casting and rolling technology, the high temperatures and prolonged reheating times are likely to form a scale rich in wüstite with the classical three-layered formation in both low and high oxygen content atmospheres, b) in hot strip mills utilizing thin slab casting and rolling technology, the scales formed in tunnel furnaces can have either the crystalline or the classical three-layered formation.

The oxidation of low carbon steel in air over the temperature range 800-1200°C showed that during the initial 30 s of oxidation, wüstite is the predominant phase and hematite is negligible. This suggests that reducing the time of scale growth in hot rolling is necessary in order to reduce work roll wear by rolling in the presence of an oxide with a high percentage of wüstite (the softest of the iron oxides) and with a low percentage of hematite (the hardest of the iron oxides). Such a reduction in time of scale growth in the finishing strip mill can be achieved by controlling the descaler location, mill speeds, reduction practices, entry thickness and mill spacing (Blazevic, 1996). Lowering surface temperature is necessary to reduce the possibility of rolling a thick, non-homogeneous scale that can generate surface defects. However, the present study showed that the reduction in scale thickness and increase in oxide scale homogeneity are only achieved for temperatures $\leq 850^\circ\text{C}$. At 850°C , the oxide was homogeneous,

and for the first 120 s of oxidation, the oxide had a high percentage of wüstite and a low percentage of hematite. This indicates that 850°C is the ideal temperature for the finishing strip mill. A rolling temperature of 850°C allows reduction of work roll wear by rolling with a high percentage of wüstite and a low percentage of hematite, and it improves surface quality by rolling a homogeneous thin oxide scale. The microtexture analysis of scales formed in air for 10 s over the temperature range 850-950°C indicated that: a) during hot rolling of low carbon steel in the γ region, the scale has a cube texture $\{001\}\langle 100\rangle$, and b) when rolling in the α region, the texture of the scale is weak with no dominant texture components.

The four-point bending test proved to be a useful tool for measuring the adhesion of scales grown on low carbon steel. The adhesion tests at room temperature showed that scales under a normal tensile stress had the separation (crack) inside the scale, indicating that the fracture strength of the scale was lower than the fracture strength of the scale/steel interface. From the spallation of scale observed during cooling from 800°C to room temperature in both continuous heating and isothermal conditions, it was found that the spallation of scale grown on low carbon steel followed route 1, "strong interface and weak oxide." The continuous heating and isothermal experiments showed that the adhesion of scale was influenced by scale morphology, which in turn was influenced by the oxidation time, heating schedule and temperature. In general, the experiments showed that good adherence required a scale with low porosity, and that bad adherence resulted from high porosity and blisters in scales.

In the hydraulic descaling of scales formed on low carbon steel in O_2 - CO_2 - H_2O - N_2 gas mixtures over the temperature range 1050-1250°C, two modes of scale removal were observed. In mode I, observed in a classical three-layer scale that developed an inner porous layer with low or medium porosity, the horizontal undercutting occurred at the boundary of the inner porous layer and dense scale. In mode II, observed in a classical three-layer scale, which developed an inner porous layer with high porosity, and in crystalline scales, the horizontal undercutting occurred at the first plane of large pores relative to the scale/steel interface. The main conclusion was that the removability of scale was influenced by the scale morphology, which in turn was influenced by

oxidation time, temperature and free oxygen in the furnace atmosphere. The experiments at 1050, 1100 and 1150°C showed that in hot strip mills using thin slab casting and rolling technology, a reduction in the concentration of free oxygen in the tunnel furnace atmosphere is important for increasing scale removability.

Finally, it is concluded in the present work that the morphology of the scales in the hot rolling process can be controlled by oxidation time, temperature and oxidizing atmosphere. The scale morphology influences the surface strip quality, work roll wear and removability of the scale. Thus, the control of the scale morphology becomes of paramount importance in the different stages of the hot rolling process. This control can be implemented by the X ray and microscopy analyses applied in the present work. The control of the morphology of the scales will allow hot strip mills to optimize scale formation and descaling operations.

7.2 Contribution to Knowledge

- 1) Quantitative X-ray diffraction phase analysis was used to determine the phase composition of scales in several oxidizing conditions similar to those of hot rolling. It was for the first time that the volume fractions of wüstite, magnetite and hematite were determined in oxidation times as short as 30 s.
- 2) Thermo gravimetric analysis (TGA) and scanning electron microscopy (SEM) were used to study the evolution of scales in short times of oxidation ≤ 120 s. The detailed observations revealed the growth rate and scale morphology in short times of oxidation. The results obtained increased the understanding of secondary and tertiary scales in hot rolling.
- 3) Orientation imaging microscopy (OIM) was used to characterize scales. For the first time, scales grown in oxidation time as short as 10 s were characterized to reveal the microstructure of tertiary scales; the relation between temperature and texture of the scale was established over the temperature range 800-950°C.

4) A four-point bending test was used to analyze the adhesion of scales grown on low carbon steel. The influence of scale morphology on scale adhesion was investigated in details. The present work revealed the link between scale morphology and scale adhesion in different oxidizing conditions. The results obtained increased the understanding of the adhesion of scales thermally grown on low carbon steel.

5) The effect of O₂ in heating atmosphere on hydraulic descaling of scales formed in conditions similar to those of reheating furnaces was investigated in details. The results increased the understanding of the removability of scales formed during reheating in hot strip mills. The present work identified more favorable heating conditions for hydraulic descaling in hot strip mills utilizing thin slab casting and rolling technology.

7.3 Suggested Future Work

7.3.1 The Effect of H₂O on Hydraulic Descaling

Water vapour has a considerable influence on the morphology and phase composition of the oxide scales. In Chapter 3, it was concluded that the absence of water vapour in the furnace atmosphere results in scales with a gap formation near the scale/steel interface and in a scale rich in magnetite and hematite. It would be of great value to determine the influence of water vapour on the removability of the scale. By thoroughly understanding the effect of H₂O on scale removability, future models of descaling will become more accurate.

7.3.2 The Effect of Nickel in Steel on Hydraulic Descaling

In the steel making process the necessity to recycle scrap tends to increase continuously. Scrap contains tramp elements (e.g. Ni, Cu, Sn, Zn) that are difficult to

eliminate. Nickel in particular affects the descaling process. Asai *et al.* (1997) found that the unevenness of the scale/metal interface in the steels with high nickel content resulted in a lower descalability than that of the steels with low nickel. In addition to the unevenness of the scale/metal interface, they suggested that scale morphology could influence the removability of scale. More work needs to be done to clarify the influence of Nickel in the morphology and removability of scales grown in conditions similar to those of reheating furnaces in hot strip mills.

References

Abuluwefa, H., 1996, *Ph. D. Thesis*, McGill University, Quebec.

Abuluwefa, H., Guthrie, R. I. L. and Ajersch, F., 1997, *Metallurgical and Materials Transactions A*, Vol. 28A, pp. 1633-1641.

Abuluwefa, H., Guthrie, R. I. L. and Mucciardi, F., 1993, *Proceedings of the 34th MWSP Conference*, Iron and Steel Society, ISS-AIME, Vol. XXX, pp. 453-467.

Adams, B. L., 1997, *Ultramicroscopy*, Vol. 67, pp 11-17.

Asai, T., Soshiroda, T. and Miyahara, M., 1997, *ISIJ International*, Vol. 37, pp. 272-277.

Atkinson, A. and Guppy, R., 1991, *Materials Science and Technology*, Vol. 7, pp. 1031-1041.

Averbach, B. L. and Cohen, M., 1948, *Trans. AIME*, Vol. 176, pp. 401-415.

Basabe, V. V. and Szpunar, J. S., 2004, *ISIJ International*, Vol. 44, pp. 1554-1559.

Basabe, V. V. and Szpunar, J. S., 2006, *Steel Research International*, Vol. 77, pp. 818-824.

Becker, E., Birkemeier, G., Buchele, W., Degner, M., Devrient, L., Nowak, M. and Thiemann, G., 2000, *Metallurgical Plant and Technology*, Vol. 23, pp. 92-97.

Biederman, R. R., Bourgault, R. F. and Smith, R. W., 1974, *Advances in X-Ray Analysis*, Vol. 17, pp. 139-149.

Birks, N., 1973, *Iron and Steel Institute*, Publication No. 146, pp. 402-411.

References

Birks, N. and Meier, G. H., 1983, *Introduction to High Temperature Oxidation of Metals*, Edward Arnold, London.

Birosca, S., Dingley, D. and Higginson, R. L., 2004, *Journal of Microscopy*, Vol. 213, pp. 235-240.

Blazevic, D. T., 1996, *Proceedings of the 37th MWSP Conference*, Iron and Steel Society, ISS-AIME, Vol. XXXIII, pp. 33-38.

Blazevic, D. T., 1997, *Proceedings of the 2nd International Conference on Hydraulic Descaling in Rolling Mills*, The Institute of Materials, London, pp. 1-8.

Bohnenkamp, K. and Engell, H. J., 1959, *Archiv für das Eisenhüttenwesen*, Vol. 30, pp. 275-282.

Brandon, D. and Kaplan, W. D., 1999, *Microstructural Characterization of Materials*, John Wiley & Sons Ltd, Great Britain.

Burke, D.P. and Higginson, R.L., 2000, *Scripta Materialia*, Vol. 42, pp. 277-281.

Buscail, H., Larpin, J.P., Heizmann, J.J. and Laruelle, C., 1995, *Revue de Metallurgie, Cahiers d'Informations Techniques*, Vol. 92, pp. 661-670.

Caplan, D. and Cohen, M., 1966, *Corrosion Science*, Vol. 6, pp. 321-335.

Chen, W. C., Samarasekera, I. V., Kumar, A. and Hawbolt, E. B., 1993, *Ironmaking Steelmaking*, Vol. 20, pp. 113-125.

Coble, R. L., 1963, *Journal of Applied Physics*, Vol. 34, pp. 1679-1682.

Cook, E. A. and Rasmussen, K. E., 1970, *Iron and Steel Engineer Year Book*, pp. 175-181.

References

- Cornell, R. M. and Schwertmann, U., 2003, *The Iron Oxides*, Wiley-VCH, Weinheim.
- Cullity, B. D., 1978, *Elements of X-ray Diffraction*, Addison-Wesley Publishing Company, United States of America.
- Cullity, B. D. and Stock, S. R., 2001, *Elements of X-ray Diffraction, Third Edition*, Prentice Hall, United States of America.
- Darken, L. S. and Gurry, R. W., 1945, *Journal of the American Chemical Society*, Vol. 67, pp. 1398-1412.
- Darken, L. S. and Gurry, R. W., 1946, *Journal of the American Chemical Society*, Vol. 68, pp. 798-816.
- Dingley, D. J., Baba-Kishi, K. Z. and Randle, V., 1995, *Atlas of Backscattering Kikuchi Diffraction Patterns*, The Institute of Physics, UK.
- Donini, E. A., Borsi, R. and Carboni, A., 1997, *Iron and Steel Engineer*, Vol. 74, pp. 39-44.
- El-Kalay, A. K. E. H. A. and Sparling, L. G. M., 1968, *Journal of The Iron and Steel Institute*, Vol. 43, pp. 152-168.
- Elsner, G., Suga, T. and Turwitt, M., 1985, *Journal de Physique*, Vol. 46, pp. 597-612.
- Engell, H. and Wever, F., 1957, *Acta Metallurgica*, Vol. 5, pp. 695-702.
- Evans, A. G. and Langdon, T. G., 1976, *Progress in Materials Science*, Vol. 21, pp. 171-441.
- Evans, H. E., 1988, *Materials Science and Technology*, Vol. 4, pp. 415-420.

References

Evans, H. E. and Lobb, R. C., 1984, *Corrosion Science*, Vol. 24, pp. 209-222.

Evans, U. R., 1948, *An Introduction to Metallic Corrosion*, Edward Arnold & CO., London.

Frick, J. W., 2004, *Metallurgical Plant and Technology*, Vol. 27, pp. 90-93.

Fukagawa, T., Okada, H. and Fujikawa, H., 1997, *Tetsu-to-Hagane*, Vol. 83, pp. 305-310.

Fukagawa, T., Okada, H. and Maehara, Y., 1995, *Tetsu-to-Hagane*, Vol. 81, pp. 559-564.

Fultz, B. and Howe, J. M., 2002, *Transmission Electron Microscopy and Diffractometry of Materials*, Springer, Germany.

Gandhi, C. and Ashby, M. F., 1979, *Acta Metallurgica*, Vol. 27, pp 1565-1602.

Gaskell, D. R., 1995, *Introduction to the Thermodynamics of Materials*, Taylor & Francis, United States of America.

Ginzburg, V. B. and Ballas, R., 2000, *Flat Rolling Fundamentals*, Marcel Dekker Inc, New York.

Griffiths, R., 1934, *Journal of the Iron and Steel Institute*, Vol. 130, pp. 377-388.

Hancock, P. and Hurst, R. C., 1970, *Adv. Corrosion Science Technology*, Vol. 4, pp. 1-84.

Hauffe, K., 1954, *Metalloberfläche*, Vol. 8, pp. 97-103.

References

Hedden, K. and Lehmann, G., 1964, *Archiv für das Eisenhüttenwesen*, Vol. 35, pp. 839-846.

Herring, C., 1950, *Journal of Applied Physics*, Vol. 21, pp. 437-445.

Higginson, R.L., Roebuck, B. and Palmiere, E.J., 2002, *Scripta Materialia*, Vol. 47, pp. 337-342.

Humphreys, F. J., 2001, *Journal of Materials Science*, Vol. 36, pp. 3833-3854.

Irwin, G. R., 1957, *Journal of Applied. Mechanics*, Vol. 24, pp. 361-364.

Jaenicke, W., Leistikow, S. and Stadler, A., 1964, *Journal of the Electrochemical Society*, Vol. 111, pp. 1031-1037.

James, R. W., 1962, *The Optical Principles of the Diffraction of X-Rays*, G. Bell and Sons Ltd, London.

JCPDF 6-0615 card, 1974, *Wustite, Powder Diffraction Data*, Joint Committee on Powder Diffraction Standards, Philadelphia, p. 127.

JCPDF 11-614 card, 1974, *Magnetite, Powder Diffraction Data*, Joint Committee on Powder Diffraction Standards, Philadelphia, p. 159.

JCPDF 13-534 card, 1974, *Hematite, Powder Diffraction Data*, Joint Committee on Powder Diffraction Standards, Philadelphia, p. 562.

Jominy, W. E. and Murphy, D. W., 1930, *Transactions of the A. S. S. T.*, Vol. 18, pp. 19-57.

Jones, D. A., 1996, *Principles and Prevention of Corrosion, 2nd Edition*, Prentice-Hall, United States of America.

References

Khanna, A. S., 2002, *High Temperature Oxidation and Corrosion*, ASM International, United States of America.

Kim, B. K. and Szpunar, J. A., 2001, *Scripta Materialia*, Vol. 44, pp. 2605-2610.

Kofstad, P., 1985, *Oxidation of Metals*, Vol. 24, pp. 265-276.

Kofstad, P., 1988, *High Temperature Corrosion*, Elsevier Applied Science Publishers Ltd, London and New York.

Kor, G. J. W. and Turkdogan, E. T., 1971, *Metallurgical Transactions*, Vol. 2, pp. 1571-1578.

Krzyzanowski, M. and Beynon, J. H., 1999, *Steel Research International*, Vol. 70, pp. 22-27.

Kubaschewski, O. and Hopkins, B. E., 1962, *Oxidation of Metals and Alloys*, Academic Press, London.

Lenard, J. G., Pietrzyk, M. and Cser, L., 1999, *Mathematical and Physical Simulation of the Properties of Hot Rolled Products*, Elsevier Science Ltd, The Netherlands.

Li, C. S., Xu, J. Z., He, X. M., Liu, X. H. and Wang, G. D., 2001, *Journal of Materials Processing Technology*, Vol. 116, pp. 201-204.

Liu, G., Li, M., Zhang, Y. and Zhou, Y., 2003, *Materials Science and Engineering*, Vol. A360, pp. 408-414.

Manning, M. I. and Metcalfe, E., 1977, *Sixth European Congress on Metallic Corrosion*, Society of Chemical Industry, London, pp. 121-127.

References

Marshall, D. B. and Evans, H. E., 1984, *Journal of Applied Physics*, Vol. 56, pp. 2632-2638.

Matsuno, F., 1980, *Transactions ISIJ*, Vol. 20, pp. 413-421.

Mehrotra, P. K. and Quinto, D. T., 1985, *Journal of Vacuum. Science & Technology*, Vol. A3, pp. 2401-2405.

Miannay, D. P., 1988, *Fracture Mechanics*, Springer-Verlag, New York.

Modin, S., 1962, *Metal Treatment*, Vol. 29, pp. 89-95.

Mrowec, S., 1980, *Defects and Diffusion in Solids, An Introduction*, Polish Scientific Publishers, Warszawa.

Nabarro, F. R. N., 1948, *Report of a Conference on the Strength of Solids*, The Physical Society, London, pp. 75-90.

Nakamura, T. and Sato, M., 1993, *Tetsu-to-Hagane*, Vol. 79, pp. 74-80.

Nakamura, T. and Sato, M., 1994, *Tetsu-to-Hagane*, Vol. 80, pp. 55-60.

Nova, 1997, *User Manual for Nova Model 376WP Portable Flue Gas Analyzer in Weatherproof Case*.

Pettit, F. S. and Wagner, J. B., 1964, *Acta Metallurgica*, Vol. 12, pp. 35-40.

Pfeil, L. B., 1929, *Journal of the Iron and Steel Institute*, Vol. 119, pp. 501-560.

Pilling, N. B. and Bedworth, R. E., 1923, *Journal of the Institute of Metals*, Vol. 29, pp. 529-595.

References

Preece, A., Richardson, G. T. and Cobb, J. W., 1939, *Iron and Steel Institute*, Special Report 24, pp. 9-63.

Rahmel, A., 1961, *Mitteilungen Der VGB*, Vol. 74, pp. 319-332.

Rahmel, A. and Tobolski, J., 1965, *Corrosion Science*, Vol. 5, pp. 333-346.

Ramaswamy, V., Benner, F. G. and Rosenthal, D., 1996, *Stahl und Eisen*, Vol. 116, pp. 93-100.

Ramírez-Cuellar, J., Guerrero-Mata, M. P., Leduc, L. A. and Colás, R., 2003, *Proceedings of International Conference on Thermomechanical Processing: Mechanics, Microstructure & Control*, ed. by Palmiere E. J., Mahfouf M. and Pinna C., Department of Engineering Materials, The University of Sheffield, Sheffield, pp. 418-422.

Randle, V. and Engler, O., 2000, *Texture Analysis Macrotecture Microtexture & Orientation Mapping*, Gordon and Breach Science Publishers, The Netherlands.

Reimer, L., 1998, *Scanning Electron Microscopy Physics of Image Formation and Microanalysis, Second Edition*, Springer, Germany.

Rhines, F. N. and Wolf, J. S., 1970, *Metallurgical Transactions*, Vol. 1, pp. 1701-1710.

Robertson, J. and Manning, M. I., 1990, *Materials Science and Technology*, Vol. 6, pp. 81-91.

Rolls, R., 1963, *Metal Treatment and Drop Forging*, November, pp. 427-436.

Sachs, K. and Tuck, C. W., 1968, *Iron and Steel Institute*, Publication No. 111, pp. 1-17.

References

- Scheil, E. and Kiwit, K., 1936, *Archiv für das Eisenhüttenwesen*, Vol. 9, pp. 405-416.
- Schütze, M., 1997, *Protective Oxide Scales and Their Breakdown*, The Institute of Corrosion, UK.
- Schwartz, A. J., Kumar, M. and Adams, B. L., 2000, *Electron Backscatter Diffraction in Materials Science*, Kluwer Academic/Plenum Publishers, United States of America.
- Schwenk, W. and Rahmel, A., 1986, *Oxidation of Metals*, Vol. 25, pp. 293-303.
- Schwerdtfeger, K. and Zhou, S., 2003, *Steel Research International*, Vol. 74, pp. 538-547.
- Seki, H. *et al.*, 1996, *CAMP-ISIJ*, Vol. 9, pp. 972-975.
- Sheasby, J. S., Boggs, W. E. and Turkdogan, E. T., 1984, *Metal Science*, Vol. 18, pp. 127-136.
- Sheppard, T. and Steen, W. M., 1970, *Journal of The Iron and Steel Institute*, Vol. 208, pp. 797-805.
- Shiraiwa, T. and Matsuno, F., 1967, *Sumitomo Metals*, Vol. 19, pp. 33-43.
- Skagen, R. C. and Gilbert, D. C., 1995, *Iron and Steel Engineer*, Vol. 72, pp. 42-44.
- Smeltzer, W. W., 1960, *Transactions of the Metallurgical Society of Aime*, Vol. 218, pp. 674-689.
- Smeltzer, W. W., 1960, *Acta Metallurgica*, Vol. 8, pp. 377-383.
- Smeltzer, W. W. and Young, D. J., 1975, *Progress in Solid-State Chemistry*, Vol. 10, pp. 17-54.

References

Stott, F. H., 1988, *Materials Science and Technology*, Vol. 4, pp. 431-438.

Stringer, J., 1970, *Corrosion Science*, Vol. 10, pp-513-543.

The Oxide Handbook, 1982, 2nd edition, edited by Samsonov, G. V., translated by Johnston, R. K., published by IFI/ Plenum Data Company, New York.

Trenkler, H., 1971, *Berg-und Hüttenmännische Monatshefte*, Vol. 116, pp. 425-428.

TSL, 2001, *OIM Analysis User Manual*.

Tuck, C. W., Odgers, M. and Sachs, K., 1969, *Corrosion Science*, Vol. 9, pp. 271-285.

Tuck, C. W., Odgers, M., Sachs, K. and Reinbold, B. G., 1966, *Werkstoffe und Korrosion*, Vol. 17, pp. 34-48.

Tylecote, R. F., 1960, *Journal of the Iron and Steel Institute*, Vol. 196, pp. 135-141.

Tylecote, R. F., 1965, *Memoires et Etudes Scientifiques de la Revue de Metallurgie*, Vol. 62, pp. 241-247.

Vallet, P., 1965, *Comptes Rendus de l'Academie de la Science*, Paris, t. 261, pp 4396-4399.

Vallet, P. and Raccah, P., 1965, *Memoires Scientifiques de la Revue de Metallurgie*, Vol. 62, pp. 1-29.

Vergne, C., Boher, C., Levailant, C. and Gras, R., 2001, *Wear*, Vol. 250, pp. 322-333.

Villars, P. and Calvert, L. D., 1991, *Peason's Handbook of Crystallographic Data for Intermetallic Phases*, ASM International, New York, Vol. 3, pp. 3327-3329.

References

Wagner, C., 1933, *Zeitschrift für Physikalische*, Abt. B. 21, Heft 1/2, pp. 25-41.

Wolf, M. M., March 2000, *Iron & Steelmaker*, Vol. 27, pp.69-71.

Wolf, M. M., April 2000, *Iron & Steelmaker*, Vol. 27, pp.58-60.

Wolf, M. M., July 2000, *Iron & Steelmaker*, Vol. 27, pp. 63-65.

Wolf, M. M., September 2000, *Iron & Steelmaker*, Vol. 27, pp.90-92.

Wolf, M. M., October 2000, *Iron & Steelmaker*, Vol. 27, pp.114-115.

Zitterman, J. A., Bacco, R. P. and Boggs, W. E., 1982, *Journal of Metals*, Vol. 34, pp. 22-26.

Appendix A

Card Number 6 - 0615			
<i>Iron Oxide (FeO)</i>			
<i>Radiation: CuK_α (λ = 1.5418 Å)</i>			
<i>d (Å)</i>	<i>2θ</i>	<i>I/I₁</i>	<i>hkl</i>
2.49	36.07006	80	111
2.153	41.96202	100	200
1.523	60.81837	60	220
1.299	72.80536	25	311
1.243	76.66047	15	222
1.077	91.41507	15	400
0.988	102.5694	10	331
0.9631	106.3435	15	420

Card Number 11 - 614			
<i>Iron Oxide (Fe₃O₄)</i>			
<i>Radiation: CuK_α (λ = 1.5418 Å)</i>			
<i>d (Å)</i>	<i>2θ</i>	<i>I/I₁</i>	<i>hkl</i>
4.85	18.29173	40	111
2.966	30.12972	70	220
2.53	35.48066	100	311
2.419	37.16689	10	222
2.096	43.15949	70	400
1.712	53.52485	60	422
1.614	57.06187	85	333,511
1.483	62.64098	85	440
1.327	71.03259	20	620
1.279	74.13228	30	533
1.264	75.16299	10	622
1.2112	79.05912	20	444
1.1214	86.85628	30	642
1.0922	89.79216	60	553,731
1.0489	94.60775	40	800
0.9890	102.4249	10	660,822
0.9692	105.3858	40	555,751
0.9386	110.4362	30	840
0.8794	122.4747	40	931
0.8565	128.3315	50	844
0.8113	143.685	40	951

Card Number 13 - 534			
<i>Iron Oxide (Fe₂O₃)</i>			
Radiation: CuK _α (λ = 1.5418 Å)			
<i>d</i> (Å)	2θ	<i>I</i> / <i>I</i> ₁	<i>hkl</i>
3.66	24.31836	25	012
2.69	33.30662	100	104
2.51	35.77289	50	110
2.285	39.43395	2	006
2.201	41.0052	30	113
2.070	43.72932	2	202
1.838	49.59636	40	024
1.69	54.2784	60	116
1.634	56.30072	4	211
1.596	57.76567	16	018
1.484	62.594	35	214
1.452	64.13566	35	300
1.349	69.70425	4	208
1.310	72.09748	20	1010,119
1.258	75.5842	8	220
1.226	77.92223	2	036
1.213	78.91887	4	223
1.189	80.83613	8	128
1.162	83.12324	10	0210
1.141	85.00703	12	134
1.102	88.78123	14	226
1.076	91.52429	2	042
1.055	93.89205	18	2110
1.042	95.4334	2	1112
1.038	95.92012	2	404
0.9890	102.4249	10	232,318
0.9715	105.0305	2	229
0.9601	106.823	18	324
0.9578	107.1945	6	0114
0.9512	108.2798	12	140,0213
0.9314	111.722	6	413
0.9204	113.7689	6	048
0.9080	116.2081	25	1310

Appendix B

The intensity of the diffraction pattern of a particular phase in a mixture depends on the concentration of that phase in the mixture. Therefore, depending on the scale composition, the number of the selected reflections hkl of a particular phase for the phase analysis varied from two to six. A complete analysis for the scale formed in 5O₂-15CO₂-N₂ gas mixture at 1100°C for 60 min. is presented in Table A1. The selected reflections, number of combinations of the selected reflections, scale mean phase composition and standard deviation of the scale analyses are shown in Tables (A2)-(A8).

Table A.1 Example of scale analysis. The scale was formed in 5O₂-15CO₂-N₂ gas mixture at 1100 °C for 60 min.

Integrated intensity		Intensity combination			Analysis		
(hkl)	Area (mm ²)	FeO (hkl)	Fe ₃ O ₄ (hkl)	Fe ₂ O ₃ (hkl)	FeO (%)	Fe ₃ O ₄ (%)	Fe ₂ O ₃ (%)
(111) FeO	90.48	(200)	(400)	(104)	58.91	27.03	14.06
(200) FeO	185.81	(200)	(220)	(104)	57.51	28.76	13.73
(220) Fe ₃ O ₄	19.29	(111)	(400)	(104)	55.12	29.52	15.36
(400) Fe ₃ O ₄	16.45	(111)	(220)	(104)	53.69	31.35	14.96
(104) Fe ₂ O ₃	15.35	(200)	(220)	(113)	59.28	29.65	11.07
(113) Fe ₂ O ₃	4.30	(200)	(400)	(113)	60.77	27.88	11.35
(111) FeO	90.48	(111)	(220)	(113)	55.50	32.40	12.10
(200) FeO	185.81	(111)	(400)	(113)	57.03	30.54	12.43
				$\bar{X} =$	57.23	29.64	13.13
				$\bar{S} =$	2.4	1.8	1.6

Table A.2 Analysis of the iron oxides in scales formed over the temperature range 1000-1250 °C in 1O₂-15CO₂-10H₂O-N₂ gas mixture.

Temp. (°C)	Oxidation time (min)	hkl				Volume fraction (%)		
		Wüstite (FeO)	Magnetite (Fe ₃ O ₄)	Hematite (Fe ₂ O ₃)	No. of Combinations	Wüstite (FeO)	Magnetite (Fe ₃ O ₄)	Hematite (Fe ₂ O ₃)
1000	12	(111), (200)	(220), (400)	(104)	4	93.47 ± 1.4	5.71 ± 1.3	0.82 ± 0.2
1000	30	(111), (200)	(220), (400)	(104)	4	92.15 ± 1.3	6.26 ± 1.1	1.59 ± 0.2
1000	60	(111), (200)	(220), (400)	(104)	4	81.92 ± 3.5	15.32 ± 3.2	2.76 ± 0.2
1000	120	(111), (200)	(220), (400)	(104)	4	78.62 ± 3.2	18.34 ± 3.1	3.04 ± 0.5
1050	12	(111), (200)	(220), (400)	(104)	4	82.90 ± 2.8	13.91 ± 2.9	3.19 ± 0.2
1050	30	(111), (200)	(220), (400)	(104)	4	81.32 ± 2.1	15.44 ± 1.8	3.24 ± 0.3
1050	60	(111), (200)	(220), (400)	(104)	4	79.82 ± 2.7	16.65 ± 2.3	3.53 ± 0.4
1050	120	(111), (200)	(220), (400)	(104)	4	77.07 ± 2.3	17.73 ± 2.4	5.20 ± 0.2
1100	12	(111), (200)	(220), (400)	(104)	4	91.29 ± 3.0	7.90 ± 2.9	0.81 ± 0.2
1100	30	(111), (200)	(220), (400)	(104)	4	88.50 ± 4.1	10.67 ± 4.1	0.83 ± 0.2
1100	60	(111), (200)	(220), (400)	(104)	4	87.15 ± 3.2	11.72 ± 3.0	1.13 ± 0.2
1100	120	(111), (200)	(220), (400)	(104)	4	85.21 ± 2.8	12.04 ± 2.9	2.75 ± 0.2
1150	12	(111), (200)	----	----	----	100 ± 0	----	----
1150	30	(111), (200)	(220)	----	2	98.50 ± 0.5	1.50 ± 0.5	----
1150	60	(111), (200)	(220)	(104)	2	97.38 ± 0.4	1.64 ± 0.3	0.98 ± 0.2
1150	120	(111), (200)	(220), (400)	(104)	4	87.33 ± 2.4	10.42 ± 2.0	2.25 ± 0.4
1200	12	(111), (200)	----	----	----	100 ± 0	----	----
1200	30	(111), (200)	(220)	----	2	95.94 ± 1.2	4.06 ± 1.2	----
1200	60	(111), (200)	(220)	----	2	96.54 ± 1.0	3.46 ± 1.0	----
1200	120	(111), (200)	(220), (400)	(104)	4	83.65 ± 1.3	9.96 ± 1.3	6.39 ± 0.2
1250	12	(111), (200)	(220)	----	2	98.84 ± 0.2	1.16 ± 0.1	----
1250	30	(111), (200)	(220)	----	2	98.55 ± 0.3	1.45 ± 0.3	----
1250	60	(111), (200)	(220)	----	2	98.26 ± 0.4	1.74 ± 0.4	----
1250	120	(111), (200)	(220), (400)	(104)	4	85.82 ± 1.4	10.21 ± 1.5	3.97 ± 0.2

Table A.3 Analysis of the iron oxides in scales formed over the temperature range 1000-1250 °C in 5O₂-15CO₂-10H₂O-N₂ gas mixture.

Temp. (°C)	Oxidation time (min)	hkl				Volume fraction (%)		
		Wüstite (FeO)	Magnetite (Fe ₃ O ₄)	Hematite (Fe ₂ O ₃)	No. of Combinations	Wüstite (FeO)	Magnetite (Fe ₃ O ₄)	Hematite (Fe ₂ O ₃)
1000	12	(111), (200)	(220), (400)	(104)	4	75.94 ± 3.6	19.33 ± 3.3	4.73 ± 0.6
1000	30	(111), (200)	(220), (400)	(104)	4	72.05 ± 2.6	21.45 ± 2.0	6.5 ± 0.6
1000	60	(111), (200)	(220), (400)	(104)	4	69.53 ± 1.6	22.73 ± 1.5	7.74 ± 0.3
1000	120	(111), (200)	(220), (400)	(104), (113)	8	64.10 ± 2.7	24.58 ± 3.0	11.32 ± 0.7
1050	12	(111), (200)	(220), (400)	(104)	4	77.81 ± 2.6	17.30 ± 2.5	4.89 ± 0.4
1050	30	(111), (200)	(220), (400)	(104)	4	69.67 ± 3.0	24.40 ± 3.2	5.93 ± 0.3
1050	60	(111), (200)	(220), (400)	(104)	4	64.49 ± 3.1	29.11 ± 2.9	6.40 ± 0.5
1050	120	(111), (200)	(220), (400)	(104)	4	61.30 ± 2.3	31.69 ± 2.0	7.01 ± 0.4
1100	12	(111), (200)	(220), (400)	(104)	4	80.03 ± 3.8	16.21 ± 3.9	3.76 ± 0.3
1100	30	(111), (200)	(220), (400)	(104)	4	75.61 ± 3.3	19.71 ± 3.5	4.68 ± 0.3
1100	60	(111), (200)	(220), (400)	(104)	4	68.43 ± 3.4	24.02 ± 3.8	7.55 ± 0.4
1100	120	(111), (200)	(220), (400)	(104), (113)	8	64.83 ± 3.0	25.08 ± 3.2	10.09 ± 0.8
1150	12	(111), (200)	(220), (400)	(104)	4	65.89 ± 2.9	28.44 ± 2.6	5.67 ± 0.5
1150	30	(111), (200)	(220), (400)	(104)	4	61.91 ± 3.7	30.02 ± 3.0	8.07 ± 0.8
1150	60	(111), (200)	(220), (400)	(104)	4	59.37 ± 3.6	31.72 ± 4.1	8.91 ± 0.6
1150	120	(111), (200)	(220), (400)	(104), (113)	8	58.65 ± 3.1	32.18 ± 2.9	9.17 ± 1.1
1200	12	(111), (200)	(220), (400)	(104)	4	80.81 ± 2.6	17.67 ± 2.4	1.52 ± 0.2
1200	30	(111), (200)	(220), (400)	(104)	4	74.76 ± 2.7	20.19 ± 2.3	5.05 ± 0.5
1200	60	(111), (200)	(220), (400)	(104)	4	72.13 ± 3.8	21.75 ± 3.7	6.12 ± 0.6
1200	120	(111), (200)	(220), (400)	(104)	4	70.49 ± 3.8	22.75 ± 3.1	6.76 ± 0.9
1250	12	(111), (200)	(220), (400)	(104)	4	85.83 ± 3.3	12.82 ± 3.1	1.35 ± 0.2
1250	30	(111), (200)	(220), (400)	(104)	4	84.34 ± 3.4	13.06 ± 2.8	2.60 ± 0.6
1250	60	(111), (200)	(220), (400)	(104)	4	82.66 ± 3.0	14.31 ± 2.5	3.03 ± 0.5
1250	120	(111), (200)	(220), (400)	(104)	4	78.58 ± 3.8	15.20 ± 2.8	6.22 ± 1.1

Table A.4 Analysis of the iron oxides in scales formed at the temperature of 1100 °C and 1250 °C in 10₂-15CO₂-N₂ gas mixture.

Temp. (°C)	Oxidation time (min)	hkl				Volume fraction (%)		
		Wüstite (FeO)	Magnetite (Fe ₃ O ₄)	Hematite (Fe ₂ O ₃)	No. of Combinations	Wüstite (FeO)	Magnetite (Fe ₃ O ₄)	Hematite (Fe ₂ O ₃)
1100	12	(111), (200)	(220), (400)	(104)	4	80.23 ± 3.9	15.03 ± 2.9	4.74 ± 0.9
1100	30	(111), (200)	(220), (400)	(104)	4	66.07 ± 2.7	25.01 ± 3.0	8.92 ± 0.4
1100	60	(111), (200)	(220), (400)	(104)	4	60.93 ± 2.2	30.40 ± 1.7	8.67 ± 0.5
1100	120	(111), (200)	(220), (400)	(104), (113)	8	45.62 ± 3.1	39.14 ± 3.0	15.24 ± 2.0
1250	12	(111), (200)	(220), (400)	(104)	4	93.89 ± 2.0	4.72 ± 1.4	1.39 ± 0.3
1250	30	(111), (200)	(220), (400)	(104)	4	84.73 ± 3.2	13.26 ± 2.8	2.01 ± 0.4
1250	60	(111), (200)	(220), (400)	(104)	4	78.20 ± 2.9	18.44 ± 2.5	3.36 ± 0.4
1250	120	(111), (200)	(220), (400)	(104)	4	56.63 ± 3.4	36.75 ± 2.9	6.62 ± 0.5

Table A.5 Analysis of the iron oxides in scales formed at the temperature of 1100 °C and 1250 °C in 10₂-10H₂O-N₂ gas mixture.

Temp. (°C)	Oxidation time (min)	hkl				Volume fraction (%)		
		Wüstite (FeO)	Magnetite (Fe ₃ O ₄)	Hematite (Fe ₂ O ₃)	No. of Combinations	Wüstite (FeO)	Magnetite (Fe ₃ O ₄)	Hematite (Fe ₂ O ₃)
1100	12	(111), (200)	(220)	(104)	2	97.59 ± 0.5	1.61 ± 0.3	0.80 ± 0.2
1100	30	(111), (200)	(220), (400)	(104)	4	92.77 ± 1.5	6.42 ± 1.4	0.81 ± 0.2
1100	60	(111), (200)	(220), (400)	(104)	4	87.01 ± 2.6	11.19 ± 2.3	1.80 ± 0.3
1100	120	(111), (200)	(220), (400)	(104)	4	73.41 ± 3.8	20.46 ± 2.9	6.13 ± 0.9
1250	12	(111), (200)	(220)	(104)	2	99.19 ± 0.4	0.81 ± 0.4	-----
1250	30	(111), (200)	(220)	(104)	2	98.11 ± 0.5	1.89 ± 0.5	-----
1250	60	(111), (200)	(220)	(104)	2	97.83 ± 0.7	2.17 ± 0.7	-----
1250	120	(111), (200)	(220), (400)	(104)	4	84.86 ± 3.7	11.18 ± 2.8	3.96 ± 0.9

Table A.6 Analysis of the iron oxides in scales formed at the temperature of 1100 °C and 1250 °C in 5O₂-15CO₂-N₂ gas mixture.

Temp. (°C)	Oxidation time (min)	hkl				Volume fraction (%)		
		Wüstite (FeO)	Magnetite (Fe ₃ O ₄)	Hematite (Fe ₂ O ₃)	No. of Combinations	Wüstite (FeO)	Magnetite (Fe ₃ O ₄)	Hematite (Fe ₂ O ₃)
1100	12	(111), (200)	(220), (400)	(104)	4	76.74 ± 3.1	18.64 ± 3.3	4.62 ± 0.3
1100	30	(111), (200)	(220), (400)	(104)	4	71.70 ± 2.2	21.10 ± 1.6	7.23 ± 0.5
1100	60	(111), (200)	(220), (400)	(104), (113)	8	57.23 ± 2.4	29.64 ± 1.8	13.13 ± 1.6
1100	120	(111), (200)	(220), (400)	(104), (113)	8	47.11 ± 2.0	37.43 ± 2.5	15.46 ± 1.1
1250	12	(111), (200)	(220), (400)	(104)	4	71.56 ± 2.8	26.83 ± 2.6	1.61 ± 0.2
1250	30	(111), (200)	(220), (400)	(104)	4	59.34 ± 3.1	37.70 ± 3.3	2.96 ± 0.2
1250	60	(111), (200)	(220), (400)	(104)	4	52.74 ± 3.3	41.64 ± 2.9	5.62 ± 0.4
1250	120	(111), (200)	(220), (400)	(104)	4	47.96 ± 3.3	44.90 ± 2.8	7.14 ± 0.6

Table A.7 Analysis of the iron oxides in scales formed at the temperature of 1100 °C and 1250 °C in 5O₂-10H₂O-N₂ gas mixture.

Temp. (°C)	Oxidation time (min)	hkl				Volume fraction (%)		
		Wüstite (FeO)	Magnetite (Fe ₃ O ₄)	Hematite (Fe ₂ O ₃)	No. of Combinations	Wüstite (FeO)	Magnetite (Fe ₃ O ₄)	Hematite (Fe ₂ O ₃)
1100	12	(111), (200)	(220), (400)	(104)	4	77.54 ± 3.8	18.38 ± 3.4	4.08 ± 0.5
1100	30	(111), (200)	(220), (400)	(104), (113)	8	68.02 ± 3.3	22.45 ± 2.3	9.53 ± 1.6
1100	60	(111), (200)	(220), (400)	(104), (113)	8	57.42 ± 2.7	31.08 ± 2.6	11.50 ± 1.3
1100	120	(111), (200)	(220), (400)	(104), (113)	8	51.71 ± 3.1	36.28 ± 3.8	12.01 ± 1.4
1250	12	(111), (200)	(220), (400)	(104)	4	83.18 ± 3.0	15.63 ± 2.8	1.19 ± 0.2
1250	30	(111), (200)	(220), (400)	(104)	4	81.34 ± 3.5	17.12 ± 3.4	1.54 ± 0.2
1250	60	(111), (200)	(220), (400)	(104)	4	80.34 ± 3.1	18.02 ± 2.9	1.64 ± 0.2
1250	120	(111), (200)	(220), (400)	(104)	4	80.75 ± 3.1	17.22 ± 3.2	2.03 ± 0.2

Table A.8 Analysis of the iron oxides in scales formed over the temperature range 750-1200 °C in dry air.

Temp. (°C)	Oxidation time (s)	hkl				Volume fraction (%)		
		Wüstite (FeO)	Magnetite (Fe ₃ O ₄)	Hematite (Fe ₂ O ₃)	No. of Combinations	Wüstite (FeO)	Magnetite (Fe ₃ O ₄)	Hematite (Fe ₂ O ₃)
750	30	(111), (200)	(220), (400)	(104), (113)	8	46.53 ± 3.2	41.29 ± 2.5	12.18 ± 2.1
750	120	(111), (200)	(220), (400)	(104), (113)	8	29.66 ± 3.8	54.59 ± 3.3	15.75 ± 1.8
750	600	(111), (200)	(220), (400)	(104), (113)	8	26.89 ± 2.9	44.23 ± 2.4	28.88 ± 2.4
800	30	(111), (200)	(220), (400)	(104)	4	79.84 ± 2.4	16.67 ± 2.3	3.49 ± 2.8
800	120	(111), (200)	(220), (400)	(104)	4	70.49 ± 2.7	21.84 ± 2.3	7.67 ± 0.6
800	600	(111), (200)	(220), (400)	(104), (113)	8	57.41 ± 2.4	30.61 ± 1.8	11.98 ± 1.6
850	30	(111), (200)	(220), (400)	----	4	92.53 ± 1.4	7.47 ± 1.4	----
850	120	(111), (200)	(220), (400)	(104)	4	86.91 ± 2.1	9.45 ± 1.7	3.64 ± 0.5
850	600	(111), (200)	(220), (400)	(104)	4	73.43 ± 3.0	19.97 ± 2.7	6.60 ± 0.6
900	30	(111), (200)	(220)	----	2	97.34 ± 1.0	2.66 ± 1.0	----
900	120	(111), (200)	(220)	----	2	97.25 ± 1.2	2.75 ± 1.2	----
900	600	(111), (200)	(220), (400)	(104)	4	86.18 ± 3.0	11.95 ± 2.7	1.87 ± 0.3
950	30	(111), (200)	(220), (400)	----	4	94.08 ± 1.9	5.92 ± 1.9	----
950	120	(111), (200)	(220), (400)	----	4	93.47 ± 1.9	6.53 ± 1.9	----
950	600	(111), (200)	(220), (400)	(104)	4	91.13 ± 2.2	6.96 ± 1.7	1.91 ± 0.5
1000	30	(111), (200)	(220)	----	2	96.10 ± 1.0	3.90 ± 1.0	----
1000	120	(111), (200)	(220), (400)	----	4	94.65 ± 1.4	5.35 ± 1.4	----
1000	600	(111), (200)	(220), (400)	(104)	4	92.42 ± 1.4	5.64 ± 1.1	1.94 ± 0.3
1050	30	(111), (200)	(220)	----	2	94.46 ± 1.3	5.54 ± 1.3	----
1050	120	(111), (200)	(220), (400)	(104), (113)	8	49.71 ± 2.7	34.41 ± 2.5	15.88 ± 2.4
1050	600	(111), (200)	(220), (400)	(104), (113)	8	20.06 ± 1.7	58.41 ± 2.7	21.53 ± 2.3
1100	30	(111), (200)	(220), (400)	(104)	4	84.56 ± 3.2	9.48 ± 2.0	5.96 ± 1.2
1100	120	(111), (200)	(220), (400)	(104)	4	56.75 ± 2.2	34.91 ± 1.9	8.34 ± 0.4
1100	600	(111), (200)	(220), (400)	(104), (113)	8	18.38 ± 2.3	61.03 ± 2.2	20.59 ± 2.0
1150	30	(111), (200)	(220), (400)	----	4	89.25 ± 2.4	10.76 ± 2.4	----
1150	120	(111), (200)	(220), (400)	(104)	4	69.04 ± 2.2	24.79 ± 1.9	6.17 ± 0.4
1150	600	(111), (200)	(220), (400)	(104), (113)	8	52.94 ± 2.1	33.95 ± 1.5	13.11 ± 2.1

Appendix B

1200	30	(111), (200)	(220), (400)	-----	4	79.12 ± 2.2	20.88 ± 2.2	-----
1200	120	(111), (200)	(220), (400)	(104)	4	67.61 ± 2.4	26.38 ± 2.2	6.01 ± 0.4
1200	600	(111), (200)	(220), (400)	(104), (113)	8	55.94 ± 3.3	34.97 ± 3.9	9.09 ± 1.0